Reactivity of the Clay Mineral Montmorillonite: A First Principles Study

Stackhouse, Stephen

Reactivity of the Clay Mineral Montmorillonite: A First Principles Study

A thesis presented to the University of London in partial fulfilment of the requirements for the degree of Doctor of Philosophy

by

Stephen Stackhouse

of the

Department of Chemistry

Queen Mary, University of London

September 2003

Abstract

The recent development of clay-polymer nanocomposite materials has led to an increased interest in the structure and properties of clay minerals. In this thesis the reactivity of the clay mineral montmorillonite is explored by means of density functional theory based calculations. In particular three aspects are considered: catalytic properties, cation migration and dehydroxylation.

The origin of the catalytic properties of the clay mineral is investigated in the context of the synthesis of clay-polymer nanocomposite materials, by *in situ*, intercalative polymerisation. It is found that catalysis is most likely to occur at the clay mineral lattice-edge where exposed aluminium atoms act as Lewis acid sites.

Migration of lithium cations into the clay mineral lattice is explored by means of first principles molecular dynamics. Comparison of calculated hydroxyl stretching frequencies, with those from experiment indicates that cations migrate to vacant octahedral sites, as oppose to the ditrigonal cavities.

Dehydroxylation of the clay mineral is examined by consideration of a *cis*-vacant pyrophyllite structure. It is shown that dehydroxylation leads to formation of a *trans*-vacant structure, with aluminium in trigonal bipyramidal coordination and a highly distorted tetrahedral layer. Differences in the dehydroxylation behaviour of *cis* and *trans*-vacant pyrophyllite are shown to be due to the fact that in the former adjacent hydroxyl groups bridge different pairs of aluminium atoms, while in the latter they are both bonded to the same pair.

Overall density functional theory based calculations are shown to be a powerful tool for the study of the structure and reactivity of clay minerals.

Acknowledgements

The research described in this thesis was supported financially by Queen Mary, University of London and W. R. Grace & Co. To whom I am most grateful. It is also a pleasure to be able to thank those people who have helped and supported me over the past years, both scientifically and personally.

I would like to thank my supervisor Peter Coveney for his general oversight and encouragement to both present and publish my work. I am also very grateful to Keir Novik, Simon Clifford, Matt Harvey and Jon Chin for computing support; Phil Hasnip, Matt Probert and Eric Sandré for initial help with CASTEP; David Benoit and Pascal Boulet for teaching me about density functional theory and *ab initio* methods in general; and Steve Newman for his encouragement. In addition, I am indebted to Bill Jones and Chris Greenwell, with whom I have collaborated on work not presented in this thesis. It was a pleasure to work with you.

I would also like to thank those who I should have seen the most, but have probably seen the least, my housemates: Ana, Anastasia, Jie, Nélido and Simba. Many friends have also blessed me immensely over the last few years: Rute, Marcie, Julie, Konrad, Roma, Sergey, Natasha, Chris, Bryan and Shirley, Adam and Helen, Roger and Sarah, Martin and Sarah ...you'll never know what it means to me... There is not enough space here to mention everyone at Abbey Road Baptist church, but particular thanks goes to Iain and Lucy, Joe and Ulrica, Daniel and Celina, Deise, Magali, Alberto, Douglas, Stacy, Kleber, Ellen, Renato, James and Sol. I also thank Will and his wife Anita for much wise counsel. You are missed brother.

Most especially, I thank my family, for all their love, support and prayers.

But we have this treasure in jars of clay to show that this all-surpassing power is from God and not from us. 2 Corinthians 4 v 7.

Contents

List of Tables

List of Figures

Chapter 1

Clay Minerals

Clay minerals are naturally occuring materials formed by weathering and decomposition of igneous rocks.[1] They compose a large part of the earths mantle and are commonly regarded as those particles that comprise the 2 μm colloidal fraction of soil, sediments, rocks and waters.

1.1 Crystal Structure

The small particle size of clay minerals has in most cases prevented their study by single-crystal X-ray diffraction. Fundamental structural data is therefore limited. In spite of this, their general structural attributes are considered well established.[2,3]

1.1.1 Layer Structure

Most clay minerals are layered materials composed of continuous two-dimensional silicate layers stacked on top of each other in a well-defined manner. The various classes are distinguished by the differences in their sheets and species that lie in the spaces between them, known as the interlayer. In fact, most clay minerals are based on one of a small number of common frameworks. Essential to all of these are two basic structural components: a *tetrahedral sheet* and an *octahedral sheet.*

Tetrahedral Sheet

Figure 1.1 shows a tetrahedral sheet. Each silicon atom is in tetrahedral coordination with four oxygen atoms. Three out of the four oxygens are bridging and form a planar hexagonal network, while the remaining apical oxygens sit together in a plane above.

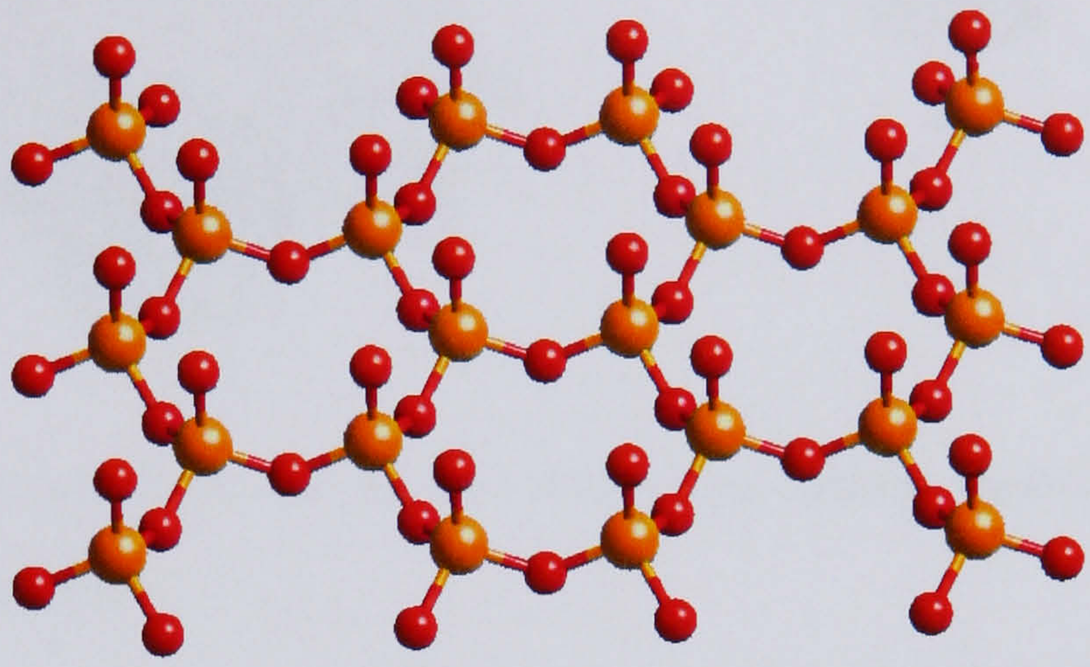

Figure 1.1: Tetrahedral layer. The colour scheme here is red for oxygen and yellow for silicon.

Octahedral Sheet

Octahedral sheets comprise metal ions in octahedral coordination embedded between two layers of close-packed oxygen and hydroxyl groups. The regular arrangement of the hydroxyl groups means that three distinct octahedral sites may be distinguished. These are designated *cis* or *trans* according to their position relative to the hydroxyls, shown in Figure 1.2. Two of the sites are *cis* and one is *trans*.

When the metal ions present are divalent, like magnesium, all octahedral sites are filled and a *trioctahedral* sheet is obtained, shown in Figure 1.3(a). In contrast, when trivalent cations such as aluminium are present, just two out of three sites are occupied and a *dioctahedral* sheet is obtained. Incomplete filling of octahedral sites in dioctahedral sheets gives rise to the possibility of structural isomers; one in which one *cis* and one *trans* site are occupied, defined as *cis*-vacant and a second in which both *cis* sites are filled, known as *trans*-vacant, as in Figures 1.3(b) and 1.3(c).

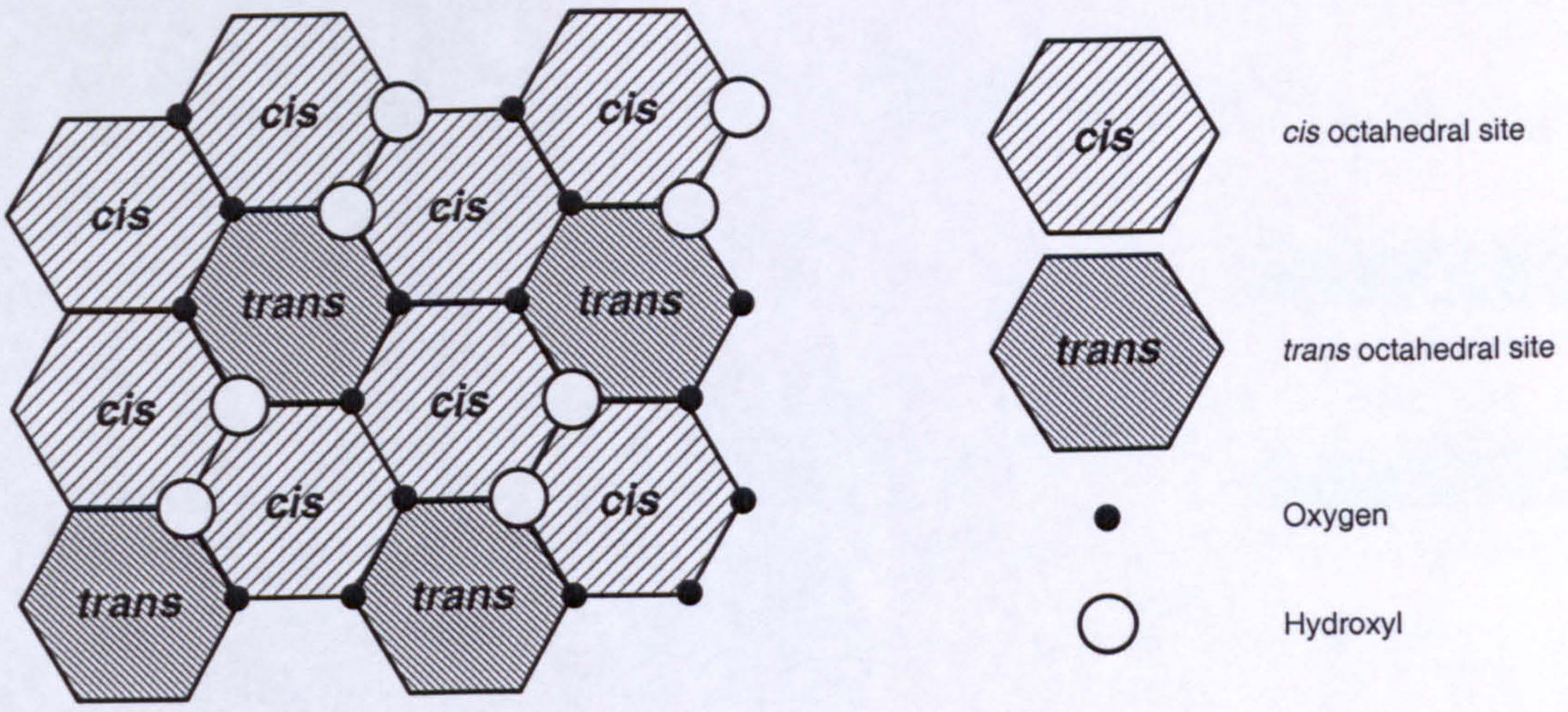

Figure 1.2: Schematic diagram of an octahedral sheet showing the different *cis* and *trans* octahedral sites.

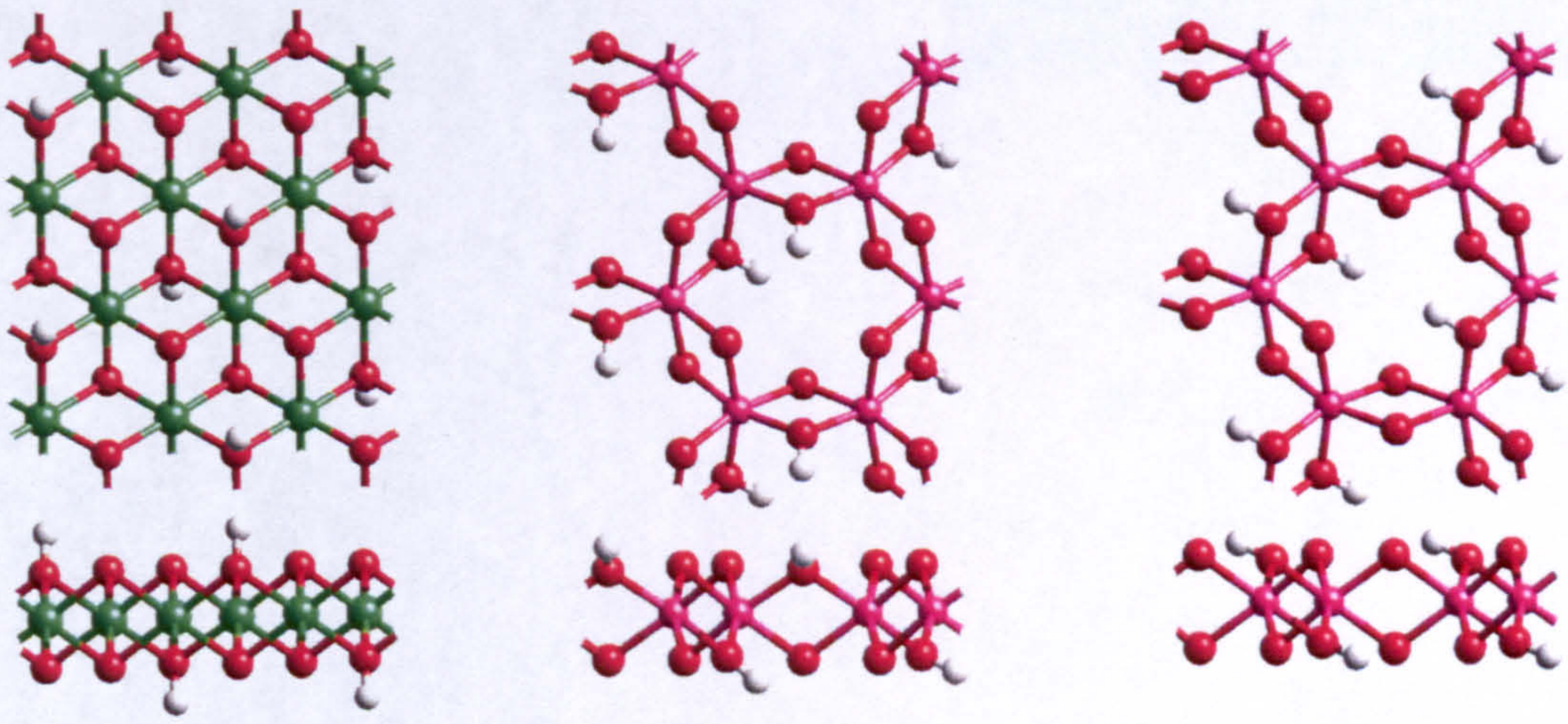

(a) Trioctahedral (b) Dioctahedral (*cis*-vacant) (c) Dioctahedral (*trans*-vacant)

Figure 1.3: The three types of octahedral sheet viewed looking onto the *ab* plane (top) and onto *bc* plane (bottom). The colour scheme here is white for hydrogen, red for oxygen, green for magnesium, pink for aluminium and yellow for silicon.

1.1.2 Common Frameworks

There are four common ways in which tetrahedral and octahedral sheets are found arranged together. These are:

1:1 Clay Minerals

Clay minerals with layer structures that comprise just one tetrahedral sheet joined to one octahedral sheet are known as 1:1, dimorphic or two-sheet clay minerals. Figure 1.4 illustrates the 1:1 layer structure of the clay mineral kaolinite.

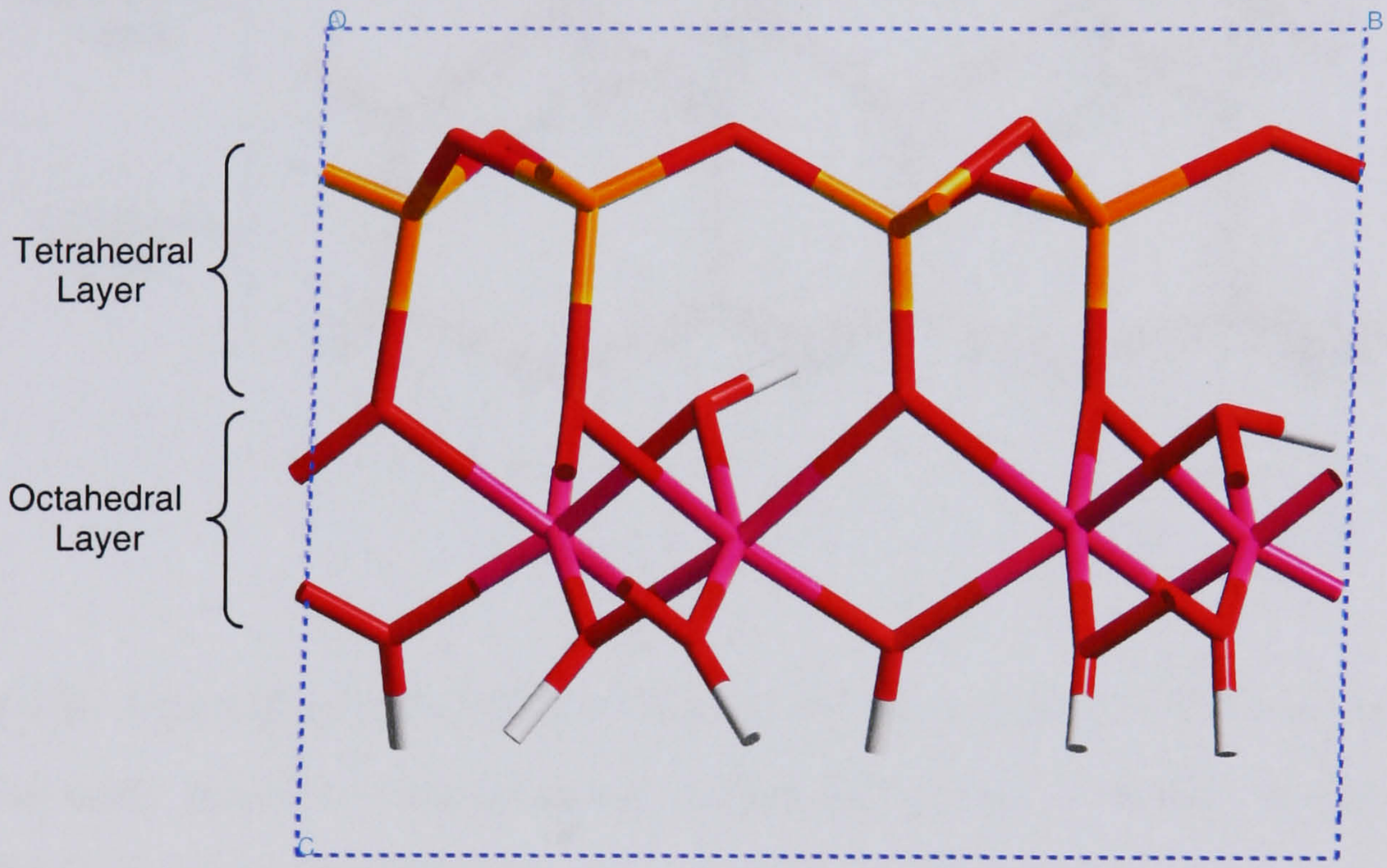

Figure 1.4: Unit cell of kaolinite. The colour scheme here is white for hydrogen, red for oxygen, pink for aluminium and yellow for silicon. Periodic boundaries are indicated by the blue dashed lines.

2:1 Clay Minerals

Clay mineral with layer structures that comprise an octahedral sheet sandwiched between two tetrahedral sheets are known as 2:1, trimorphic or three-sheet clay

minerals and are by far the most common of the layer silicates. Figure 4.3 illustrates the 2:1 layer structure of the clay mineral pyrophyllite.

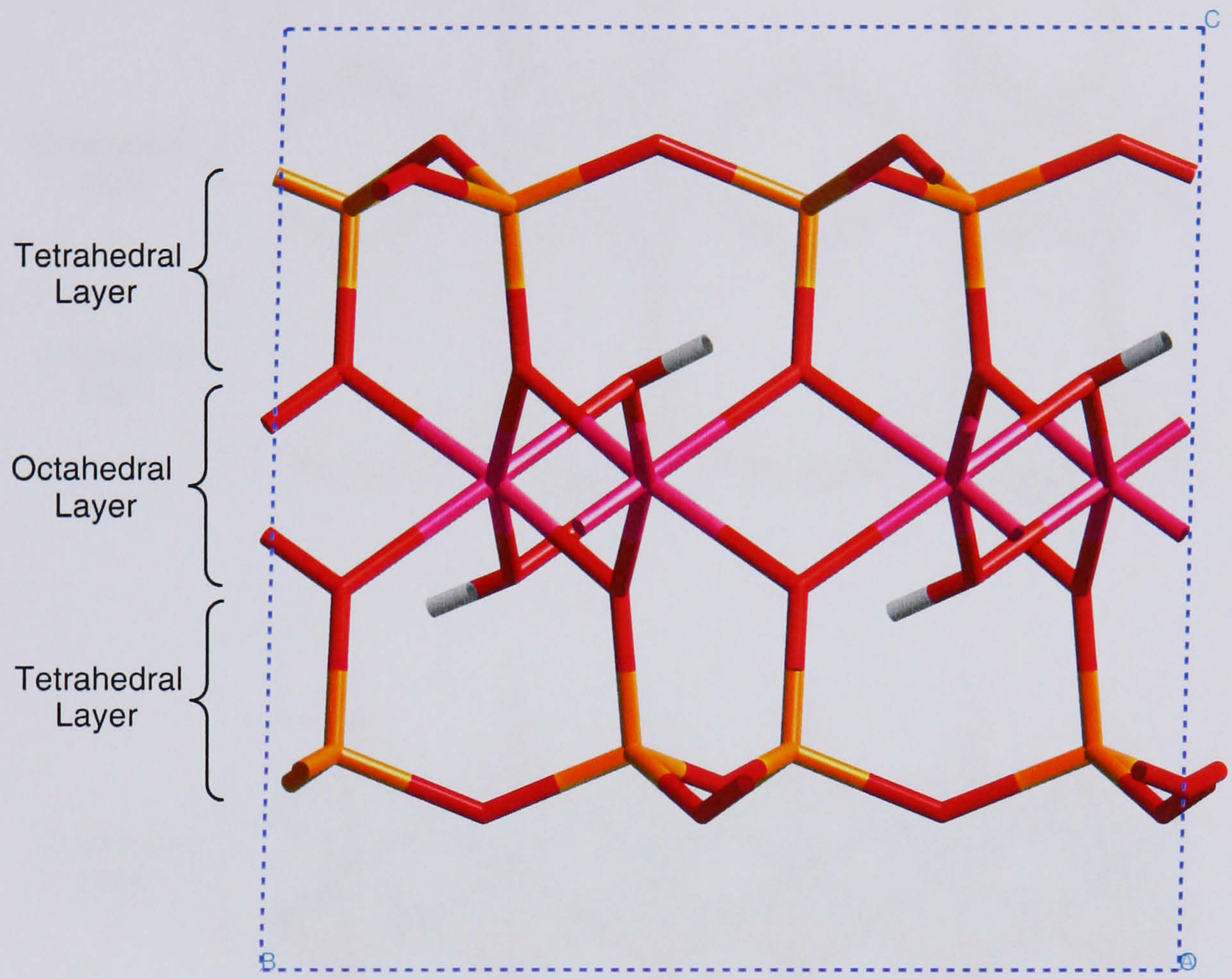

Figure 1.5: Unit cell of pyrophyllite. The colour scheme here is white for hydrogen, red for oxygen, pink for aluminium and yellow for silicon. Periodic boundaries are indicated by the blue dashed lines.

2:1:1 Clay Minerals

A more unusual arrangement is that of the 2:1:1, tetramorphic or four-sheet clay mineral, whose layer structure consists of an alternating sequence of 2:1 clay layers and octahedral sheets. Figure 1.6 illustrates the 2:1:1 layer structure typical of the chlorite group.

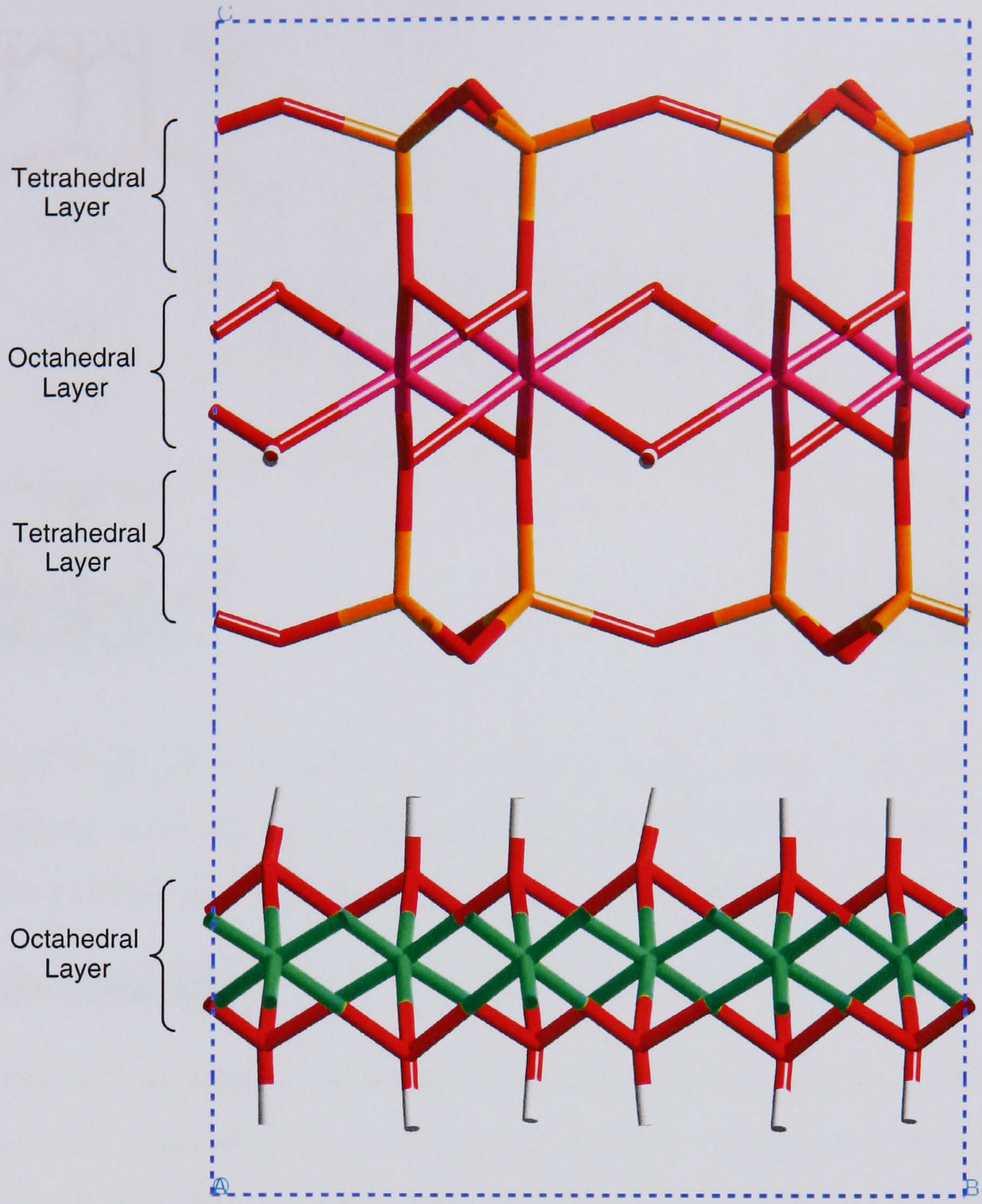

Figure 1.6: Unit cell of chlorite. The colour scheme here is white for hydrogen, red for oxygen, green for magnesium, pink for aluminium and yellow for silicon. Periodic boundaries are indicated by the blue dashed lines.

Pseudo-Layer Clay Minerals

An even more unusual composition is that of pseudo-layer silicates. These are not strictly layer silicates, with 2:1 layers being arranged in chains or bands, linked together by bridging oxygen atoms. Figure 1.7 illustrates the pseudo-layer structure typical of the sepiolite subgroup of clay minerals.

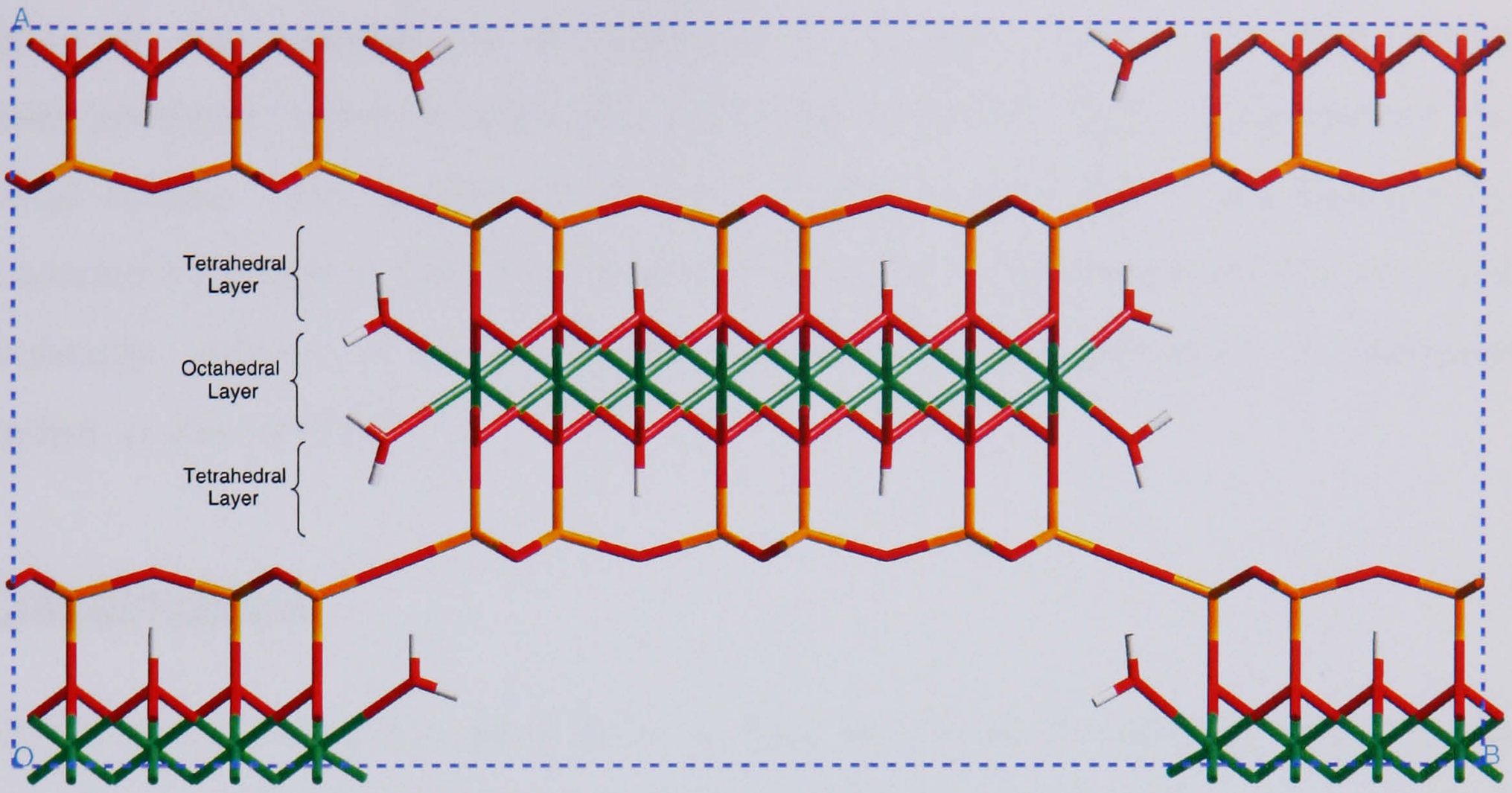

Figure 1.7: Unit cell of sepiolite. The colour scheme here is white for hydrogen, red for oxygen, green for magnesium, pink for aluminium and yellow for silicon. Periodic boundaries are indicated by the blue dashed lines.

1.1.3 Isomorphic Substitution

Further diversity in layer composition is generated by isomorphic substitution of tetrahedral and octahedral sites. The most common situation is that of partial substitution of aluminium in the octahedral layer and silicon in the tetrahedral layer by atoms of similar size and coordination, but of different valency. The most common substitutes for Si^{4+} are Al^{3+} and Fe^{3+}, while for Al^{3+} they are Fe^{3+}, Fe^{2+} and Mg^{2+}, though others are found. Such a process gives rise to layers with a permanent net-negative charge. This is balanced by sorption of extraneous metal cations into the interlayer.

1.1.4 Hydration

The hydration of interlayer cations provides a driving force for the sorption of water into the interlayer of the clay minerals that possess them. It is therefore normal

for such clay minerals to accommodate a certain amount of water within their interlayer, where it associates with and forms hydration shells around the metal cations. The acquisition of water via this mechanism is accompanied by a necessary increase in interlayer separation in order to accommodate the increased molecular volume of the interlayer contents. The phenomenon is therefore known as clay swelling.

1.2 Classification

Clay minerals are distinguished firstly by their layer type, secondly by their formula unit charge (related to the overall degree of substitution) and lastly by whether they adopt dioctahedral or trioctahedral geometry (related to the substitution of octahedral sites.) Table 1.1 provides a list of the most common clay mineral groups and subgroups. For a comprehensive review of the structure and properties of clay minerals the reader is directed to Grim[2,3] and Brindley and Brown.[4]

1.3 Applications of Clay Minerals

Clay minerals continue to be important industrial materials. In addition to more traditional uses, recent development of clay-polymer nanocomposites has opened up many new application areas.

1.3.1 Solid Catalysts

The catalytic properties of clay minerals have been well known since the mid 1930s, when they were used in the hydrocracking process, in the petrochemical industry. They exhibit many different Lewis and Brønstead acid sites, which make them useful as solid acid catalysts for many organic reactions.[5] This is particularly provident in view of current environmental legislation, which necessitates the substitution of liquid acids and bases by more amenable solid catalysts.

Table 1.1: Classification of Clay Minerals[a]

group	layer type	charge per formula unit[b]	subgroup
serpentine-kaolinite	1:1	~0.0	(trioctahedral) serpentines
			(dioctahedral) kaolins
talc-pyrophyllite	2:1	~0.0	(trioctahedral) talcs
			(diocathedral) pyrophyllites
smectite	2:1	~0.2-0.6	(trioctahedral) saponites
			(dioctahedral) montmorillonites
vermiculite	2:1	~0.6-0.9	trioctahedral vermiculites
			dioctahedral vermiculites
mica	2:1	~1.0	trioctahedral micas
			dioctahedral micas
brittle mica	2:1	~2.0	trioctahedral brittle micas
			dioctahedral brittle micas
chlorite	2:1:1	variable	trioctahedral chlorites
			dioctahedral chlorites
			di,trioctahedral chlorites
sepiolite-palygorskite	pseudo-layer	variable	sepiolites
			palygorskites

[a] Table adapted from Brindley and Brown.[4]

[b] In the case of smectites, vermiculites, micas and brittle micas a formula unit refers to a $O_{10}(OH)_2$.

In addition, the geometric structure of clay minerals may also play a role in their catalytic behaviour. Species adsorbed into the interlayer are constrained to diffuse in two-dimensional space rather than a three-dimensional volume, which increases their encounter frequencies and consequently the rate of any reaction between them.[6] Steric effects introduced by the confinement of the interlayer also lead to higher selectivity in certain reactions.[7]

1.3.2 Paper Coating

In the paper industry, clay minerals from the kaolinite group are used to coat paper to improve its printability. The coating fills up the voids and crevices between fibres on the paper surface, making it more even, with smaller pores and a narrower pore size distribution.[8] It therefore also enhances the aesthetic qualities of the paper.

1.3.3 Drilling Fluids

Drilling fluids are used in the oil exploration and recovery industries to transport cuttings to the surface during drilling operations. The fluid is pumped down the drill stem and rises to the surface in the space between the drill stem and the walls of the hole carrying loose cuttings with it. Once at the surface the cuttings are removed from the fluid, which is then recirculated.

Environmental legislation has meant that current drilling fluids are, in general, water based. In addition to water, they contain a small weight percentage of a clay mineral and also, depending on the conditions, some inorganic/organic additive.

The clay mineral most extensively used in drilling fluids is bentonite; this is the name given to montmorillonite from the Wyoming area of the United States, with sodium as the predominant exchangeable cation. When a small volume percentage is added to water it forms a fluid with ideal rheological properties for a transport medium—high viscosity and thixotropy. These properties ensure that when drilling is stopped the fluid forms a thick gel that suspends the rock cuttings, preventing then from sinking to the bottom of the wellbore. It is, however, possible to obtain drilling fluids with similar rheological properites with other clay minerals. The preference for bentonite arises due to the fact that when used in drilling operations it forms a thin impervious layer on the wall of the borehole, which stabilises the exposed rock formation. The uniqueness of bentonite in this respect is thought to be due to the fact that it is easily dispersed into flakes of almost unit cell thickness, which one can imagine to plaster the surface of the wellbore.[2]

1.3.4 Waste Management

The sorptive properties of clay minerals has led to their use in the containment of domestic, industrial and nuclear waste.

Domestic and Industrial Landfills

European Union landfill regulations have made installation of artificial liner systems mandatory for all landfills, except sites where a suitable low permeability natural liner, such as a clay mineral formation, is present.[9] In either case the liner is required to contain all leachate produced by degredation of the landfill waste and so provide complete protection to all groundwater.

Modern artificial liners are multiple barrier clay-membrane systems, comprising one or two layers of a synthetic membrane, such as high density polyethylene, interlayered with 1m of smectite clay mineral material.[9,10] In the event that pollutants pass through the synthetic membrane, they are expected to be absorbed by the clay mineral material.[10,11]

Nuclear Waste Repositories

The permanent disposal of high level nuclear waste, such as spent nuclear fuel, is a major scientific challenge. Investigations by research groups in different countries have led to the proposal of similar multiple barrier systems.[12–14] The general concept is to seal the nuclear waste in corrosion-resistant copper containers, deposit these in engineered repositories 500-1000m deep in a geological formation and surround them with a compacted, smectite-clay-based buffer material.

The intended role of the clay-based buffer material is two-fold. In the first instance it would protect the container from minor movements in the surrounding geological formation. In the second instance its sorbtive properties would prevent groundwater flow around the container and also at a later stage retard migration of leached radionuclides from corroded canisters.

Studies looking at the properties of smectite clay minerals with a view to their use as buffer materials for nuclear waste repositories have included investigation of long-term stability,[15] thermomechanical properties,[16,17] swelling behaviour,[18,19] and ion diffusion.[18–20] Synthetic organophilic clay materials have also been studied.[21,22]

1.3.5 Clay-Polymer Nanocomposites

In recent years there has been considerable interest in clay-polymer nanocomposites due to the novel material properties that they exhibit. They offer enhanced mechanical,[23,24] thermal[25,26] and permeability properties,[27] which has led to a wide range of applications in the automotive, electronics and furnishing industries.

The intrinsic structure of clay-polymer nanocomposites varies depending on their constituents and method of preparation. Two extremes may be used to define the range of possible structures. At one extreme the intercalated polymer chains sit within the clay mineral layers, which are stacked together in a well-ordered manner. Such materials are called *intercalated* or *non-exfoliated* nanocomposites. At the other extreme the clay mineral layers have lost their order and are well-dispersed in a continuous polymer matrix. Such materials are called *delaminated* or *exfoliated* nanocomposites. Some nanocomposites, may of course, contain both ordered and disordered phases. Recent research has mainly focused on the preparation of exfoliated rather than non-exfoliated materials because of their lower density.

1.4 Summary

Clay minerals are naturally occuring materials that comprise silicate layers. In some clay minerals, isomorphic substitution of octahedral and tetrahedral sites by atoms of lower valency causes the layers to be negatively charged. To maintain charge neutrality metal cations reside between the layers. Hydration of the cations provides the driving force for the adsorption of water. These structural features give rise to their physical and chemical properties which lead to a range of applications.

Chapter 2

First Principles Simulation

This chapter provides a short discription of the advantages and disadvantages of both first principles and classical simulation and the types of problems each is particularly useful for studying. It goes on to describe some of the fundamental concepts of molecular quantum mechanics: the time-independent Schrödinger equation, Born-Oppenheimer approximation and variation principle. This is followed by an outline of Hartree-Fock theory, which lays the foundation for an overview of density functional theory.

2.1 First Principles or Classical Simulation?

First principles (or *ab initio*) simulations attempt to solve–to a good approximation–the equations of quantum mechanics, in order to model the interactions between electrons and nuclei in the system under study. In classical simulations, however, there is no description of interactions at the sub-atomic scale, instead atoms are considered as a single unit and interactions between them modelled by potential functions from classical physics.

The only input data required for a first principles simulation is the atomic number and position of the nuclei and the total number of electrons. In a classical simulation, by contrast one must also provide a set of suitable parameters for the interaction

potential functions, known as a force-field. Force-field parameters are derived from empirical data and/or quantum mechanical calculations on a finite set of systems. There is therefore a question as to how well a force-field is able to simulate the properties of compounds dissimilar to those from which it was derived. This kind of uncertainty is not encountered in *ab initio* simulations where the approximations made are system independent.

If one is interested in the electron dynamics of a system–such as bond making-bond breaking–one must perform a first principles simulation, since only they have explicit representation of electrons. This however, comes with a huge associated computational cost—at present electronic structure calculations are limited to systems of up to hundreds of atoms, even when using large parallel machines. On the other hand, if one is interested in phenomena predominantly governed by non-bonded interactions, classical simulations are often preferable. The use of simple inter-atomic potentials means that they are able to handle up to millions of atoms and therefore model much larger and more realistic systems.

In the present work, our interest in bond formation neccessitates the use of first principles simulation, described next.

2.2 Elementary Quantum Mechanics

In this section we give a very brief overview of the basics of quantum mechanics.

2.2.1 The Time-Independent Schrödinger Equation

The fundamental basis of first principles simulation methods is the time-independent, non-relativistic *Schrödinger equation*:

$$\hat{H}\Psi = E\Psi \tag{2.1}$$

In the context of a system of N electrons and M nuclei $\hat{H}$ is defined as the Hamiltonian operator, Ψ the electronic and nuclear wavefunction, and E the total energy.

The Hamiltonian operator for such a system may be written as:

$$\hat{H} = -\frac{1}{2}\sum_{i=1}^{N}\nabla_i^2 - \frac{1}{2}\sum_{A=1}^{M}\frac{1}{M_A}\nabla_A^2 - \sum_{i=1}^{N}\sum_{A=1}^{M}\frac{Z_A}{r_{iA}} + \frac{1}{2}\sum_{i=1}^{N}\sum_{j\neq i}^{N}\frac{1}{r_{ij}} + \frac{1}{2}\sum_{A=1}^{M}\sum_{B\neq A}^{M}\frac{Z_A Z_B}{R_{AB}}. \quad (2.2)$$

In this expression the first two terms define the kinetic energy of the electrons and the kinetic energy of the nuclei, while the remaining three describe the potential energy arising from electron-nucleus, electron-electron and nucleus-nucleus electrostatic interactions, respectively. In this text atomic units are used throughout such that $h/2\pi = m_e = 4\pi\varepsilon_0 = 1$, where h is Planck's constant, m_e is the mass of an electron and ε_0 is the permittivity of free space. In this notation M_A, the mass of nucleus A, must be given in multiples of the mass of an electron, the unit of length is Bohrs and the unit of energy Hartrees. The other terms are r_{pq} and R_{pq}, the distance between particles p and q; and Z_A the atomic charge on nucleus A. The Laplacian, ∇_i^2, is the sum of the differential operators, which in Cartesian coordinates has the form:

$$\nabla_i^2 = \frac{\partial^2}{\partial x_i^2} + \frac{\partial^2}{\partial y_i^2} + \frac{\partial^2}{\partial z_i^2}. \quad (2.3)$$

According to the postulates of quantum mechanics, the energy and properties of a stationary state of a system of microscopic particles are obtained from the solution of the Schrödinger equation. To determine such solutions, one must make a series of approximations.

2.2.2 The Born-Oppenheimer Approximation

The first simplification made is the *Born-Oppenheimer approximation* which states that, since the nuclei are much heavier than the electrons, it is possible to separate their motion.[28] The nuclei move relatively slowly and so the electrons are presummed to follow their motion adiabatically—that is the electrons respond almost instantaneously to changes in the position of the nuclei. The electrons can therefore be assumed to be moving in an external field created by the fixed nuclei.

If the nuclei are considered fixed their kinetic energy is zero and the nucleus-nucleus repulsion term is equal to a constant. Thus the total Hamiltonian may be simplified to give the electronic Hamiltonian:

$$\hat{H}_{elec} = -\frac{1}{2}\sum_{i=1}^{N}\nabla_i^2 - \sum_{i=1}^{N}\sum_{A=1}^{M}\frac{Z_A}{r_{iA}} + \frac{1}{2}\sum_{i=1}^{N}\sum_{j\neq i}^{N}\frac{1}{r_{ij}}. \tag{2.4}$$

The electronic wavefunction Ψ_{elec} and the electronic energy E_{elec} are solutions of the electronic Schrödinger equation:

$$\hat{H}_{elec}\Psi_{elec} = E_{elec}\Psi_{elec}. \tag{2.5}$$

The total energy of the system is then the sum of the electronic energy and the constant nuclear repulsion term. To optimise ionic positions, the electronic Schrödinger equation may be solved for different nuclear arrangements to obtain a multidimensional potential energy surface (PES).

Since we are nearly always only concerned with solving the electronic Schrödinger equation we will subsequently drop the '*elec*' superscript and use $\hat{H}$, Ψ and E to refer to $\hat{H}_{elec}$, Ψ_{elec} and E_{elec}, respectively.

2.2.3 The Variational Principle

In all but a few very simple cases there is no way to solve the electronic Schrödinger equation exactly for either atomic or molecular systems. One must therefore use the *variational principle* to systematically approach the ground state wavefunction Ψ_0, which will deliver the lowest energy E_0.

The variational principle states that if an arbitrary trial wavefunction is used to calculate the energy of a system, then the value calculated is never less than the true energy, shown by the inequality:

$$\langle\Psi_{trial}|\hat{H}|\Psi_{trial}\rangle \;=\; E_{trial} \;\geq\; E_0 \;=\; \langle\Psi_0|\hat{H}|\Psi_0\rangle, \tag{2.6}$$

where we have used Dirac notation, such that:

$$\langle\Psi|\hat{H}|\Psi\rangle = \int \Psi^*(\mathbf{x}_1,\mathbf{x}_2...\mathbf{x}_N)\hat{H}\Psi(\mathbf{x}_1,\mathbf{x}_2...\mathbf{x}_N)d\mathbf{x}_1,d\mathbf{x}_2...d\mathbf{x}_N. \tag{2.7}$$

2.3 Basis Sets

In order to minimise the expectation value of the electronic energy (2.6) one must search through the infinite number of possible acceptable N electron wavefunctions. Of course, in practise this is impossible, but one can apply the variational principle to a subset of possible functions. The electronic wavefunction is usually approximated using either *localised orbitals* or *planewaves*.

2.3.1 Localised Orbitals

The orbital approximation suggested by Hartree,[29] implies that a many-electron wavefunction may be expressed as a simple product of one-electron wavefunctions. In fact, to adhere to the Pauli principle,[30] it must be an antisymmetrised product. The simplest way to achieve this is to express the many-electron wavefunction as a Slater determinant[31] of one-electron wavefunctions, written as:

$$\Psi = \frac{1}{\sqrt{N!}} \begin{vmatrix} \chi_1(\mathbf{x}_1) & \chi_2(\mathbf{x}_1) & \cdots & \chi_N(\mathbf{x}_1) \\ \chi_1(\mathbf{x}_2) & \chi_2(\mathbf{x}_2) & \cdots & \chi_N(\mathbf{x}_2) \\ \vdots & \vdots & \vdots & \vdots \\ \chi_1(\mathbf{x}_N) & \chi_2(\mathbf{x}_N) & \cdots & \chi_N(\mathbf{x}_N) \end{vmatrix}, \tag{2.8}$$

where $\chi_i(\mathbf{x}_i)$ are the one-electron wavefunctions, $\mathbf{x}_i$ donates both the spatial $\mathbf{r}_i$ and spin ξ_i coordinates of electron i and N is the total number of electrons in the system.

In the localised orbital approach the one-electron wavefunctions, commonly called *spin orbitals*, are expanded as a product of a spatial $\psi_i(\mathbf{r}_i)$ and spin $\eta_i(\xi_i)$ function such that $\chi_i(\mathbf{x}_i) = \psi_i(\mathbf{r}_i)\eta_i(\xi_i)$. In turn, the spatial functions, or *molecular orbitals* are expressed as a linear combination of *atomic orbtials* (LCAO):[32,33]

$$\psi_i = \sum_{\mu=1}^{m} c_{i\mu}\phi_\mu, \tag{2.9}$$

where m is the number of atomic orbitals ϕ_μ used to describe the molecular orbital and $c_{i\mu}$ are the atomic orbital coefficients calculated self-consistently, as discussed

in Section 2.4.2. The spin functions may take one of two values, usually denoted $\eta_i(\alpha)$ and $\eta_i(\beta)$ corresponding to the usual spin-up or spin-down picture. Thus each molecular orbital may accommodate two electrons, one in each of the two spin states.

In a similar way, atomic orbitals are almost always constructed as a linear combination of Gaussian functions, called contracted Gaussian-type orbitals. The preferred use of Gaussian functions is due to their favourable algebraic properties which make integral evaluation easier during calculations.

Basis sets of different degrees of accuracy are defined by the number and type of atomic orbitals they assign to each atom type. One can see that maximum accuracy is obtained when the number of atomic orbitals used in the linear expansion (2.9) is infinite. In practice it is usually chosen to be as high as possible taking into consideration the computational resources available.

The localised orbital representation of a wavefunction is well suited to the study of atoms and molecules, since the orbitals are centred on the atoms. In the limit of a finite basis set however, the localisation of atomic orbitals causes problems.

In first principles simulations, forces on atoms can, in theory, be taken to be the Hellman-Feynman forces,[34] determined analytically from the derivative of the total energy with respect to nuclear coordinates. The Hellman-Feynman theorem is, however, only valid when the wavefunction used is an exact eigenfunction of the Hamiltonian, which is never the case since a finite basis set is always employed. Therefore, in practise, one must also calculate contributions due to variations in the wavefunction, known as Pulay forces.[35] In contrast, Pulay forces are not present when a finite size, position independent basis set is used.

In the theory of quantum mechanics there is a finite probability of an electron being anywhere in space. In using localised atomic orbitals we restrict the location of the electrons. This gives rise to so called basis set superposition errors (BSSE),[36] which are particularly noticeable when calculating binding energies. They come about because individual fragments of a structure are able to make use of the basis functions of other fragments. Thus each fragment utilises a basis set larger than

that available to it when in isolation. This results in calculated binding energies being too attractive. It is possible to estimate basis set superposition errors by the counterpoise method,[36] which computes the energies of individual fragments using the basis set of the complete system.

One further problem associated with the localised orbital approach is that there is no systematic way of improving the quality of a basis set. This means that to demonstrate convergence it is often necessary to perform a series of calculations on a system, using basis sets not only of increasing size, but also different form.

2.3.2 Planewaves

In order to better model the continuum properties of extended systems, such as crystalline solids, it is often useful to make the supercell approximation.[37] In this approach a system is modelled by a relatively small unit cell with periodic boundary conditions applied.

If the supercell approximation is made, a different description of the electronic wavefunction may be used. In this prescription the electronic wavefunction is still constructed as a Slater determinant of one-electron wavefunctions (2.8), but the periodicity of the cell means that it is possible to describe the one-electron wavefunctions by an expanded planewave basis set rather than localised orbtials.

The planewave representation of the one-electron wavefunctions is based upon *Bloch's Theorem*,[38] which states that in a periodic system the eigenstates of a one-electron Hamiltonian can be chosen to have the form of a planewave multiplied by a function with the periodicity of the Bravis lattice:

$$\psi_{n\mathbf{k}}(\mathbf{r}) = e^{i\mathbf{k}\cdot\mathbf{r}} u_{n\mathbf{k}}(\mathbf{r}), \tag{2.10}$$

where $\mathbf{k}$ is a wavevector, defined by the reciprical lattice vetors; n is the band index, which occurs because for a given $\mathbf{k}$ there will be many independent eigenstates and $u_{n\mathbf{k}}(\mathbf{r})$ is a function with the periodicity of the crystal lattice.

The periodic function can be expressed in terms of a basis set consisting of a discrete set of planewaves, whose wavevectors are reciprical lattice vectors $\mathbf{G}$:

$$u_{n\mathbf{k}}(\mathbf{r}) = \sum\nolimits_{\mathbf{G}} c_{n\mathbf{k},\mathbf{G}} e^{i\mathbf{G}\cdot\mathbf{r}}. \tag{2.11}$$

Therefore each one-electron wavefunction can be written as a sum of planewaves:

$$\psi_{n\mathbf{k}} = \sum\nolimits_{\mathbf{G}} c_{n,\mathbf{k}+\mathbf{G}} e^{i(\mathbf{k}+\mathbf{G})\cdot\mathbf{r}}. \tag{2.12}$$

There are two potential difficulties with the practical use of this equation. In theory, the summation is over an infinite number of reciprocal lattice vectors. In addition, to calculate the correct band structure the calculation needs to be performed for all allowed wavevectors, in the Brillouin zone. However, some approximations can be made to overcome these problems.

In practise, it is found that summation over a finite number of reciprocal lattice vectors yields sufficient accuracy. The coefficients $c_{n,\mathbf{k}+\mathbf{G}}$ for the planewaves with small kinetic energy are usually more important than those with larger kinetic energy, which are much higher than acccessible physical energies. It is therefore possible to make an approximation and truncate the planewave basis set so as to include only planewaves with energies less than a certain kinetic energy cut-off E_c, given by:

$$E_c = \frac{\hbar^2(\mathbf{k}+\mathbf{G})^2}{2m}. \tag{2.13}$$

Since electronic wavefunctions with wavevectors in close proximity to each other will be almost identical, it is possible to represent the electronic wavefunctions over a region of $\mathbf{k}$-space by a single wavevector. In this way the electronic states at only a finite set of wavevectors are required to calculate the electronic potential and hence the total energy of the system. Several schemes for selecting a suitable set of wavevectors exist, one of the most popular and also the one used in this work is that described by Monkhorst and Pack.[39,40] Since the volume of the reciprocal lattice is inversely proportional to the volume of the real-space cell, for very large systems it may only be necessary to consider one wavevector.

In spite of this, the use of planewaves to describe electronic wavefunctions is impeded by the vast number of planewaves required to expand tightly bound core orbitals and follow the rapid oscillations of the wavefunctions of the valence electrons in the core region, which make it too computational expensive. In order to reduce the number of planewaves required, planewave basis sets are almost always used in conjunction with *pseudopotentials*.[41]

The pseudopotential approximation exploits the fact that the core electrons of an atom are relatively uneffected by the atomic enviroment and it is the valence eletrons that are largely responsible for chemical bonding and physical properties. The core electrons and ionic potential are replaced by a weaker pseudopotential, which acts on a set of pseudowavefunctions rather than the true electronic wavefunctions. Pseudopotentials are, constructed in such a way that the pseudowavefunctions show the same shape as the true wavefunctions outside the core region, but with no radial nodes inside. In this way the number of planewaves required to expand the electronic wavefunctions is dramatically reduced. In addition, removal of the core electrons means that there are less one-electron wavefunctions to be calculated.

The removal of core electrons also has an impact on the calculated total energy, which is typically a thousand times smaller than that which would be obtained from an all-electron calculation. This dictates that in pseudopotential calculations only energy differences are meaningful.

In general, two criteria are used to classify different types of pseudopotential. A *local* pseudopotential is one which uses the same potential for all the angular momentum components of the wavefunctions, whereas a *non-local* pseudopotential uses different potentials for the different angular momentum components. A *norm conserving* pseudopotential is one for which the integral of the squared amplitudes of the wavefunction and pseudowavefunction are identical, such that they generate identical electron densities. The pseudopotentials used in this work were the ultrasoft pseudopotentials of Vanderbilt[42] and the Troullier-Martins pseudopotentials[43] in Kleinman-Bylander form.[44]

Although the planewave approach is naturally suited to the study of crystalline materials, it can be used to describe any system in a periodic cell provided that the cell is large enough to eliminate spurious intereactions caused by the artificial periodicity, called finite size effects. The use of planewaves rather than localised orbitals has several benefits. For example, since planewaves are not dependent on atomic positions, for a fixed unit cell there are no Pulay contributions to the forces on atoms. The independence of planewaves from atomic positions also means that basis set superposition errors are not encountered. In addition, the quality of a basis set can be systematically improved by increasing the number of wavevectors considered and the kinetic energy cut-off, normally done until the total energy converges to a predefined accuracy.

One drawback of the planewave description is that the number of planewaves required for a calculation increases with the volume of the simulation cell, instead of the number of atoms, as in the localised orbital apporoach. It is therefore less efficient for the study of systems which exhibit large amounts of unoccupied space.

2.4 Hartree-Fock Theory

The variational principle implies that the ground state electronic energy of a system may be determined by varying the electronic wavefunction to minimise the expectation value of the electronic energy $\langle\Psi|\hat{H}|\Psi\rangle$, while maintaining the orthonormallity of the spin orbitals *i.e.* $\langle\chi_i|\chi_j\rangle = \delta_{ij}$. This is acheived by the *method of Lagrange undetermined multipliers*, as described in detail by Szabo and Ostlund,[45] such that we minimise the expression:

$$\langle\Psi|\hat{H}|\Psi\rangle \; - \; \sum_{i=1}^{N}\sum_{j=1}^{N}\epsilon_{i,j}\langle\chi_i|\chi_j\rangle \; - \; \delta_{i,j} = \; 0, \tag{2.14}$$

where $\epsilon_{i,j}$ are called the *Lagrange multipliers.*

In practise this means that the coefficients of the molecular orbitals are varied until a minimum value is obtained.

2.4.1 The Hartree-Fock Equations

The many-electron Hamiltonian (2.5) contains three terms. The first two terms are single-particle operators and last term is a two-particle operator. The expectation value of the many-electron Hamiltonian is therefore given by:

$$\begin{aligned}\langle\Psi|\hat{H}|\Psi\rangle &= \sum_{i=1}^{N}\int d\mathbf{x}_1\chi_i^*(\mathbf{x}_1)[-\frac{1}{2}\nabla_1^2-\sum_{A=1}^{M}\frac{Z_A}{r_{1A}}]\chi_i(\mathbf{x}_1)\\ &+ \frac{1}{2}\sum_{i=1}^{N}\sum_{j=1}^{N}[\int d\mathbf{x}_1\int d\mathbf{x}_2\chi_i^*(\mathbf{x}_1)\chi_j^*(\mathbf{x}_2)\frac{1}{r_{12}}\chi_i(\mathbf{x}_1)\chi_j(\mathbf{x}_2)\\ &- \int d\mathbf{x}_1\int d\mathbf{x}_2\chi_i^*(\mathbf{x}_1)\chi_j^*(\mathbf{x}_2)\frac{1}{r_{12}}\chi_i(\mathbf{x}_2)\chi_j(\mathbf{x}_1)] \qquad (2.15)\end{aligned}$$

Substition of (2.15) into (2.14) and variation of the wavefunctions leads, after some mathematical manipulation, to the (canonical) *Hartree-Fock equations*:

$$\hat{f}_i(\mathbf{x}_1)\chi_i(\mathbf{x}_1)=\epsilon_i\chi_i(\mathbf{x}_1), \qquad for\ i\ =\ 1,2,3...N, \qquad (2.16)$$

where $f_i(\mathbf{x}_1)$ is the *Fock operator* given by:

$$\hat{f}_i(\mathbf{x}_1) = -\frac{1}{2}\nabla_1^2-\sum_{A=1}^{M}\frac{Z_A}{r_{1A}}+\sum_{j=1}^{N}[\hat{J}_j(\mathbf{x}_1)-\hat{K}_j(\mathbf{x}_1)], \qquad (2.17)$$

here $\hat{J}_j(\mathbf{x}_1)$ is the *Coulomb operator*, which represents the electrostatic potential an electron at position $\mathbf{x}_1$ experiences due to the average charge distribution of another electron in spin orbital χ_j:

$$\hat{J}_j(\mathbf{x}_1)\chi_i(\mathbf{x}_1) = \int d\mathbf{x}_2\chi_j(\mathbf{x}_2)\chi_j^*(\mathbf{x}_2)\frac{1}{r_{12}}\chi_i(\mathbf{x}_1), \qquad (2.18)$$

and $\hat{K}_j(\mathbf{x}_1)$ is the *exchange operator*, which has no classical interpretation, but arises due to the correlation of the motion of electrons with parallel spin:

$$\hat{K}_j(\mathbf{x}_1)\chi_i(\mathbf{x}_1) = \int d\mathbf{x}_2\chi_j(\mathbf{x}_1)\chi_j^*(\mathbf{x}_2)\frac{1}{r_{12}}\chi_i(\mathbf{x}_2); \qquad (2.19)$$

and the Lagrange multipliers ϵ_i have the physical interpretation of orbital energies.

We note in passing, that in the double summation of (2.15), the term $i = j$ is allowed and therefore includes the unphysical electrostatic interaction of an electron with itself. This problem is however very neatly dealt with, since when $i = j$ the Coulomb and exchange integrals cancel exactly.

The total electronic energy can then be calculated as the sum of the one-electron energies minus half of the Coulomb and exchange energies, otherwise counted twice:

$$E_{HF} = \sum_{i=1}^{N} \epsilon_i - \frac{1}{2}\sum_{i=1}^{N}\sum_{j=1}^{N}[\int d\mathbf{x}_1 \int d\mathbf{x}_2 \chi_i^*(\mathbf{x}_1)\chi_j^*(\mathbf{x}_2)\frac{1}{r_{12}}\chi_i(\mathbf{x}_1)\chi_j(\mathbf{x}_2) - \int d\mathbf{x}_1 \int d\mathbf{x}_2 \chi_i^*(\mathbf{x}_1)\chi_j^*(\mathbf{x}_2)\frac{1}{r_{12}}\chi_i(\mathbf{x}_2)\chi_j(\mathbf{x}_1)] \quad (2.20)$$

2.4.2 Self-Consistent Field Method

Since the Coulomb and exchange operators depend upon the one-electron wavefunctions themselves, the Hartree-Fock equations (2.16) must be solved *self-consistently.* In this approach a set of trial one-electron wavefunctions are used to determine the Coulomb and exchange operators. These are then used to solve the equations, which result in a new set of one-electron wavefunctions and their corresponding energies. The states with the lowest energies are occupied and the Coulomb and exchange operators recalculated. This process is repeated interatively until the output potentials are acceptably close to the input potentials. From the variational principle, this self-consistent procedure generates the ground state of the system.

2.5 Post Hartree-Fock Techniques

Since the Coulomb and exchange operators involve the *average* (not *instantaneous*) repulsive interactions between electrons, the energy calculated by the Hartree-Fock method E_{HF} is not the true non-relativistic energy E_0. The difference between these values is known as the *correlation energy* E_c, defined by:

$$E_c = E_0 - E_{HF} \quad (2.21)$$

In fact, equilibrium geometries and relative energies calculated by the Hartree-Fock method are often in good agreement with experimental results. The need to account for electron correlation is more crucial in the study of dispersive effects, which play a major role in intermolecular interactions.

2.5.1 Configuration Interaction

A popular way to incorporate electron correlation into *ab initio* calculations is known as *configuration interaction* (CI), which expresses the multi-electron wavefunction as a linear combination of its ground and excited-state wavefunctions Ψ_j:

$$\Psi = \sum_j c_j \Psi_j, \tag{2.22}$$

where c_j are the expansion coefficients, calculated variationally.

One drawback of configuration interaction is that, unless *full* configuration interaction is used, the calculations are not size consistent *i.e.* the energy of N non-interacting particles is not equal to N times the energy of a single particle. In addition, it also very computational expensive, typically scalling as $O(N^6)$, where N is the number of electrons in the system. The method is therefore only used in cases where the accuracy of the total energy is paramount.

2.5.2 Møller-Plesset Perturbation Theory

A further approach to electron correlation is *Møller-Plesset perturbation theory.*[46] It is based on more general many-body perturbation theory, in which the exact Hamiltonian $\hat{H}$ is expressed as the sum of a zeroth-order Hamiltonian $\hat{H}_0$, which is soluble exactly, and a perturbation $\hat{V}$, which is assumed to be small in comparison:

$$\hat{H} = \hat{H}_0 + \lambda \hat{V}. \tag{2.23}$$

Since $\hat{V}$ is a small perturbation we can write the eigenfunctions Ψ_i and corresponding energies E_i of the exact Hamiltonian as a power series in terms of λ:

$$\Psi_i = \Psi_i^{(0)} + \lambda^1 \Psi_i^{(1)} + \lambda^2 \Psi_i^{(2)} + ... = \sum_{n=0} \lambda^n \Psi_i^{(n)}, \tag{2.24}$$

$$E_i = E_i^{(0)} + \lambda^1 E_i^{(1)} + \lambda^2 E_i^{(2)} + ... = \sum_{n=0} \lambda^n E_i^{(n)}, \tag{2.25}$$

where Ψ_i^0 and E_i^0 are the eigenfunctions and corresponding energies of the zeroth-order Hamiltonian. $E_i^{(n)}$ is known as the nth-order correction to the energy.

Substitution of expressions (2.23), (2.24) and (2.25) into the time-independent Schödinger equation (2.1), followed by equation of coefficients of like powers of λ, multiplication by $\Psi_i^{(0)}$ and integration over all coordinates leads to formulae for the energy contributions. The first three of these are:

$$E_i^{(0)} = \langle \Psi_i^{(0)} | \hat{H}_0 | \Psi_i^{(0)} \rangle \tag{2.26}$$

$$E_i^{(1)} = \langle \Psi_i^{(0)} | \hat{V} | \Psi_i^{(0)} \rangle \tag{2.27}$$

$$E_i^{(2)} = \langle \Psi_i^{(0)} | \hat{V} | \Psi_i^{(1)} \rangle \tag{2.28}$$

In Møller-Plesset perturbation theory the zeroth-order Hamiltonian is taken to be the sum of the one-electron Fock operators:

$$\hat{H}_0 = \sum_{i=1}^{N} \hat{f}_i(\mathbf{x}_1), \tag{2.29}$$

therefore the zeroth-order energy is equal to the sum of the energies of the occupied spin orbitals:

$$E_0^{(0)} = \sum_{i=1}^{N} \epsilon_i. \tag{2.30}$$

The true Hamiltonian is equal to the sum of the kinetic energy, nuclear attraction and electron repulsion terms, hence the perturbation is given by:

$$\hat{V} = \frac{1}{2} \sum_{i=1}^{N} \sum_{j=1}^{N} \frac{1}{r_{ij}} - \sum_{i=1}^{N} \sum_{j=1}^{N} [\hat{J}_j(\mathbf{x}_1) - \hat{K}_j(\mathbf{x}_1)], \tag{2.31}$$

and the first-order energy correction is:

$$\begin{aligned} E_0^{(1)} &= -\frac{1}{2} \sum_{i=1}^{N} \sum_{j=1}^{N} [\int d\mathbf{x}_1 \int d\mathbf{x}_2 \chi_i^*(\mathbf{x}_1) \chi_j^*(\mathbf{x}_2) \frac{1}{r_{12}} \chi_i(\mathbf{x}_1) \chi_j(\mathbf{x}_2) \\ &\quad - \int d\mathbf{x}_1 \int d\mathbf{x}_2 \chi_i^*(\mathbf{x}_1) \chi_j^*(\mathbf{x}_2) \frac{1}{r_{12}} \chi_i(\mathbf{x}_2) \chi_j(\mathbf{x}_1)]. \end{aligned} \tag{2.32}$$

It can therefore be seen that the sum of the zeroth-order energy and first-order energy correction is equal to the Hartree-Fock energy:

$$E_{HF} = E_0^{(0)} + E_0^{(1)}. \tag{2.33}$$

To obtain an improvement on Hartree-Fock theory it is therefore necessary to use Møller-Plesset perturbation theory to at least second-order, referred to as the MP2 level of accuracy. The only new information required to obtain the MP2 energy is the first-order wavefunction, which may be expressed as a linear combination of solutions to the zeroth-order Hamiltonian $\Psi_j^{(0)}$:

$$\Psi_0^{(1)} = \sum_j c_j \Psi_j^{(0)}, \tag{2.34}$$

where $\chi_j^{(0)}$ include excitations, obtained by promoting electrons into virtual orbitals. This leads to the following expression:

$$E_0^{(2)} = \sum_j \frac{|\langle \Psi_0^{(0)} | \hat{V} | \Psi_j^{(0)} \rangle|^2}{E_0^{(0)} - E_j}, \tag{2.35}$$

which can be expanded in terms of ground-state and virtual spin orbitals:

$$E_0^{(2)} = \frac{1}{4} \sum_a \sum_b \sum_r \sum_s \frac{|\langle ab||rs\rangle|^2}{\epsilon_a + \epsilon_b - \epsilon_r - \epsilon_s}, \tag{2.36}$$

where the sum over a and b corresponds to all ground-state spin orbitals, the sum over r and s corresponds to all virtual spin orbitals and

$$\begin{aligned} \langle ab||rs\rangle &= \int d\mathbf{x}_1 \int d\mathbf{x}_2 \chi_a^*(\mathbf{x}_1)\chi_b^*(\mathbf{x}_2)\frac{1}{r_{12}}\chi_r(\mathbf{x}_1)\chi_s(\mathbf{x}_2) \\ &- \int d\mathbf{x}_1 \int d\mathbf{x}_2 \chi_a^*(\mathbf{x}_1)\chi_b^*(\mathbf{x}_2)\frac{1}{r_{12}}\chi_r(\mathbf{x}_2)\chi_s(\mathbf{x}_1)]. \end{aligned} \tag{2.37}$$

If we set $\lambda = 1$, the energy at the MP2 level can be calculated as:

$$E_0 = E_0^{(0)} + E_0^{(1)} + E_0^{(2)}. \tag{2.38}$$

Møller-Plesset perturbation theory is a size consistent method. In addition, it is also a relatively cheap way to incorporate correlation effects, with scaling of an MPn calculation being of the order $O(N^{(n+3)})$. The main disadvantage of it is that it is non-variational and therefore it is possible to obtain energies lower than the exact energy. A simpler way to account for electron correlation is given by density functional theory.

2.6 Density Functional Theory

Density functional theory (DFT) provides a valuable alternative to the more conventional quantum mechanical methods. It is still in principle an *ab initio* technique since it is based on a parameter free theory, although as will soon be clear, it also possesses some empirical elements.

The basis of density functional theory is similar to that of Hartree-Fock theory, indeed the Born-Oppenheimer approximation is made and consequently the problem it attempts to solve is identical: to find the ground-state energy of a system of interacting electrons moving in an electric field generated by an arrangement of fixed nuclei. The formularisation of the two theories is also very similar, in that both reduce the problem to a set of one-electron eigenvalue equations, which must be solved self-consistently.

The most prominent difference between density functional theory and other quantum mechanical schemes is the change in central quantity from a many-electron wavefunction to the electron density. In addition, the kinetic energy of the electrons is calculated in a subtlely different way, which makes use of the fact that a Slater determinant is an *exact* eigenfunction of a Hamiltonian operator that describes a system of non-interacting electrons moving in an external potential. In addition, the non-classical electron-electron interactions are calculated in an alternative manner, which not only incorporates correlation effects, but also results in a substantial reduction in computational cost. This means that density functional methods can be applied advantageously to much larger systems.

It is no surprise then that the use of density functional methods has increased enormously over the last fifteen years, undoubtedly in part due to the success of the molecular dynamics method of Car and Parrinello.[47] The great importance of the method and its application in simulation was recognised by the award of the 1998 Nobel Prize in chemistry to Walter Kohn and John Pople who both played significant roles in its early development.

2.6.1 The Hohenberg-Kohn Theorem

Density functional theory is based on the Hohenberg-Kohn theorem,[48] which states that for a system of N interacting electrons, moving in an external potential $V_{ext}(\mathbf{r})$ provided by fixed nuclei, we can define an energy functional:

$$E[\rho(\mathbf{r})] = F[\rho(\mathbf{r})] + \int d\mathbf{r} V_{ext}(\mathbf{r})\rho(\mathbf{r}), \tag{2.39}$$

where $F[\rho(\mathbf{r})]$ is a *universal* functional of the electron density $\rho(\mathbf{r})$ independent of both $V_{ext}(\mathbf{r})$ and N, given by:

$$F[\rho(\mathbf{r})] \equiv \langle \Psi | \hat{H} | \Psi \rangle, \tag{2.40}$$

here $\hat{H}$ is a Hamiltonian operator, expressed as:

$$\hat{H} = -\frac{1}{2}\sum_{i=1}^{N}\nabla_i^2 + \frac{1}{2}\sum_{i=1}^{N}\sum_{j\neq i}^{N}\frac{1}{r_{ij}}; \tag{2.41}$$

and the ground state electron density $\rho_0(\mathbf{r})$ minimises the energy functional to give the ground-state electronic energy $E_0[\rho_0(\mathbf{r})]$.

In the same paper, Hohenberg and Kohn went on to show that it is convenient to separate out the classical Coulomb energy of the system from $F[\rho(\mathbf{r})]$ to give:

$$F[\rho(\mathbf{r})] = \frac{1}{2}\int d\mathbf{r}_1 \int d\mathbf{r}_2 \frac{\rho(\mathbf{r}_1)\rho(\mathbf{r}_2)}{r_{12}} + G[\rho(\mathbf{r})], \tag{2.42}$$

where $G[\rho(\mathbf{r})]$ is also a universal functional of the electron density like $F[\rho(\mathbf{r})]$. Substitution of this expression into equation (2.39) leads to:

$$E[\rho(\mathbf{r})] = \int d\mathbf{r} V_{ext}(\mathbf{r})\rho(\mathbf{r}) + \frac{1}{2}\int d\mathbf{r}_1 \int d\mathbf{r}_2 \frac{\rho(\mathbf{r}_1)\rho(\mathbf{r}_2)}{r_{12}} + G[\rho(\mathbf{r})] \tag{2.43}$$

2.6.2 The Kohn-Sham Equations

Kohn and Sham continued the formulation of density functional theory with the introduction of the concept of a non-interacting reference system[49] and expanded the functional $G[\rho(\mathbf{r})]$ as:

$$G[\rho(\mathbf{r})] \equiv T_s[\rho(\mathbf{r})] + E_{xc}[\rho(\mathbf{r})], \tag{2.44}$$

where $T_s[\rho(\mathbf{r})]$ is the kinetic energy of a system of non-interacting electrons moving in an effective potential $V_S(\mathbf{r})$, with the same total density as the actual system of interacting electrons, defined as:

$$T_s[\rho(\mathbf{r})] = -\frac{1}{2}\sum_{i=1}^{N}\int d\mathbf{r}\varphi_i^*(\mathbf{r})\nabla^2\varphi_i(\mathbf{r}), \tag{2.45}$$

with $\varphi_i(\mathbf{r})$, the one-electron wavefunctions of the non-interacting reference system, known as the *Kohn-Sham orbitals*, being analogous to the $\chi_i(\mathbf{x})$ in the Hartree-Fock method and related to the real system of interacting electrons by the expression:

$$\rho(\mathbf{r}) = \sum_{i=1}^{N}|\varphi_i(\mathbf{r})|^2; \tag{2.46}$$

and $E_{xc}[\rho(\mathbf{r})]$, is defined as the exchange-correlation energy of the actual system, which in addition to the non-classical contributions of self-interaction correction, exchange and Coulomb correlation, also includes the difference in the kinetic energy of the non-interacting reference system and the real interacting system of electrons.

Substitution of equation (2.44) into equation (2.43), leads to the full expression for the energy functional:

$$\begin{aligned} E[\rho(\mathbf{r})] &= T_s[\rho(\mathbf{r})] + \int d\mathbf{r}V_{ext}(\mathbf{r})\rho(\mathbf{r}) \\ &+ \frac{1}{2}\int d\mathbf{r}_1\int d\mathbf{r}_2\frac{\rho(\mathbf{r}_1)\rho(\mathbf{r}_2)}{r_{12}} + E_{xc}[\rho(\mathbf{r})], \end{aligned} \tag{2.47}$$

which is calculable exactly provided the forms of the effective potential $V_S(\mathbf{r})$ and exchange-correlation functional $E_{xc}[\rho(\mathbf{r})]$ are known.

In order to minimise the energy we must vary $\rho(\mathbf{r})$ over all densities containing N electrons. This is achieved by the method of Lagrange undetermined multipliers, where μ is chosen so that $\int\rho(\mathbf{r})d\mathbf{r} = N$, such that we have:

$$\frac{\delta}{\delta\rho(\mathbf{r})}[E[\rho(\mathbf{r})] - \mu\int d\mathbf{r}\rho(\mathbf{r})] = 0, \tag{2.48}$$

which, using expansion (2.47), leads to:

$$\frac{\delta T_s[\rho(\mathbf{r})]}{\delta\rho(\mathbf{r})} + V_{ext}(\mathbf{r}) + \int d\mathbf{r}_2\frac{\rho(\mathbf{r}_2)}{r_{12}} + \frac{\delta E_{xc}[\rho(\mathbf{r})]}{\delta\rho(\mathbf{r})} = \mu, \tag{2.49}$$

where we define the Coloumb potential:

$$V_c(\mathbf{r}) = \int d\mathbf{r}_2 \frac{\rho(\mathbf{r}_2)}{r_{12}}, \tag{2.50}$$

and the exchange-correlation potential:

$$V_{xc}(\mathbf{r}) = \frac{\delta E_{xc}[\rho(\mathbf{r})]}{\delta \rho(\mathbf{r})}. \tag{2.51}$$

If we now specify a new potential $V_{eff}(\mathbf{r})$, such that:

$$V_{eff}(\mathbf{r}) = V_{ext}(\mathbf{r}) + V_c(\mathbf{r}) + V_{xc}(\mathbf{r}), \tag{2.52}$$

equation (2.49) can be rewritten as:

$$\frac{\delta T_s[\rho(\mathbf{r})]}{\delta \rho(\mathbf{r})} + V_{eff}(\mathbf{r}) = \mu, \tag{2.53}$$

which is exactly the same equation we would obtain for a system of non-interacting electrons moving in an external potential $V_{eff}(\mathbf{r})$. Thus $V_{eff}(\mathbf{r})$ must equal $V_S(\mathbf{r})$, the potential experienced by the electrons in the non-interacting reference system.

This implies that to find the ground-state electron density of the non-interacting reference system we solve the one-electron Schrödinger equations:

$$[-\frac{1}{2}\nabla^2 + V_{eff}(\mathbf{r})]\varphi_i(\mathbf{r}) = \varepsilon_i \varphi_i(\mathbf{r}) \qquad i = 1, 2, 3...N, \tag{2.54}$$

known as the *Kohn-Sham equations* and analogous to the Hartree-Fock equations. The electron density can then be constructed from equation (2.46). Since $V_{eff}(\mathbf{r})$ depends on the electron density itself, the equations must be solved self-consistently.

The energy of the real system of interacting electrons can then be calculated as:

$$E[\rho(\mathbf{r})] = \sum_{i=1}^{N} \varepsilon_i - \frac{1}{2} \int d\mathbf{r}_1 \int d\mathbf{r}_2 \frac{\rho(\mathbf{r}_1)\rho(\mathbf{r}_2)}{r_{12}} - \int d\mathbf{r} V_{xc}(\mathbf{r})\rho(\mathbf{r}) + E_{xc}[\rho(\mathbf{r})], \tag{2.55}$$

where the first term is the total electronic ground state energy of the system with the non-interacting electrons moving in an external potential $V_{eff}(\mathbf{r})$. The second and third terms collectively subtract the excess energy included in the first term, caused by the electrons moving in an external potential $V_{eff}(\mathbf{r})$ instead of $V_{ext}(\mathbf{r})$ and also return the Coulomb energy of the system of interacting electron moving in an external potential $V_{ext}(\mathbf{r})$. The last term is the exchange-correlation energy of the system of interacting electrons moving in an external potential $V_{ext}(\mathbf{r})$.

2.6.3 Exchange-Correlation Functionals

Thus far, no reference has been made to the precise form of $E_{xc}[\rho(\mathbf{r})]$ the exchange-correlation functional. It is very important to appreciate that if it were known, density functional theory would provide a theoretical method by which the *exact* ground-state electronic energy of a system of interacting electrons may be calculated. Of course, in general it is unknown and must therefore be approximated.

The Exchange-Correlation Hole

Before proceeding to discuss approximations to the exchange-correlation functional, it is helpful to briefly describe the concept of *the exchange-correlation hole*,[50–52] which is a useful way to visualise the difference in the uncorrelated and correlated probability of finding an electron at a particular point in co-ordinate space.

In a system of interacting electrons there is said to be an exchange-correlation hole associated with each distinct pair of electrons. For an arbitrary pair of electrons, with the coordinates $\mathbf{x}_1$ and $\mathbf{x}_2$, the associated exchange-correlation hole $h_{xc}(\mathbf{x}_1;\mathbf{x}_2)$, can be expressed as:

$$h_{xc}(\mathbf{x}_1;\mathbf{x}_2) = \frac{\rho_2(\mathbf{x}_1;\mathbf{x}_2)}{\rho(\mathbf{x}_1)} - \rho(\mathbf{x}_2), \tag{2.56}$$

where $\rho(\mathbf{x}_i)$ is what has thus far been referred to as the *electron density*, but more strictly speaking is a probability density—the probability of finding an electron of arbitrary spin within the volume element $d\mathbf{r}_i$, while the remaining electrons have arbitrary position and spin; and $\rho_2(\mathbf{x}_1;\mathbf{x}_2)$, referred to as the *pair density*, is the probability of simultaneously finding an electron with spin ξ_1 within the volume element $d\mathbf{r}_1$ and another with spin ξ_2 within the volume element $d\mathbf{r}_2$, while the remaining electrons have arbitrary position and spin. The exchange-correlation hole is thus the difference in the probability of finding an electron with spin ξ_2 at $\mathbf{r}_2$, given there is already an electron with spin ξ_1 at $\mathbf{r}_1$ and the uncorrelated probability. The name arises since the presence of the electron at $\mathbf{r}_1$ causes a depletion (*or hole*) in the electron density at $\mathbf{r}_2$, due to the correlation it introduces.

The appeal of the exchange-correlation hole in density functional theory is that it provides a way to quantify the effects of self-interaction and electron correlation. It may be formally separated into two components:

$$h_{xc}(\mathbf{x}_1;\mathbf{x}_2) = h_x(\mathbf{x}_1;\mathbf{x}_2) + h_c(\mathbf{x}_1;\mathbf{x}_2). \tag{2.57}$$

where $h_x(\mathbf{x}_1;\mathbf{x}_2)$ is known as the *Fermi hole* and $h_c(\mathbf{x}_1;\mathbf{x}_2)$ the *Coulomb hole*.

The Fermi hole is the depletion in electron density due to the correlation of the motion of electrons with parallel spin, as implied by the Pauli principle.[30] This type of correlation is included in the Hartree-Fock method, by the antisymmetry of the wavefunction used. The Fermi hole exhibits several important physical properties. Like the total hole, it integrates to -1 for electrons with parallel spin, however for electrons with antiparallel spin it integrates to 0, such that:

$$\int d\mathbf{x}_2 h_x(\mathbf{x}_1;\mathbf{x}_2) = -\delta_{\xi_1\xi_2} \tag{2.58}$$

In addition, because the Pauli principle implies that two electrons of the same spin can never occupy the same position in space, for $\mathbf{x}_2 \rightarrow \mathbf{x}_1$, the Fermi hole must be equal to minus the density of electrons with the same spin as the electron with coordinates $\mathbf{x}_1$, expressed as:

$$h_x(\mathbf{x}_1;\mathbf{x}_2 \rightarrow \mathbf{x}_1) = -\rho(\mathbf{x}_1). \tag{2.59}$$

It can also be shown that the Fermi hole is negative everywhere, denoted by:

$$h_x(\mathbf{x}_1;\mathbf{x}_2) \leq 0. \tag{2.60}$$

The Coulomb hole is the depletion in electron density due to the correlation of the motion of electrons which arises from instantaneous electrostatic repulsions. This type of correlation is not included in the Hartree-Fock method. The Coulomb hole integrates to 0, such that:

$$\int d\mathbf{x}_2 h_c(\mathbf{x}_1;\mathbf{x}_2) = 0 \tag{2.61}$$

The spin and system average of expressions (2.58), (2.60) and (2.61) gives three important conditions for the system-averaged exchange-correlation hole,[51] these are:

$$\int d\mathbf{r}_2 \langle h_x(\mathbf{r}_1;\mathbf{r}_2)\rangle = -1, \tag{2.62}$$

$$\langle h_x(\mathbf{r}_1;\mathbf{r}_2)\rangle \leq 0, \tag{2.63}$$

and

$$\int d\mathbf{r}_2 \langle h_c(\mathbf{r}_1;\mathbf{r}_2)\rangle = 0. \tag{2.64}$$

It must be kept in mind that only the total exchange-correlation hole has real physical meaning. Taken individually, neither the Fermi or Coulomb hole are usually a good representation to the total hole, it is only the sum of the two quantities that yields the correct shape and behaviour.

The exchange-correlation hole may be used to construct an expression for part of the exchange-correlation functional, since it provides a theoretical way to calculate the correction for self-interaction and effects of exchange and Coulomb correlation—these are equal to the sum of the electrostatic interaction between the positive electron density at a point $\mathbf{r}_1$ and the negative electron density contained in the related hole at $\mathbf{r}_2$, summed over all coordinate space. Excluding the difference in the kinetic energy of the non-interacting reference system and the real system of interacting electrons the exchange-correlation functional may thus be expressed as:

$$E_{xc}[\rho(\mathbf{r})] = \frac{1}{2}\int d\mathbf{r}_1 \int d\mathbf{r}_2 \frac{\rho(\mathbf{r}_1)h_{xc}(\mathbf{r}_1;\mathbf{r}_2)}{r_{12}} \tag{2.65}$$

The missing kinetic energy contribution can be incorporated into the exchange-correlation hole via the *adiabatic-connection*.[53] This will not be described here, except to point out that it has no effect on the formal properties of the hole and yields a so called *coupling-constant averaged exchange-correlation hole* $\bar{h}_{xc}(\mathbf{r}_1;\mathbf{r}_2)$, which satisfies the relation:

$$E_{xc}[\rho(\mathbf{r})] = \frac{1}{2}\int d\mathbf{r}_1 \int d\mathbf{r}_2 \frac{\rho(\mathbf{r}_1)\bar{h}_{xc}(\mathbf{r}_1;\mathbf{r}_2)}{r_{12}}, \tag{2.66}$$

a complete, albeit theoretical, expression for the exchange-correlation functional.

Local Density Approximation

One of the simplest ways to approximate the exchange-correlation functional is the *local density approximation* (LDA), the details of which were included in the original paper by Kohn and Sham.[49] This states that assuming the electron density is sufficiently slowly varying the exchange-correlation energy can be calculated from:

$$E_{xc}^{LDA}[\rho(\mathbf{r})] = \int d\mathbf{r}\rho(\mathbf{r})\varepsilon_{xc}(\rho(\mathbf{r})), \tag{2.67}$$

where $\varepsilon_{xc}(\rho(\mathbf{r}))$ is the exchange-correlation energy per particle of a uniform electron gas of density $\rho(\mathbf{r})$. The quantity $\varepsilon_{xc}(\rho(\mathbf{r}))$ can be split into separate exchange and correlation contributions, such that:

$$\varepsilon_{xc}(\rho(\mathbf{r})) = \varepsilon_x(\rho(\mathbf{r})) + \varepsilon_c(\rho(\mathbf{r})), \tag{2.68}$$

where $\varepsilon_x(\rho(\mathbf{r}))$ is the exchange energy per particle of a homogeneous electron gas of density $\rho(\mathbf{r})$, which based on work by Slater,[54] is normally calculated as:

$$\varepsilon_x(\rho(\mathbf{r})) = -\frac{3}{4}\sqrt[3]{\frac{3\rho(\mathbf{r})}{\pi}}, \tag{2.69}$$

and $\varepsilon_c(\rho(\mathbf{r}))$ is the correlation energy per particle of a homogeneous electron gas of density $\rho(\mathbf{r})$, for which analytical expressions have been developed by Vosko, Wilk and Nusair[55] and Perdew and Wang,[56] based on quantum Monte-Carlo simulations of the homogeneous electron gas by Caperly and Alder.[57] These are often referred to as the VWN and PW92 correlation functionals, respectively.

The local density approximation also exists in an unrestricted version, known as the *local spin-density approximation*, where the energy is a functional of the two spin-densities, $\rho_\alpha(\mathbf{r})$ and $\rho_\beta(\mathbf{r})$, instead of the electron density $\rho(\mathbf{r})$, such that:

$$E_{xc}^{LSD}(\rho_\alpha(\mathbf{r}), \rho_\beta(\mathbf{r})) = \int d\mathbf{r}\rho(\mathbf{r})\varepsilon_{xc}(\rho(\mathbf{r}))\rho_\alpha(\mathbf{r})\rho_\beta(\mathbf{r}). \tag{2.70}$$

Somewhat surprisingly, considering that the electron density in most atoms and molecules is far from slowly varying, the local density approximation has proven quite successful, particularly in the calculation of equilibrium geometries. This is

attributed to the fact that the exchange-correlation hole of a uniform electron gas, which is used as a model for the real hole, satisfies the most important relations of a true hole,[58] such as those given by equations (2.62), (2.63) and (2.64). In addition, although the exact shapes of the model and real holes may differ considerably, it is the spherical average which is used to calculate the exchange-correlation energy and these are in much better agreement.

Unfortunately however, the local density approximation fails to produce accurate energetic data. It gives an average absolute error of 36kcal/mol for the atomisation energies of those molecules in the G2 data set,[58] which is better than Hartree-Fock level calculations, but still far from experimental accuracy. It also performs poorly for hydrogen-bonded systems.[59] These inadequacies have led to the search for better approximate functionals.

Generalised Gradient Approximation

The first step taken to improve the local density approximation was to try and take into account the inhomogeneity of the electron density of real systems, by using information not only about the density $\rho(\mathbf{r})$, at a point $\mathbf{r}$, but also its gradient $\nabla\rho(\mathbf{r})$. The earliest attempt of this nature was the *gradient expansion approximation* (GEA). In fact, functionals of this type proved little better, since the exchange-correlation holes associated with them did not exhibit the most important physical properties of a true hole, such as those given by equations (2.62), (2.63) and (2.64). It was thus soon proceeded by the *generalised gradient approximation* (GGA), which not only used information about the density and its gradient, but also enforced most of the important hole properties. Functionals of this type are denoted:

$$E_{xc}^{GGA}[\rho_\alpha(\mathbf{r}),\rho_\beta(\mathbf{r})] = \int d\mathbf{r} f(\rho_\alpha(\mathbf{r}),\rho_\beta(\mathbf{r}),\nabla\rho_\alpha(\mathbf{r}),\nabla\rho_\beta(\mathbf{r})), \tag{2.71}$$

and are usually constructed from separate exchange and correlation contributions:

$$E_{xc}^{GGA}[\rho_\alpha(\mathbf{r}),\rho_\beta(\mathbf{r})] = E_x^{GGA}[\rho_\alpha(\mathbf{r}),\rho_\beta(\mathbf{r})] + E_c^{GGA}[\rho_\alpha(\mathbf{r}),\rho_\beta(\mathbf{r})]. \tag{2.72}$$

The precise forms of $E_x^{GGA}[\rho_\alpha(\mathbf{r}), \rho_\beta(\mathbf{r})]$ and $E_c^{GGA}[\rho_\alpha(\mathbf{r}), \rho_\beta(\mathbf{r})]$ are complicated and will not be discussed here, except to say that they are usually developed on the basis of the accuracy of the results they deliver, rather than any physically meaningful concepts. Indeed, many contain empirical parameters.

Some of the most established gradient-corrected exchange functionals, are those suggested by Becke (B),[60] Perdew and Wang (PW91)[61,62] and Perdew, Burke and Ernzerhof (PBE),[63,64] while for gradient corrected correlation functionals those proposed by Lee, Yang and Parr (LYP)[65] and Perdew and Wang (PW91)[61,62] are amongst the most frequently used.

In theory any combination of exchange and correlation functional is acceptable, however certain pairs have become synonomous. The Becke exchange functional is often used in conjunction with the Lee, Yang and Parr correlation functional to give the BLYP exchange-correlation functional. In addition, the Perdew and Wang exchange and correlation functionals are often coupled together to give the PW91PW91 exchange-correlation functional. These are the two exchange-correlation functionals used in this work.

The generalised gradient approximation leads to much improved energetic data, with the average absolute error for the atomisation energies of those molecules in the G2 data set being reduced to 5-7kcal/mol.[58] It also performs better for hydrogen-bonded systems.[59]

Hybrid Functionals

More recently, several exchange-correlation functionals have been proposed which incorporate a fraction of exact Hartree-Fock exchange, known as *hybrid functionals.* The most common functional of this type is the B3LYP functional of Becke.[66]

Hybrid functionals have proved to be marginally more accurate than gradient corrected functionals with an average absolute error for the atomisation energies of those molecules in the G2 data set of just 2-3kcal/mol.[58] In spite of this, they have still to attain the popularity of gradient corrected functionals.

2.7 Semiempirical Methods

High level *ab initio* calculations based on Hartree-Fock and density functional theory have proved successful in reproducing the properties and behaviour of many chemical systems to experimental accuracy. Until recent years however, their application to all but the smallest systems was prohibited by the huge amount of computational resources required. Historically then, while computational resources were limited, more approximate *semiempirical methods* were developed to enable the quantum mechanical treatment of much larger systems.

In methodology, semiempirical methods lie somewhere in between *ab initio* and classical simulation. They are quantum mechanical in the sense that they have explicit representation of electrons, but are similar to classical simulation methods in that they also utilise empirical parameters derived from experiment.

Most modern semiempirical techniques are based on the Hartree-Fock method, but simplify the calculations by the approximation of many of the difficult-to-calculate integrals (similar in form to those present in equation 2.15). These are either set to zero or approximated by a parameter-dependent function derived from experiment or *ab initio* calculations. In addition, all semiempirical methods perform only valence electron calculations, that is they assume the inner shell electrons (which play little part in chemical behaviour) to be part of the nucleus, acting as an unpolarisable core. This is implemented using pseudopotentials similar to those described in Section 2.3.2. Together, these approximations, result in a significant reduction in computational effort.

There are advantages and disadvantages of introducing empirical parameters into the Hartree-Fock scheme. On the one hand, it is suggested that when parameters are derived from essentially exact experimental results, they in some ill-defined way account for electron correlation and results better than those from Hartree-Fock calculations can be obtained.[37] Obviously when parameters have been determined from Hartree-Fock calculations themselves this is impossible. On the other hand,

just as is the case for force-fields used in classical simulations, there is a question as to how well a particular semiempirical method is able to simulate the properties of compounds dissimilar to those from which it was parameterised.

A number of semiempirical methods exist, which differ mainly in the integrals that they approximate and how they are approximated. The most common are: Complete Neglect of Differential Overlap (CNDO),[67,68] Modified Intermediate Neglect of Differential Overlap 3 (MINDO/3),[69] Austin Model 1 (AM1)[70] and Parametric Method Number 3 (PM3).[71,72] A useful guide to the most suitable semiempirical parameterisations for the study of different types of compound is given by Stewart.[70]

2.8 Summary

First principles simulations model the interaction of electrons and nuclei by the approximate solution of the equations of quantum mechanics. This allows them to simulate many important phenomena that depend explicitly on electron dynamics, such as bond making-bond breaking, which is impossible with classical methods.

Several established first principles methods exist, which differ mainly in the way they treat electron correlation: Hartree-Fock theory includes Fermi correlation by the use of an antisymmetric many-electron wavefunction, but completely neglects Coulomb correlation; Møller-Plesset perturbation theory treats the effect of electron correlation as a perturbation, which can be calculated; and configuration interaction includes electron correlation by the use of a multi-electron wavefunction that is an expansion of ground and excited states. The latter two methods deliver extremely accurate results, but their use is often prohibited by the large computational cost, related in part to the non-local way they calculate Fermi correlation.

Density functional theory however, uses a local exchange-correlation functional to account for electron correlation effects. This makes it the most efficient way to include electron correlation in a calculation. As such, it delivers accurate energies and properties at a relatively low computational cost.

Chapter 3

Simulation of Clay Minerals

Until relatively recently simulation studies of clay minerals were quite rare. In view of the size and complex nature of their structure, they were considered inaccessible as systems to model. It is only with advances in computing hardware and algorithms that theoretical studies of clay minerals have become more common.

Modelling of clay minerals can be particularly helpful to materials scientists since information from experimental methods that analyse clay minerals and their interfaces at the atomic scale are often difficult to interpret. In addition, the small particle size of clay minerals (typically 2-10 μm), combined with the nature of the natural materials, often precludes the use of single-crystal diffraction techniques in structure determination, leading to ambiguities in crystal structure.[2]

The majority of theoretical investigations of clay minerals have been carried out using classical simulation methods, which are well suited to the study of phenomena governed predominantly by non-bonded interactions, but unable to model processes which involve electron dynamics. Electronic structure calculations of clay minerals, which are the focus of the present work, have been inhibited by the computational resources needed to simulate a realistically-sized model. In order to make them more tractable it has been commonplace to approximate the structure of clay minerals by non-periodic, cluster models.[73–92] However, a reduction in computational cost comes at a price and it is almost always necessary to fix some atoms in a cluster model

to reduce deformation at the edges, where broken bonds are simply saturated by hydrogen atoms. The use of periodic models is thus becoming more frequent,[93–101] since they are better able to describe the extended crystal lattice and the confined nature of the interlayer, though care has to be taken to minimise finite-size effects.

In this chapter we survey studies of clay minerals by first principles methods, with a focus on the results of the simulations and the chemical insight they provide.

3.1 Layer Structure

It has already been mentioned that the small particle size of clay minerals has in many cases prevented their study by single-crystal X-ray diffraction. Therefore clay mineral structures optimised by quantum methods are of real significance.

Early investigations reported relevant structural parameters, such as bond lengths and angles, obtained from optimisations of small cluster models of clay minerals.[73–78] The formulae and associated references of selected models are listed in Table 3.1. The size of the clusters enabled their optimisation by quantum methods. In general, slightly shorter bond lengths and larger angles were determined from Hartree-Fock calculations compared to those from perturbation and density functional methods, which gave similar values. This is particularly evident in the prominent study of Teppen *et al.*,[76] who optimised an array of pertinent clay mineral cluster models, using a range of *ab initio* methods and localised basis sets. The importance of their results proved two-fold. In the first instance they showed that electron-correlation must be included in the optimisations of clay mineral cluster models in order to obtain reasonably accurate structures. In addition, they provide a database for the development of force-field parameters for classical simulations of clay minerals.

One of the problems with such small cluster models is that they do not define a particular clay mineral—their limited size prohibits representation of the subtle variations in layer structures. To obtain more specific structural data, much larger cluster models, discernible as particular clay minerals types, have also been studied.

Table 3.1: Structural Studies of Clay Minerals with Cluster Models

model	associated reference(s)
$Si(OH)_4$	Luke *et al.*,[73] Kubicki *et al.*,[74] Strandh *et al.*[75]
$Al(OH)_4^-$	Luke *et al.*,[73] Kubicki *et al.*,[74] Teppen *et al.*[76]
$Al(OH)_6^{3-}$	Bougeard *et al.*[77]
$Al(OH)_3(H_2O)_3$	Teppen *et al.*[76]
$Si(OH)_3$-O-$Si(OH)_3$	Kubicki *et al.*,[74] Strandh *et al.*[75]
$[Si(OH)_3$-O-$Al(OH)_3]^-$	Kubicki *et al.*,[74] Teppen *et al.*[76]
$Si(OH)_3$-O-$Al(OH)_2(H_2O)_3$	Teppen *et al.*[76]
$Al(OH)_2(H_2O)_2$-$(OH)_2$-$Al(OH)_2(H_2O)_2$	Teppen *et al.*,[76] Sainz-Diaz *et al.*[78]
$Mg(OH)_2(H_2O)_2$-$(OH)_2$-$Mg(OH)_2(H_2O)_2$	Sainz-Diaz *et al.*[78]

For example, Gorb *et al.* used $Si_6Al_6O_{30}H_{18}$ based clusters to determine geometrical parameters of the closely related clay minerals pyrophyllite and montmorillonite and reported good agreement with available experimental data.[85]

More recently, structural data has been reported from studies of periodic clay minerals models,[93–96] listed in Table 3.2. Periodic models are much better able to represent the extended layer structure of clay minerals and also do not suffer from edge-effects. It is interesting to note that all recent studies of periodic models of clay minerals have employed a density functional method in conjunction with pseudopotentials and a planewave basis set,[93–96] which indicates the aptness of the technique to the study of such systems. This is exemplified by Teppen *et al.*,[93] who used the method to calculate the structures of kaolinite, talc, pyrophyllite and nontronite, showing each to be in very good agreement with experiment.

In addition, the use of periodic models has enabled the study of hydrogen bonding between adjacent layers in kaolinite and dickite and its effect on the orientation of surface hydroxyl groups.[94,100] This is particularly useful, due to the difficulties associated with the determination of the position of hydrogen atoms by experiment.

Table 3.2: Structural Studies of Clay Minerals with Periodic Models

clay mineral	associated reference(s)
kaolinite	Teppen *et al.*,[93] Benco *et al.*[94]
dickite	Benco *et al.*[94]
talc	Teppen *et al.*,[93] Bridgeman *et al.*[95]
pyrophyllite	Teppen *et al.*,[93] Bridgeman *et al.*[95]
beidellite	Chatterjee *et al.*[96]
montmorillonite	Chatterjee *et al.*[96]
nontronite	Teppen *et al.*[93]

3.2 Isomorphic Substitution

In view of its relation to catalytic properties, several authors have investigated various aspects of isomorphic substitution in the course of their theoretical studies.

In an analytical study, Ebina *et al.* assessed the potential of X-ray photoelectron spectroscopy for determination of the distribution of aluminium in the tetrahedral and octahedral sheets of phyllosilicate clay minerals.[82] X-ray photoelectron spectra indicated Al(2p) binding energies of 74.5 eV for aluminium in octahedral sites and 73.3 eV for that in tetrahedral sites, a difference of 0.8 eV. The authors showed the distribution of aluminium in tetrahedral and octahedral sites to follow the ratio of the area of peaks fitted to these values. For comparison, Al(2p) binding energies were also calculated using density functional theory; these were 70.1 eV for aluminium in octahedral sites and 69.5 eV for that in tetrahedral sites. It was commented that although these reflect a marked difference in absolute values, their difference is in good agreement at 0.6 eV and validated the experimental procedure.

In other density functional studies of cluster models, Chatterjee *et al.* showed that in montmorillonite substitution of silicon in the tetrahedral layer by aluminium is an unfavourable process[79] and the preference for substitution of aluminium in the octahedral layer decreases as: $Fe^{3+} > Mg^{2+} > Fe^{2+} > Na^{+} > K^{+}$.[92]

3.3 Interlayer Cations and Water

The interaction of interlayer cations and water with the surface of clay minerals is responsible for many of their most important properties, such as swelling behaviour and catalysis. This has motivated many *ab initio* studies.

Density functional investigations of montmorillonite (octahedral substitution) and beidellite (tetrahedral substitution) by Chatterjee *et al.* showed that interlayer cations prefer to reside close to sites of isomorphic substitution.[87,96] The earlier of their two studies,[87] which used cluster models of the clay mineral, showed that cations associated with octahedral substitution sites in montmorillonite lie much closer to the surface of the clay mineral than those associated with tetrahedral substitution sites in beidellite. The authors however acknowledged the limits of cluster models and the need for periodic models in order to properly take into account the influence of both sides of the interlayer. These concerns were justified when their later study of periodic models of the same clay minerals,[96] indicated that in fact cations associated with tetrahedral substitution sites lie closer to the surface than those associated with octahedral substitution sites, the exact opposite relation.

In a related study Gorb *et al.* examined a clay mineral cluster model which exhibited isomorphic substitution in both the tetrahedral and octahedral layer.[84] MNDO-PM3 semiempirical calculations indicated that in such a system the favoured position for an interlayer cation is in the vicinity of the tetrahedral substitution site.

In addition to determination of their preferred location, several *ab initio* studies have also looked at the hydration of interlayer cations on the clay mineral surface. These showed that as the number of hydrating water molecules increases: the cation moves further away from the clay mineral surface;[75,84–86] the water molecules bind less tightly to the cation;[84–86] and the enthalpy gained from the addition of a new water molecule to the cluster decreases.[84–86] The non-additive nature of each of these phenomena is attributed to hydrogen bonding between water molecules and oxygen atoms on the clay mineral surface.[84]

The potential reactivity of water within the interlayer has also been of interest, especially in relation to acid catalysis. A study of the hydration of a magnesium cation at the clay mineral surface by Gorb *et al.*[84] showed that dissociation of a hydrating water molecule to form a Brønsted acid site is an endothermic process. In addition, the possible reaction of water molecules with hydroxyl groups in the octahedral layer of 2:1 clay minerals to form H_3O^+ has been investigated as part of several studies,[95,96] which showed high energy barriers prohibited such processes.

The roles of interlayer cations and water in the dissolution of clay minerals have also been examined using cluster models representative of surface and edge sites, at different pH values.[74,75] The effect of adsorption of alkali metal cations on the dissolution of silicate minerals was investigated by Strandh *et al.*[75] The authors showed that cations adsorbed onto the interlayer surface stabilise Si–O bonds at low pH, but weaken them at high pH. In addition, their calculations indicated that solvation of adsorbed cations reduces dissolution reaction energies, particularly with small cations. In an analogous study,[74] Kubicki *et al.* showed that, like adsorption of cations, hydrogen bonding to the interlayer surface also stabilises Si–O bonds at low pH, but weakens them at high pH.

3.4 Interaction with Organic Compounds

There is much interest in the interaction of organic molecules with clay minerals due to a desire to understand the complex chemical processes that occur in soil systems, in particular the mobility and biochemical degradation of herbicides, pesticides and other pollutants. Study of the adsorption of organic species on such surfaces is however very difficult by experimental methods, not least because of the problems with the characterisation of the clay minerals themselves. Therefore to obtain insight at the molecular level, *ab initio* simulations have been performed, which are able to provide information on the possible orientations of molecules in the interlayer, type and extent of bonding involved and relative adsorption and intercalation energies.

Several electronic structure studies have looked at the interaction of organic acids with clay minerals,[73,74,80,81,90,99] because they are often the final product of degradation processes and involved in the dissolution mechanism of clay minerals.

Early work by Luke *et al.* reported the first *ab initio* optimised structures of acetic acid and clay mineral fragments representative of exposed tetrahedral sites at the clay mineral edge.[73] This was followed by work by Kubicki *et al.* who studied the adsorption of water and acetic acid onto a range of cluster models intended to mimic interlayer and edge sites of aluminosilicate clay minerals.[74] The most likely surface complexes were determined from reaction energetics and comparison of calculated and experimental vibrational frequencies. In addition, the authors elucidated a mechanism which offered some insight into why organic acids increase dissolution rates and preferentially leach aluminium over silicon. In the suggested mechanism, as acetic acid approaches the clay mineral surface it forms a trigonal bipyramidal complex with an aluminium atom in the tetrahedral layer, which causes associated Al–O bonds to increase in length, while Si–O bonds remain largely unaffected.

More recently Tunega *et al.* examined the adsorption of water and acetic acid on the interlayer surface of kaolinite type clay minerals using both cluster and periodic model systems.[90,99] These studies showed pronounced differences in the adsorption of both molecules onto the two different surfaces presented by such clay minerals. Calculated adsorption energies indicated that both water and acetic acid interact much more strongly with the octahedral surface, which comprises surface hydroxyls, than the tetrahedral surface, which is made up of basal oxygen atoms. This was explained in terms of the number and nature of hydrogen bonds each molecule is able to make, which are higher and stronger, respectively, at the octahedral surface where hydroxyls act as both hydrogen bond donors and acceptors. Similar observations have been made for formamide, *N*-methyl-formamide and dimethylsulfoxide on the surface of kaolinite type clay minerals.[91]

There has also been some interest in the interaction of nitroaromatic compounds (NACs) with clay minerals, due to their widespread use as herbicides, pesticides

and solvents. Employing a range of *ab initio* methods Pelmenschikov *et al.* showed that complexation of NACs onto siloxane sites of clay minerals is mainly governed by dispersion interactions and not electron donor-acceptor interactions between the electron-deficient π-system of the NACs and siloxane oxygens, as at first thought.[89] In addition, work by Gorb *et al.* indicated that the interaction energy of NACs with partially hydrated clay mineral surfaces is similar to that observed with non-hydrated surfaces.[85]

The potential significance of clay minerals in the origin of life[102] has led to studies of the interaction of small peptides with the interlayer surface of clay minerals.[73,98] Yu *et al.* used a periodic system to investigate the adsorption of *N*-formyl-D-alanine amide (D-Ala) and *N*-formyl-L-alanine amide (L-Ala) on the interlayer surface of the clay mineral nontronite.[98] They showed that the two molecules adopt very different geometries with respect to the clay mineral layer—in the case of L-Ala, the C(α)-C(β) bond orientates perpendicular to the surface, while for D-Ala it is parallel. In both cases however, the optimised structures exhibit a continous chain of hydrogen-bond-linked peptide molecules, which implies that the clay mineral may act as template. Interestingly enough, although the L-Ala system was 6 kcal mol^{-1} more stable than the D-Ala system, the relative affinities were reversed when the enantiomeric form of the clay mineral was used. The authors suggested that this implies that participation of clay minerals in chemical evolution can only be hypothesised if the natural distribution of clay enantiomers is unequal or a bioprocess is started by a specific enantiomeric form of a clay mineral and then dominates the subsequent evolution.

Nontronite is of particular industrial importance due to its use as a catalyst in the reductive dechlorination of organic contaminants in groundwater aquifers. In view of this, Teppen *et al.* used *ab initio* molecular dynamics to examine the interaction of trichlorethane with the clay mineral.[93] The results of their simulations indicated that reductive dechlorination of trichloroethane on notronite occurs more readily in the presence of water.

3.5 Prediction of Vibrational Spectra

First principles techniques have been employed to calculate vibrational frequencies of various clay minerals, in order to facilitate interpretation of experimental spectra. The attraction of these methods is that they allow one to determine the vibrational frequencies of individual bonds and the relative shifts induced by variation of their local environment.

The traditional way to calculate vibrational spectra at the quantum level is to employ a second derivatives based method. Due to the great computational expense associated with this approach it has only been applied to small cluster models of clay minerals.[74,78,80,81,92] The use of cluster models introduces significant errors, since they are unable to account for hydrogen bonding between hydroxyl-hydrogens and apical oxygen atoms of the tetrahedral sheet. In particular, calculated hydroxyl stretching frequencies, are found to be lower than experimental values.[78] The main successes of these types of study have been to predict *relative* shifts in vibrational frequencies with respect to isomorphous substitution[78,92] and to aid interpretation of experimental vibrational spectra of organic acids adsorbed onto the surfaces of clay minerals.[80,81]

More recent investigations have taken another route and calculated vibrational spectra from the Fourier transformation of the velocity autocorrelation function (VACF) obtained from the trajectories of relatively short (1ps) *ab initio* molecular dynamics simulations of periodic models.[94,100,101] This technique is discussed in detail by Kleinhesselink and Wolfsberg who recommend the use of a long trajectory coupled with truncation of the VACF prior to its Fourier transform, in such a way that the tail of the VACF is disregarded.[103] Benco *et al.* employed this method to interpret the stretching frequencies of the structural hydroxyl groups of kaolinite and dickite, whose experimental spectra are particularly difficult to resolve due to complex inter- and intra-layer hydrogen-bonding.[94,100,101] This led to proposal of a new interpretation of the observed hydroxyl stretching frequencies of dickite.[100]

Common to several studies has been the observation of an approximately linear relationship between calculated hydroxyl stretching frequency and O-H and O-H..O bond lengths.[78,94,100,101] This implies that careful examination of optimised models may offer useful information on relative hydroxyl vibrational frequencies without the need for their explicit calculation.

3.6 Force-Field Development

A lack of available experimental data has meant there has been a much greater dependency on *ab initio* calculations in the development of interatomic potentials for clay mineral systems, than most other types of system.

In view of their related structures, force-fields for clay minerals have tended to be developed by adaption and extension of those originally designed for silica and zeolites systems. For example, in their development of a force-field, Teppen *et al.* performed a large number of first principle calculations on an array of cluster models representative of the common structural features of aluminosilicate clay minerals.[76] The results of these calculations were then used in combination with parameters taken directly or adapted from a force-field developed for silica and zeolites[104,105] by Hill and Sauer, to produce a new force-field for dioctahedral aluminosilicate clay minerals.[106] Teppen *et al.* later reported work in which this force-field was successfully employed in classical molecular dynamics studies of proteins on the surface of the clay mineral pyrophyllite.[107]

In a similar manner, Bougeard *et al.* performed electronic structure calculations to develop force-field parameters for octahedrally coordinated aluminium, to add to those from their previous work on zeolites[108,109] and produce a new force-field suitable for clay minerals.[77] Classical molecular dynamics simulations performed on the clay mineral kaolinite, reported in the same paper, showed the new force-field yielded structural parameters and vibrational spectra in good agreement with experimental data.

3.7 Summary

The application of *ab initio* simulation methods to clay minerals is very worthwhile, since they yield information unavailable from experimental data. It is possible to determine accurate crystal structures, study the effect of isomorphous substitution, investigate their interaction with water and small organic molecules and determine vibrational frequencies. Such information enhances understanding of the chemical behaviour of clay minerals and should ultimately lead to increased control over their physical and chemical properties.

Chapter 4

Montmorillonite: A Solid Acid Catalyst

The general structure and properties of clay-polymer nanocomposites were briefly mentioned in Section 1.3.5. They offer enhanced mechanical,[23,24] thermal[25,26] and permeability properties,[27] which has led to a wide range of applications in the automotive, electronics and furnishing industries. The favourable qualities of these hybrid materials has motivated much research into their synthesis.

Three established methods of clay-polymer nanocomposite preparation exist: exfoliation-adsorption,[110] *in situ* intercalative polymerisation,[23,111,112] and polymer melt intercalation.[24,113,114] Exfoliation-adsorption involves initial exfoliation of the clay mineral using a solvent in which the polymer is soluble, followed by addition of the polymer, which is adsorbed onto the clay mineral layers. Upon evaporation of the solvent the clay mineral layers reassemble. The major disadvantage of this approach is that a suitable solvent is not always available. *In situ* intercalative polymerisation involves mechanical mixing of the clay mineral with a monomer, which intercalates within the interlayer and promotes delamination. This is followed by polymerisation of the monomer to yield linear or cross-linked polymer matrices. Polymerisation may be initiated by heat, radiation, an organic initiator or a catalyst, such as an acid, fixed through cationic exchange inside the interlayer. However, it is often necessary to disperse the clay mineral by a pre-swelling step of long-chain alkylammonium ion

intercalation to aid exfoliation. This is brought about by exchange of the natural interlayer cations with the organic salt. It is convenient to combine the pre-swelling of the clay mineral with its acid treatment. Polymer melt intercalation simply involves mechanical mixing of the clay mineral into a polymer melt. Similar to *in situ* intercalative polymerisation, polymer melt intercalation usually necessitates some pre-treatment of the clay mineral, again via exchange of the natural cations with an organic salt. In this case however, the purpose of the treatment is not to aid delamination of the clay mineral, but rather the presence of the alkylammonium cations within the interlayer renders the hydrophilic clay mineral layers organophilic and therefore increases the enthalpic interactions with the intercalating polymer.

For a comprehensive review of standard preparation methods, properties and uses of clay-polymer nanocomposites the reader is directed to Alexandre and Dubois.[115] Here however, we consider a new synthetic route that has recently been proposed by Coveney *et al.*,[116] known as 'self-catalysed *in situ* intercalative polymerisation'. The method is similar to *in situ* intercalative polymerisation, but does not require any pre-treatment of the clay mineral—two monomers are intercalated, which are thought to spontaneously copolymerise. It is worthy of particular attention, since it requires no pre-treatment of the clay mineral and also occurs under facile conditions. The polymerisation mechanism is however poorly understood; in particular it is unclear how the reactions are catalysed by the untreated clay mineral.

The purpose of the present study is to provide theoretical insight into the role of the clay mineral in self-catalysed *in situ* intercalative polymerisation. In particular, we examine the reaction of methanal with ethylenediamine, within the interlayer of Wyoming montmorillonite. More specifically, we investigate the potential of the clay mineral to render the carbonyl bond of methanal open towards nucleophilic attack; either by protonation from a Brønsted acid source or its coordination to a Lewis acid site. We also examine the subsequent nucleophilic attack of ethylenediamine on an activated methanal molecule. This is done using density functional theory based calculations on periodic models of the clay system.

This chapter is organised as follows. In Section 4.1 relevant experimental data is analysed and a possible reaction mechanism is postulated. The potential sources of Brønsted and Lewis acidity in Wyoming montmorillonite are discussed in Section 4.2. This is followed by an account of the model systems and the optimisation method used in Section 4.3. The results of the simulations are elaborated in Section 4.4. Finally, in Section 4.5, we draw some conclusions.

4.1 Intercalative Polymerisation

The synthesis of clay-polymer nanocomposite materials by self-catalysed *in situ* intercalative polymerisation was first reported by Coveney *et al.*,[116] who treated thin films of the clay mineral Wyoming montmorillonite with different combinations of monomers. X-ray diffraction (XRD), fast-atom bombardment mass spectrometry (FAB MS) and solid-state nuclear magnetic resonance (NMR) spectroscopy were used to ascertain whether or not any form of polymerisation had occurred.

One pair of monomers used by Coveney *et al.*[116] was methanal (CH_2O) and ethylenediamine ($NH_2CH_2CH_2NH_2$), which in addition to being cheap, formed a particularly desirable nanocomposite material—non-exfoliated, flexible and hard. XRD analysis of the sample indicated an average interlayer separation of 14.4 Å, which was unaffected by subsequent extraction with chloroform. FAB MS of the filtrate offered evidence for polymer formation on the clay and, thus, presumably inside also. Molecular ions of mass/charge 90, 120, and 150 were attributed to hemiaminals formed by the addition of one, two and three molecules of methanal to ethylenediamine. Higher molecular ions with mass/charge 424, 443, and 613 indicated copolymerisation, but could not be assigned to specific addition products. Magic angle spinning ^{13}C NMR performed on an analogous laponite nanocomposite however, provided evidence for the presence of hemiaminal, aminal and methylene carbon atoms, implying that copolymerisation had indeed occurred. In view of this, it was chosen as a case study to examine the catalytic properties of the clay mineral.

The synthesis of Nylon 66 from hexanedioic acid and 1,6-hexanediamine is one of the most well known examples of copolymerisation.[117] The reaction is acid-catalysed and begins with the protonation of a carbonyl group of the acid, rendering it open to nucleophilic attack by a nitrogen of the amine. The addition of the amine to the acid is followed by elimination of both water and the initial acid catalyst. Methanal and ethylenediamine possess similar functional groups to those of hexanedioic acid and 1,6-hexanediamine and it was postulated that they may undergo a similar type of reaction within the interlayer of Wyoming montmorillonite, as shown in Figure 4.1: equations 1 and 2. Protonation of methanal is followed by nucleophilic attack by ethylenediamine leading to an initial hemiaminal addition product. The subsequent stages lead to the formation of an aminal, itself able to perform nucleophilic attack on a second methanal molecule and thus copolymerisation may proceed. In the synthesis of Nylon 66, one of the monomers is an acid which autocatalyses the reaction, albeit very slowly, unless the reaction mixture is heated or an additional acid source is introduced. However, neither methanal nor ethylenediamine is an acid. It is therefore reasonable to assume that the copolymerisation reaction between methanal and ethylenediamine is catalysed by the clay mineral acting in some way as a solid acid.

It is worth noting that magic angle spinning ^{13}C NMR also displayed peaks characteristic of poly-acetal carbon atoms, indicating some self-polymerisation of methanal had taken place,[116] as seen in Figure 4.1, equation 3. This made it difficult to conclusively assign the larger ion fragments indicated by FAB MS to a methanal-ethylenediamine copolymer since they may also be due to paraformaldehdye.

In both reactions however, the initial stages are likely to be the same, that is, the protonation of methanal (Figure 4.1, equation 1). It is thus very important to understand the role of Wyoming montmorillonite as a solid acid catalysts, in order to determine the likely mechanism of nanocomposite formation.

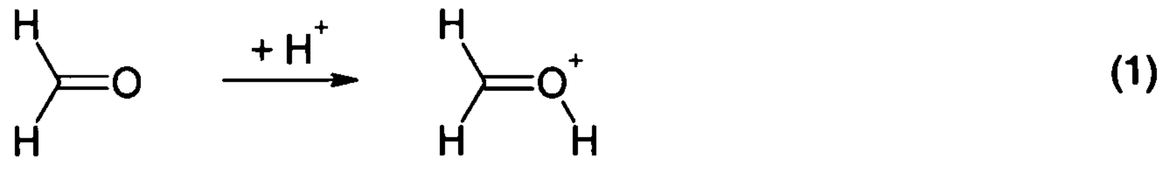

Figure 4.1: Postulated polymerisation mechanisms; (1) protonation of methanal; (2) copolymerisation of methanal with ethylenediamine; and (3) self-polymerisation of methanal.

4.2 Wyoming Montmorillonite

Montmorillonite is a *cis*-vacant, 2:1 layer type, clay mineral characterised by partial substitution of aluminium by magnesium in the octahedral layer, typically balanced by sodium and calcium interlayer cations. This leads to a general unit cell formula $Na_nCa_{(x-n)/2}[Mg_xAl_{4-x}(OH)_4Si_8O_{20}]$.

In fact, most montmorillonites show small amounts of other types of substitution; the most prevalent being that of aluminium by iron(III) in the octahedral layer. In the Wyoming montmorillonite, used by Coveney *et al.*,[116] a small fraction of aluminium for silicon substitution is also present in the tetrahedral layer. This leads to a general unit cell formula $Na_nCa_{(x+z-n)/2}[Mg_xFe_yAl_{(4-x-y)}(OH)_4Al_zSi_{(8-z)}O_{20}]$. Typical values are $n = 0.32$, $x = 0.54$, $y = 0.40$ and $z = 0.02$.[118]

In this thesis we adopt the nomenclature according to which montmorillonite that exhibits substitution only in the octahedral layer will be referred to as 'Texas-type' and that with substitution in both tetrahedral and octahedral layers will be called 'Wyoming-type'.

Brønsted Acidity

When considering the structure of montmorillonite, the most immediately obvious source of Brønsted acidity is the hydroxyl groups that bridge two aluminium atoms in the octahedral layer. These protrude into the interlayer through the hexagonal silicate structure of the tetrahedral layer.

A second possible source arises from protons attached to oxygen atoms in the tetrahedral layer, which act as counterions to the negative charge created either by magnesium-for-aluminium substitution in the octahedral layer or aluminium-for-silicon substitution in the tetrahedral layer.[5,119] These are similar to Brønsted acid sites found in Y-zeolites and are more accessible than the aforementioned protons.

A third potential source exists at lattice edges where the sheet structure is broken and bonds are terminated by hydroxyl groups which may act as Brønsted acid sites.[7]

Experimental work has suggested that peptide formation may be initiated by such silanol (Si–OH) and aluminol (Al–OH) groups.[120,121]

However, the most important source of Brønsted acidity is widely believed to be dissociated water molecules in the hydration sphere of the interlayer cations.[122–125] This acidity depends upon the water content of the clay and, to a lesser extent, upon whether the layer charge arises mainly from isomorphic substitution in the octahedral or tetrahedral layer. It is maximised when the water content of the clay is low and when highly polarising species such as M^{3+} cations are exchanged for the naturally occurring Na^{+} and Ca^{2+} cations.[124,125]

The first two sources of Brønsted acidity listed above are thought to be minor contributors to the total acidity since the hydrogens are tightly bound,[5,126] and thus the latter two sources are likely to be the most prolific. The former sources may become more important at high temperatures or under anhydrous conditions when exchangeable cation acidity becomes very low.[5,127] (Most of the copolymerisation reactions reported by Coveney *et al.* were performed at room temperature.[116])

Lewis Acidity

Lewis acidity is associated with exposed aluminium ions at the clay mineral edge.[5,128] Commenting on experimental studies by Solomon and Rosser into polymerisation of styrene, Grim alleged that the greater catalytic activity shown by attapulgite, as compared with other clay minerals, implies that crystal edges are involved in catalysis; attapulgite has a much larger edge-to-surface-area ratio owing to its unusual structure.[3] Grim therefore suggested that the catalytic activity was related to aluminium in octahedral coordination situated at the crystal edges.

This view is further supported by investigations of Kubicki *et al.*, who employed attenuated total reflectance Fourier transform infrared spectroscopy and Hartree-Fock calculations, to determine the nature of chemical bonding between salicylic acid and the clay mineral illite.[81] The correlation of experimental and calculated

vibrational frequencies indicated complexes involving carboxylate oxygen atoms bonded to aluminium in octahedral coordination exposed at the lattice-edge. In addition, by using selective blocking Negrón-Mendoza *et al.* showed that it is the Lewis acid sites of Wyoming montmorillonite that cause decarboxylation of alpha-ketoglutaric acid.[129]

4.3 Simulation Details

In this section we describe the development of the model systems and optimisation method used. We also give some technical details concerning the calculations.

4.3.1 Clay Mineral Model Systems

Since montmorillonite is naturally disordered in the planes of the clay layers, little structural data is available in the common international X-ray crystallographic databases, where only the unit cell parameters are found.[130] It has therefore been customary to construct models of montmorillonite from the crystal structure of a closely related clay mineral. This however, has led to many studies of the wrong structural isomer. Nearly all previous simulation studies of montmorillonite have examined the *trans*-vacant isomer, since they used models based on the crystal structure of a *trans*-vacant clay mineral. Experimental evidence suggests however, that the naturally occurring material is of the *cis*-vacant form.[131,132]

In classical molecular dynamics simulations where interest is focused on events occurring in the interlayer, the choice of isomer can be expected to have negligible effect on computed properties, but when the behaviour of the hydroxyl groups are being studied, it may play a crucial role. Sainz-Diaz *et al.* examined the *cis* and *trans*-vacant configurations of illites and smectites using interatomic potentials.[133] These authors found that though there was little difference in hydroxyl bond length for the two isomers, the angle that the hydroxyl groups made with the *ab* plane was slightly higher in the *cis*-vacant clays minerals, as compared to the *trans*-vacant.

In view of this, a periodic model of *trans*-vacant pyrophyllite was created from one of *trans*-vacant muscovite (disregarding hydrogen atomic positions) from a structural database.[134] Pyrophyllite possesses identical layers to muscovite, but exhibits no isomorphic substitution in either the tetrahedral or octahedral layer. This model, formula $[Al_2(OH)_2Si_4O_{10}]_2$, was assigned the unit cell parameters for montmorillonite listed in the crystallographic database[130] and optimised as outlined in Section 4.3.3, with no atom or cell constraints imposed. The resultant model was transformed into a *cis*-vacant pyrophyllite model and optimised in a similar manner.

The optimised *cis*-vacant pyrophyllite model was then used as a template for the fabrication of three Texas-type and six Wyoming-type montmorillonite models. Each Texas-type montmorillonite systems was given one magnesium-for-aluminium substitution in the octahedral layer and a proton counterion, attached to a basal oxygen atom in the tetrahedral layer; unit cell formula $[MgAl_3(OH)_4(Si_4O_{10})_2H]$. Two Wyoming-type montmorillonite systems were created from each Texas-type system by introduction of aluminium for silicon substitution in the tetrahedral layer. In order to keep the Wyoming-type systems simple, no additional counterion was inserted to balance the extra isomorphic substitution. This gave each model a unit cell formula $[MgAl_3(OH)_4(AlSi_7O_{20})H]^-$.

The crystallographic database listed a very small montmorillonite unit cell c parameter of 9.07 Å, which corresponds to a low interlayer separation. (The unit cell c parameter regulates the magnitude of the interlayer separation.) This low value is typical of a dehydrated clay sample; at this value no organic molecules could be accommodated between the clay layers. Since it was intended to explore the potential of the Brønsted acid sites within the interlayer to protonate methanal and ethylenediamine, it was necessary to calculate a suitable unit cell c parameter corresponding to a d-spacing large enough to accommodate the monomers.

Preliminary investigations showed that for the clay-monomer model systems, the initial alignment of monomers with respect to a hydroxyl group located in the tetrahedral layer greatly affected their potential for protonation during optimisation.

Protonation was found to occur most readily in the following situations: (i) the angle between the oxygen atom in the tetrahedral layer, the proton and the acceptor atom of the monomer was approximately 180°; (ii) in the case of methanal, the angle between the proton, the oxygen acceptor atom and the carbon atom was approximately 120°; (iii) in the case of ethylenediamine, the angles between the proton, the nitrogen acceptor atom and the other atoms bonded to the nitrogen were all approximately 109°. The total energy of the clay-monomer systems were also lowest when such geometries were adopted. These observations are understandable in terms of the preferred geometry of the protonated species. It was thus assumed that protonation would be most probable when the interlayer separation was large enough to allow the monomers to align as defined above. Further investigations involving the optimisation of relevant clay-monomer model systems over a range of interlayer separations showed that a *d*-spacing corresponding to a unit cell *c* parameter of approximately 13 Å was appropriate. This value was thus applied to all clay mineral models, which were then optimised with no constraints imposed.

Periodic models of pyrophyllite and Texas-type montmorillonite that exhibited a lattice-edge were created from the optimised pyrophyllite model. This was done by breaking all bonds crossing the periodic plane made by the **b** and **c** lattice vectors. Oxygen atoms were then terminated with a hydrogen atom and non-oxygen atoms with a hydroxyl group, To accommodate the extra atoms and to allow room for the insertion of monomers at the lattice-edge it was necessary to increase the unit cell *b* parameter to 17.5 Å. These models were then optimised with no atom or cell constraints imposed.

4.3.2 Interaction of Monomers with Acid Sites

Throughout the polymerisation reaction between methanal and ethylenediamine an unknown mixture of cations, water and monomers/polymer may be present within the interlayer holding the clay layers apart. The complexity of the potential energy

surface that would result from trying to model each of these species, and the small size of the system cell, meant that it was decided to model only those interactions between the clay mineral surface and the monomers. The absence of water is justified to a certain extent by the fact that organic molecules, driven by entropic factors, are usually absorbed into the interlayer with the expulsion of water.[135]

Molecular models of methanal and ethylenediamine molecules were constructed and their geometries optimised using semiempirical methods; in particular, AM1 for methanal and MINDO3 for ethylenediamine, based on reported recommendations.[136] These were inserted into the periodic clay mineral models and aligned in such a way as to make protonation favourable, as described in the previous section, with a distance of approximately 1.00 Å between the proton and potential acceptor atom. In the case of Lewis acid sites the monomers were co-ordinated to the metal atoms, at a distance of approximately 2.00 Å. In this way model systems were created with each monomer interacting with each of the different types of acid site.

In addition, model systems were also constructed to investigate the interaction between methanal, ethylenediamine, water and interlayer cations. These possessed no representation of the clay mineral.

4.3.3 Geometry Optimisation

Geometry optimisation calculations were carried out using the density functional theory based CASTEP code,[137] which utilises periodic boundary conditions, a plane-wave basis set and **k**-point sampling. Teppen *et al.* previously used this code to optimise the structures of the clay minerals talc, kaolinite and pyrophyllite and reported very good agreement with experimental results.[93] In view of this, an almost identical setup was used. Ultrasoft pseudopotentials were employed.[42] The energy cut-off for the planewave expansion was set at 340eV and just one special **k**-point was allowed in the Brillouin zone. For all simulations the gradient-corrected PW91 exchange-correlation functional was used.[61,62]

In order to allow calculation of total energy differences between unit cells of different volume, at a relatively low kinetic energy cut-off, a finite basis set correction was applied.[138] This corrects total energies for errors due to the use of a finite **k**-point set in a finite cut-off energy calculation.

Different constraints were applied to the various clay-monomer systems during their optimisation. In all optimisations one aluminium atom in the octahedral layer was fixed. In the case of the small periodic models all cell parameters were allowed to vary. For the lattice-edge models all cell parameters were allowed to vary apart for the b and c parameters. For the larger models, used to investigate the effect of degree of substitution, all cell parameters were fixed.

4.3.4 Computational Details

The smaller calculations were run serially on a Silicon Graphics Octane workstation mounted with two 225 MHz MIPS R10000 processors and 1GB RAM. The larger calculations were run in parallel on a Silicon Graphics Onyx2 mounted with sixteen 400MHz MIPS R12000 processors and 8GB RAM. The code scaled well for our simulations. For example, geometry optimisation of a montmorillonite unit cell containing a single methanal molecule experienced a speed-up of 1.68, 3.70, 7.30 and 13.33 when using 2, 4, 8 and 16 processors, respectively. Here speed-up is defined as the ratio of the time required for the single-CPU execution to the time required for execution on N processors.

4.4 Results and Discussion

In this section we present and discuss the most important results of the simulations. We begin with observations on the interaction of ethylenediamine with methanal and Brønsted acidity of water molecules in the hydration sphere of interlayer cations. This is followed by a description of the optimised clay mineral structures and the interaction of methanal and ethylenediamine with their various acid sites.

Table 4.1: Selected Bond Lengths of Optimised Cation-Monomer Models/Å

	M–O=CH_2		M–O–$CH_2NH_2CH_2CH_2NH_2$		
M	M–O	O=C	M–O	O–C	C–N
H^+	0.9928	1.2489	0.9742	1.3721	1.5401
Na^+	2.1765	1.2190	2.0706	1.3071	1.5917
Ca^{2+}	2.1018	1.2411	1.9486	1.3746	1.4989

4.4.1 Reaction of Methanal with Ethylenediamine

Optimisations showed the nucleophilic attack of ethylenediamine on methanal to occur only when the carbonyl bond was activated by protonation or coordination to a metal cation. In such cases the carbonyl bond length increased from 1.2086 Å, the value calculated for an isolated methanal molecule, to those listed in Table 4.1, column three. The increase in bond length induced by a sodium cation is smaller than that of a proton or calcium cation. This is related to cation size and charge—smaller cations with higher charge are better able to polarise the carbonyl bond. The influence of co-ordinating cation is also noticeable in the oxygen-carbon and carbon-nitrogen bond lengths of the addition products, shown in Table 4.1.

These results could cause one to speculate that the copolymerisation reaction of methanal with ethylenediamine may be initiated by the interlayer cations of Wyoming montmorillonite, without the clay mineral structure itself playing a role. Though this mechanism cannot be dismissed, we believe it unlikely. The reactions were modelled in the absence of any representation of the clay mineral, interlayer water or additional monomers. It is known that at low water content, cations tend to associate with the negatively charged clay mineral layers, while at higher water content they are hydrated. Thus coordination of methanal is inhibited. In addition, association of several monomers, including ethylenediamine, with a single cation, would reduce its polarising effect on individual co-ordinated methanal molecules.

4.4.2 Brønsted Acidity of Hydration Sphere Water

The dissociation of water molecules in the hydration sphere of interlayer cations is considered by many to be the source of Brønsted acidity in clay minerals. It is however dependent on the cation type and degree of hydration. Investigations by Marshall *et al.*[123] into the hydration of lithium hydroxide showed that the Brønsted acidity of a $Li(H_2O)_n^+$ complex is strongest when $n = 1$. The authors stated that acidity is controlled by the effective charge on the cation; stabilisation of this charge by hydrating water molecules causes reduced acidity at higher coordination numbers.

In view of this, it was decided to model the possible protonation of monomers via the dissociation of a single water molecule co-ordinated to an interlayer cation. Three model systems were constructed for each cation studied. These comprised the cation hydrated by a lone water molecule, which was aligned so as to protonate either a second water molecule, a methanal molecule or an ethylenediamine molecule. Figure 4.2 shows an example of a cation-water-monomer model; in this case the interlayer cation is sodium and the monomer methanal.

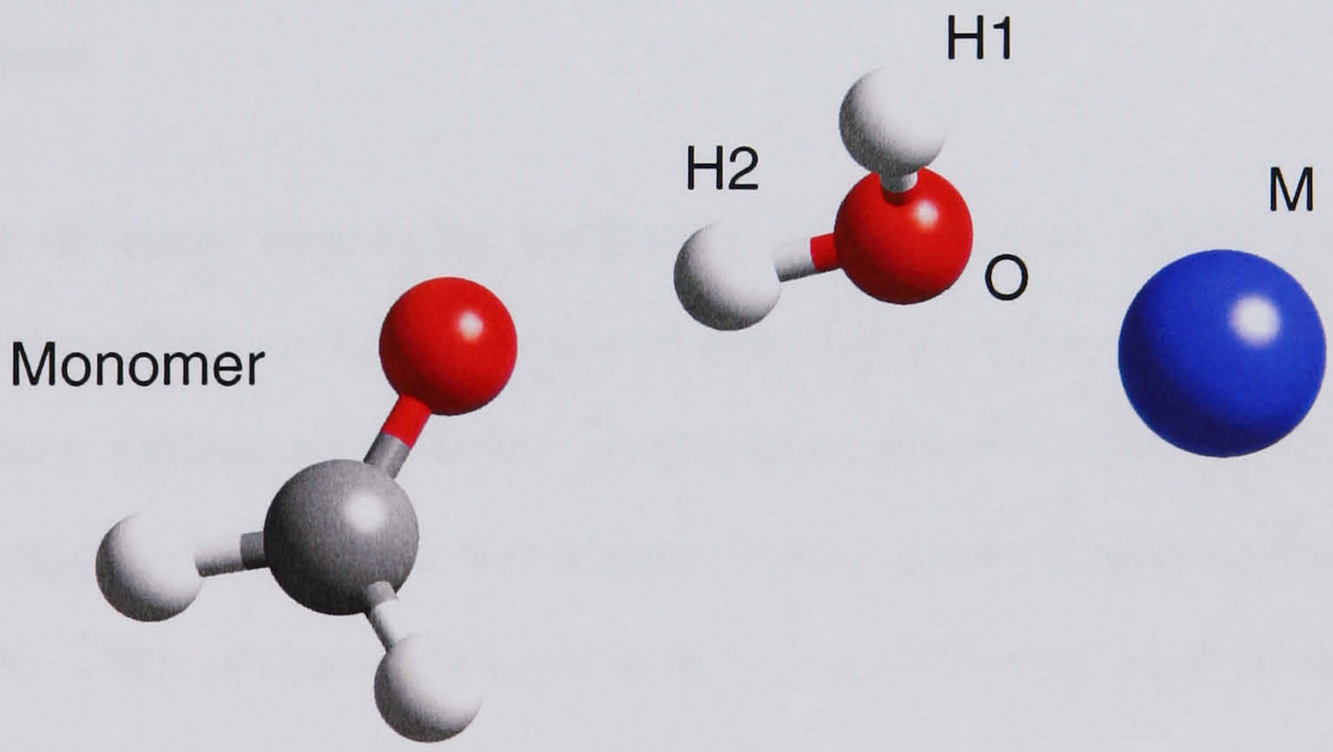

Figure 4.2: Example of a cation-water-monomer model system. The sodium cation is hydrated by one water molecule that is aligned to procure protonation of methanal. The colour scheme here is white for hydrogen, grey for carbon, red for oxygen, and blue for sodium. Labels define bonds referred to in Table 4.2.

Table 4.2: Selected Bond Lengths of Optimised Cation-Water-Monomer Models[a]/Å

metal cation (M)	monomer	M–O	O–H1	O–H2[b]
Na^+	H_2O	2.1517	0.9703	1.0028
	CH_2O	2.1516	0.9713	1.0045
	$NH_2CH_2CH_2NH_2$	2.1418	0.9709	1.0491
Ca^{2+}	H_2O	2.0657	0.9760	1.1508
	CH_2O	2.0427	0.9779	1.2264
	$NH_2CH_2CH_2NH_2$	1.9800	0.9739	-
Mg^{2+}	H_2O	1.8194	0.9753	-
	CH_2O	1.8251	0.9740	-
	$NH_2CH_2CH_2NH_2$	1.8164	0.9745	-
Al^{3+}	H_2O	1.5731	0.9923	-
	CH_2O	1.5877	0.9902	-
	$NH_2CH_2CH_2NH_2$	1.6410	0.9822	-

[a] Bond labels refer to Figure 4.2.

[b] '-' = bond dissociated.

The number of water molecules hydrating an interlayer cation varies depending on the relative humidity—a figure of about five water molecules has been calculated for sodium cations within a hydrated montmorillonite.[139] The models are therefore a rather drastic approximation to the actual environment found within the interlayer of a clay mineral. They are nevertheless able to provide some insight into the possible protonation of monomers by dissociated water.

The cations examined were Na^+, Ca^{2+}, Mg^{2+} and Al^{3+}, the model systems of which were optimised with the appropriate net charge. Table 4.2 lists selected bond lengths of the optimised cation-water-monomer model systems. Labels refer to Figure 4.2. Note that where protonation of a monomer occurred only one hydroxyl bond length is listed.

The results show the expected effect of cation charge density—smaller cations with higher charge are better able to polarise a water molecule, causing dissociation. The charge density of the cations increases as one goes down Table 4.2. It can be seen that a water molecule associated with a sodium cation is not Brønsted acidic enough to protonate any of the monomers, while one co-ordinated to a calcium cation will protonate ethylenediamine, the most basic monomer, but not water or methanal. On the other hand, a water molecule associated with a magnesium or aluminium cation will protonate all the monomers.

In the interlayer of a clay mineral cations may be hydrated by several water molecules or associated with the negative silicate layers. This reduces their ability to polarise associated water molecules and induce dissociation. In the models each cation is hydrated by just one water molecule *in vacuo*, which represent the most favourable conditions for dissociation. One could therefore assert that water in the hydration sphere of sodium and calcium cations within the interlayer of Wyoming montmorillonite is not Brønsted acidic enough to protonate methanal and catalyse its copolymerisation with ethylendiamine.

4.4.3 Optimised Clay Mineral Models

In this subsection the optimised clay mineral unit cells are described, with special attention given to the hydroxyl groups.

Clay Mineral Unit Cells

Figure 4.3 illustrates the optimised pyrophyllite unit cell, viewed directly onto the *bc* plane. The composition of the nine montmorillonite unit cells are described with reference to this in Table 4.3. The location of the proton counterion, in the tetrahedral layer, is indicated by the oxygen with which it forms a hydroxyl group. The Texas-type montmorillonite unit cells model the proton counterion at various distances from a magnesium-for-aluminium substitution in the octahedral layer. The Wyoming-type montmorillonite unit cells also exhibit an aluminium-for-silicon

Figure 4.3: Optimised pyrophyllite unit cell. The colour scheme here is white for hydrogen, red for oxygen, pink for aluminium and yellow for silicon. Periodic boundaries are indicated by the blue dashed lines. The atoms are labelled according to their element type and number.

Table 4.3: Optimised Montmorillonite Unit Cells

clay model	octahedral substitution	tetrahedral substitution	location of hydroxyl groups
Texas-type 1	Al4 ⇒ Mg	-	O24
Texas-type 2	Al4 ⇒ Mg	-	O21
Texas-type 3	Al4 ⇒ Mg	-	O20
Wyoming-type 1	Al4 ⇒ Mg	Si8 ⇒ Al	O24
Wyoming-type 2	Al4 ⇒ Mg	Si8 ⇒ Al	O21
Wyoming-type 3	Al4 ⇒ Mg	Si8 ⇒ Al	O20
Wyoming-type 4	Al4 ⇒ Mg	Si6 ⇒ Al	O24
Wyoming-type 5	Al4 ⇒ Mg	Si6 ⇒ Al	O21
Wyoming-type 6	Al4 ⇒ Mg	Si6 ⇒ Al	O20

Table 4.4: Unit Cell Parameters of Optimised Clay Mineral Models; Lengths are in Å and Angles in °

clay model	a	b	c^*	α^*	β^*	γ
experiment[130]	5.18	8.96	9.97	90.0	99.9	90.0
pyrophyllite	5.16	8.95	13.14	89.1	97.2	90.1
Texas-type 1	5.19	9.02	13.24	90.2	97.0	89.9
Texas-type 2	5.19	9.05	13.45	90.8	96.3	89.8
Texas-type 3	5.18	9.05	13.33	90.6	96.6	89.8
Wyoming-type 1	5.19	9.02	13.24	90.2	97.0	89.9
Wyoming-type 2	5.22	9.11	14.10	90.5	96.3	89.4
Wyoming-type 3	5.23	9.16	13.55	90.3	96.2	89.6
Wyoming-type 4	5.23	9.08	13.26	90.7	97.0	89.9
Wyoming-type 5	5.24	9.05	13.92	90.6	96.1	90.0
Wyoming-type 6	5.20	9.11	13.37	90.8	96.6	90.1

* To aid subsequent insertion of the monomers each model was assigned an initial unit cell c parameter of 13 Å —leading to a two-dimensional model—hence the unit cell c, α and β parameters are not physically meaningful.

substitution in the tetrahedral layer; in the first instance, close to, and in the second, away from, the magnesium-for-aluminium substitution in the octahedral layer.

The unit cell parameters of the optimised clay mineral models are presented in Table 4.4, with experimental values for montmorillonite also listed for comparison. In general, calculated values are in good agreement with experiment, in particular those of the Texas-type montmorillonite models. This is as expected, since they most reflect the degree and type of substitution found in natural montmorillonites. *i.e.*, a low degree of magnesium-for-aluminium substitution in the octahedral layer. It is difficult to make meaningful correlations between unit cell parameters and type of substitution, since the models are very similar. The most noticeable effect is the increase in b upon introduction of a magnesium-for-aluminium substitution in the octahedral layer. No experimental data was available to compare atomic positions.

Table 4.5: O–H Bond Lengths of Optimised Clay Mineral Models[a]/Å

clay model	O1–H1	O4–H2	O9–H3	O12–H4	ON–H5[b]
pyrophyllite	0.9703	0.9697	0.9709	0.9693	-
Texas-type 1	0.9712	0.9679	0.9755	0.9721	0.9834
Texas-type 2	0.9729	0.9682	0.9758	0.9727	0.9808
Texas-type 3	0.9721	0.9679	0.9743	0.9723	0.9796
Wyoming-type 1	0.9724	0.9689	0.9733	0.9711	0.9786
Wyoming-type 2	0.9731	0.9650	0.9750	0.9720	0.9785
Wyoming-type 3	0.9724	0.9690	0.9725	0.9724	0.9761
Wyoming-type 4	0.9707	0.9710	0.9738	0.9710	0.9830
Wyoming-type 5	0.9705	0.9699	0.9746	0.9732	0.9754
Wyoming-type 6	0.9709	0.9719	0.9730	0.9729	0.9764

[a] Bond labels refer to Figure 4.3.

[b] For N refer to "location of proton counterion" Table 4.3.

Table 4.6: *ab*–O–H Angles of Optimised Clay Mineral Models[a]/°

clay model	O1–H1	O4–H2	O9–H3	O12–H4	ON–H5[b]
pyrophyllite	-25.8333	+21.8392	-34.4104	+32.9463	-
Texas-type 1	-23.0068	-16.2501	0.0000	+4.6743	+54.3614
Texas-type 2	-18.9487	-13.7364	0.0000	0.0000	+77.8514
Texas-type 3	-20.8296	-12.9369	+4.8069	0.0000	+86.5185
Wyoming-type 1	-10.6276	-9.0752	+5.4510	+8.6420	+38.6318
Wyoming-type 2	-10.2038	-8.5962	+4.8615	+10.4743	+36.3706
Wyoming-type 3	-13.1353	-8.2817	+13.5359	+7.2501	+83.4624
Wyoming-type 4	-21.2192	-15.9498	+6.0686	+13.3799	+55.3490
Wyoming-type 5	-18.5123	-8.6680	+6.0352	+7.8320	+58.0117
Wyoming-type 6	-21.5227	-11.7703	+13.3040	+8.6460	+75.5543

[a] Bond labels refer to Figure 4.3.

[b] For N refer to "location of proton counterion" Table 4.3.

Tables 4.5 and 4.6 respectively list the bond length and angle made with the *ab* plane of each hydroxyl in the optimised clay mineral models. The length of a hydroxyl bond gives an indication of Brønsted acidity, while its orientation gives an indication of accessibility to potential acceptor molecules. The values show that both hydroxyl bond length and angle are influenced by local isomorphic substitution, although, again, the small size and similarity of the models make it difficult to infer meaningful correlations. Nevertheless when considered with the bond length and angles of the hydroxyl groups in the larger montmorillonite models presented in Table 4.8, Section 4.4.3, some relations are apparent.

It can be seen in Table 4.5 that almost all montmorillonite models show the same variation in hydroxyl bond length—hydroxyl O9–H3 is longest, while O4–H2 is almost always shortest. The same variation is not seen in the pyrophyllite model, where all hydroxyls are more or less equal in length, which implies that it is effected by the magnesium-for-aluminium substitution in the octahedral layer. The precise nature of this interference is more clear in the bond lengths of the hydroxyl groups in the larger montmorillonite models, listed in Table 4.8. Those hydroxyls that are bonded directly to the magnesium substitution (OH13, OH14) are shorter in length, as compared to the average value, while the next nearest (OH12, OH15) are longer. Further away a consistent average value is reached.

The influence of magnesium-for-aluminium substitution in the octahedral layer on the length of hydroxyl groups in the tetrahedral layer is not very clear. In the small models bond length increases with proximity to the substitution, seen in Table 4.5. In the large models, it appears to have little effect, seen in Table 4.9.

Quite unexpectedly, no clear relationship between hydroxyl bond length and aluminium-for-silicon substitution could be inferred.

The calculated bond lengths for the hydroxyl groups in the octahedral layer of pyrophyllite are in good agreement with the 0.97 Å determined by Bridgeman *et al.* using a similar density functional method.[95] In contrast, relatively shorter values of 0.963 Å and 0.962 Å were obtained from a HF/3-21G* cluster model study.[76]

Inspection of Table 4.6, reveals that the orientation of the hydroxyl groups in the octahedral layer with respect to the *ab* plane is similar for each type of clay mineral. In the pyrophyllite model, with no isomorphic substitution, all hydroxyls tend to make a large angle, of on average ±28.7573°, with the *ab* plane. In the Texas-type montmorillonite models, with substitution in the octahedral layer, the hydroxyls on the opposite side of the layer to the proton cation tend to make a moderate angle, of on average -17.6181°, with the *ab* plane, while those on the same side make a small angle, of on average +1.5802°. In the Wyoming-type montmorillonite models, with substitution in the octahedral and tetrahedral layers, all hydroxyls tend to make a small angle, of on average ±10.9601°, with the *ab* plane.

Examination of Table 4.8 provides some insight into the apparent asymmetry in the orientation of hydroxyl groups in the Texas-type montmorillonite models. Though not immediately obvious, careful analysis shows that the angle a hydroxyl group in the octahedral layer makes with the *ab* plane decreases with proximity to both magnesium-for-aluminium substitution and proton counterion. The influence of magnesium substitution appears to be very localised and extend to hydroxyls on both sides of the layer, whereas that of the proton counterion is more long-range and effects only those hydroxyls on the same side of the layer as itself.

The orientation of the hydroxyl group located in the tetrahedral layer follow a much more simple trend, making a smaller angle with the *ab* plane closer to the magnesium-for-aluminium substitution.

Clay Mineral Lattice-Edge Unit Cells

Figure 4.4 shows the optimised pyrophyllite lattice-edge model. In the Texas-type montmorillonite lattice-edge model aluminium atom Al3 was substituted by magnesium and a proton counterion attached to oxygen atom O18. The vertical distance between neighbouring images, *i.e.*, between the top edge of the silicate layer and the periodic cell (as pictured) is approximately 6.0 Å, which was assumed to be large enough to be able to ignore interactions between periodic images.

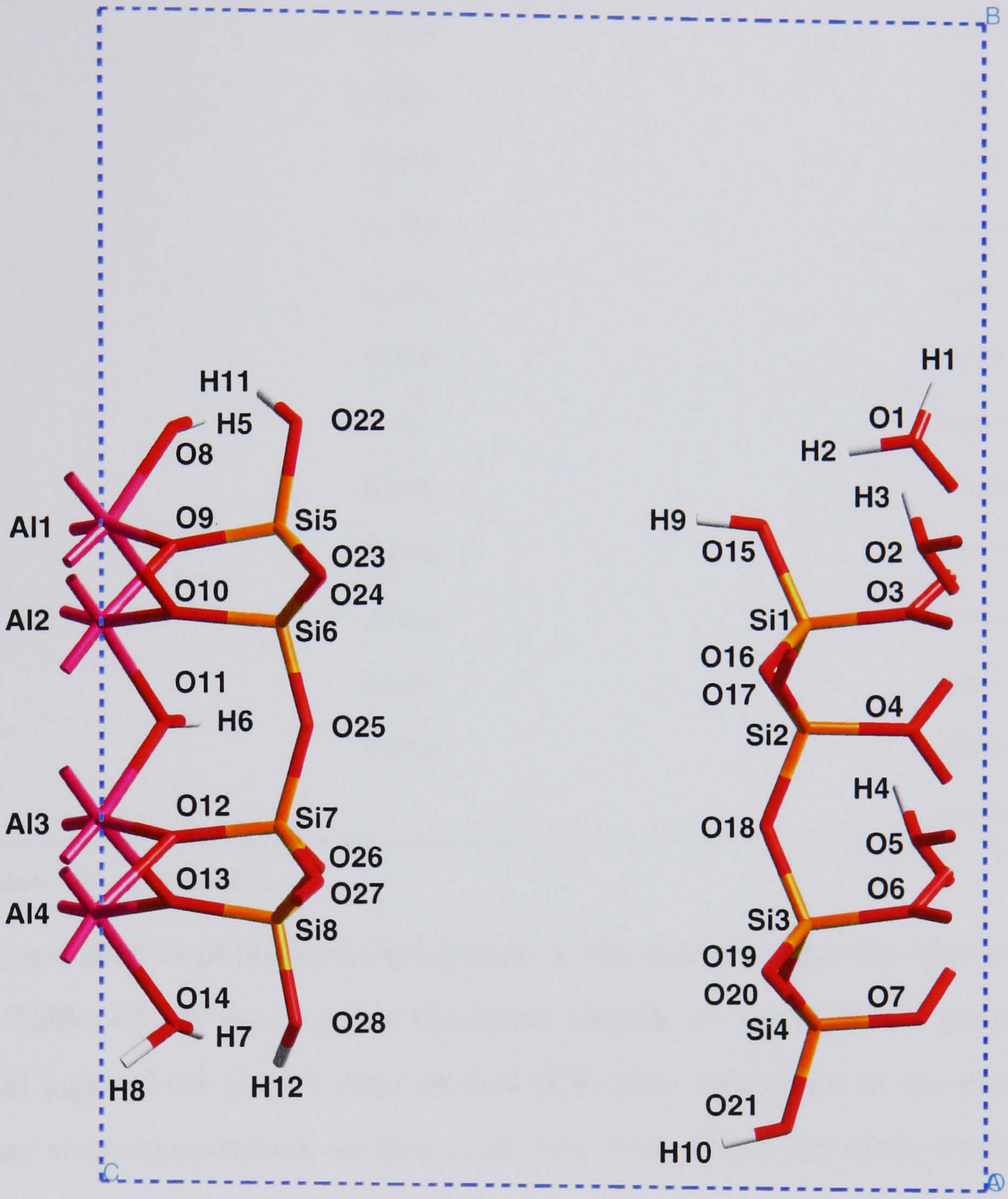

Figure 4.4: Optimised pyrophyllite lattice-edge unit cell. The colour scheme here is white for hydrogen, red for oxygen, pink for aluminium and yellow for silicon. Periodic boundaries are indicated by the blue dashed lines. The atoms are labelled according to their element type and number.

Table 4.7: O–H Bond Lengths of Optimised Clay Mineral Lattice-Edge Models[a]/Å

bond	pyrophyllite	Texas-type montmorillonite
O1–H1	0.9773	0.9803
O1–H2	0.9927	0.9867
O2–H3	0.9728	0.9737
O5–H4	0.9700	0.9745
O8–H5	0.9706	0.9717
O11–H6	0.9690	0.9703
O14–H7	0.9823	0.9803
O14–H8	0.9852	0.9814
O15–H9	0.9705	0.9710
O21–H10	0.9685	0.9704
O22–H11	0.9873	0.9812
O28–H12	0.9733	0.9665
O18–H13	-	0.9789

[a] Bond labels refer to Figure 4.4.

The bond lengths of the hydroxyl groups in the optimised lattice-edge models are listed in Table 4.7. If we compare the bond lengths of the hydroxyl groups in the octahedral layer of the lattice-edge models with their analogues in the models from which they were constructed, we find that they have about the same average value, but relative variations are very different.

Several new hydroxyl groups are created by modelling the broken crystal lattice. These can be grouped according to the atom type to which they are attached: four are directly bonded to silicon atoms (O15–H9, O22–H11, O28–H12, O21–H10); four compose the two water molecules co-ordinated to exposed aluminium atoms (O1–H1, O1–H2, O14–H7, 14–H8). In general, the length of the hydroxyl groups bonded to silicon are comparable to those in the octahedral layer, while those of the water molecules are a little longer, due in part to hydrogen bonding.

Effect of Degree of Isomorphic Substitution

The montmorillonite models exhibit a high degree of isomorphic substitution– a direct consequence of the size of our model systems, itself constrained by the limited computational resources available. The degree of substitution affects the charge density of clay mineral layers, which may influence the Brønsted acidity.

In order to justify the use of such small models it was necessary to investigate the influence of the degree of substitution on the Brønsted acidity of the hydroxyl groups in the models. For this purpose three larger models were constructed by replication of the optimised Texas-type 1 montmorillonite model, four times, in the **b** direction. Each exhibited a single magnesium-for-aluminium substitution in the octahedral layer, balanced by a proton counterion, forming a hydroxyl group in the tetrahedral layer. The position of the hydroxyl group in the tetrahedral layer relative to the magnesium-for-aluminium substitution was varied in each model. The three locations are indicated in Figure 4.5. Optimisation of the models was performed with one aluminium atom in the octahedral layer and all unit cell parameters fixed.

Table 4.8 lists the length and angle made with the *ab* plane of each hydroxyl group in the octahedral layer of the optimised large Texas-type 1 montmorillonite models. These were discussed earlier, in regard to the influence of isomorphic substitution on the length and orientation of hydroxyl groups in the octahedral layer. In the current context however we are concerned with the effect of charge density.

Let us consider the large Texas type 1 montmorillonite model with the hydroxyl group in the tetrahedral layer located at position (1), as in Figure 4.5. It exhibits a relative arrangement of isomorphic substitution and hydroxyl group similar to that found in the small Texas-type 1 montmorillonite model, while having a layer charge density four times smaller. Hydroxyl groups OH11, OH12, OH13 and OH14 in the large model are analogous to O1–H1, O9–H3, O4–H2 and O12–H4 in the small model. Comparison of their lengths shows that they are very similar, with a maximum difference of 0.0016 Å between any respective pair.

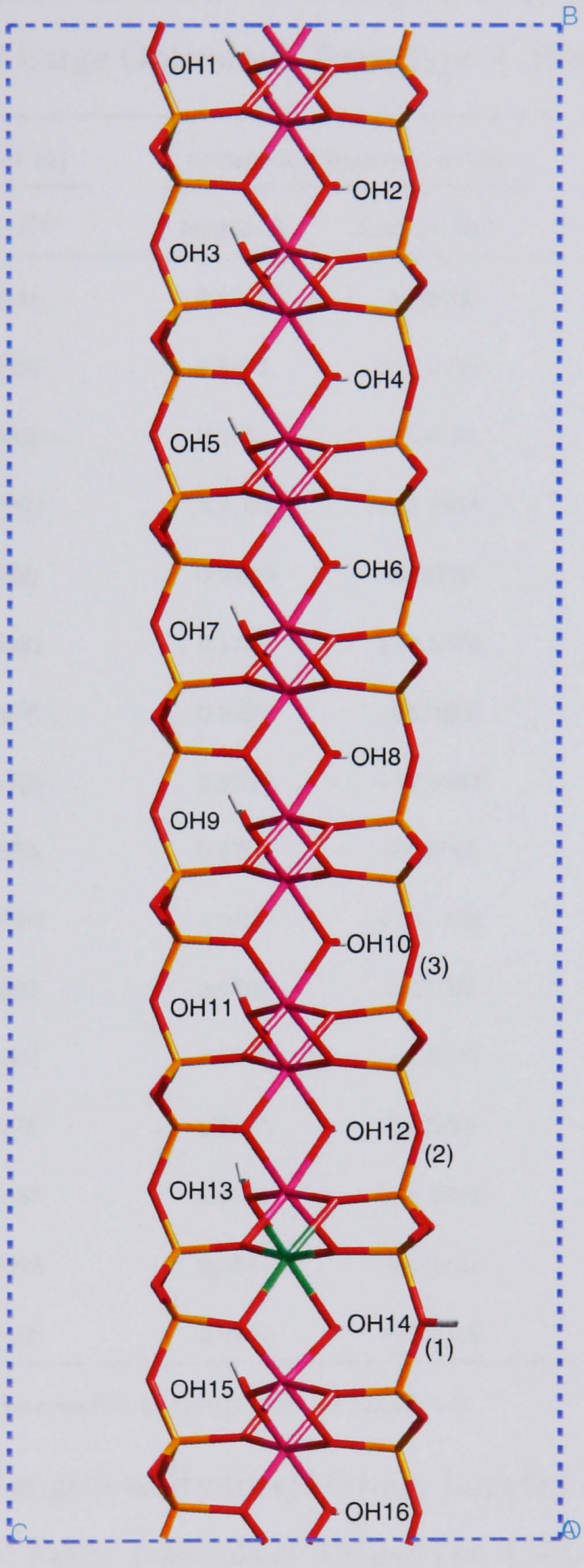

Figure 4.5: Optimised large Texas-type 1 montmorillonite unit cell. The colour scheme here is white for hydrogen, red for oxygen, green for magnesium, pink for aluminium and yellow for silicon. Periodic boundaries are indicated by the blue dashed lines.

Table 4.8: O–H Bond Lengths and *ab*-O–H Angles of Hydroxyl Groups Located in the Octahedral Layer of Large Optimised Texas-type 1 Montmorillonite Models[a]

	tetrahedral hydroxyl at (1)		tetrahedral hydroxyl at (2)		tetrahedral hydroxyl at (3)	
bond	length/Å	∠ *ab*–O–H/°	length/Å	∠ *ab*–O–H/°	length/Å	∠ *ab*–O–H/°
OH1	0.9704	-26.5684	0.9703	-40.3322	0.9716	-27.7345
OH2	0.9707	+23.6007	0.9699	+24.5795	0.9701	+23.9710
OH3	0.9706	-22.2425	0.9711	-25.3118	0.9722	-23.9104
OH4	0.9700	+22.2363	0.9704	+23.1848	0.9707	+22.7181
OH5	0.9699	-22.8800	0.9708	-25.6770	0.9716	-24.7159
OH6	0.9703	+23.8981	0.9701	+24.5578	0.9705	+23.1157
OH7	0.9706	-21.7676	0.9709	-22.8928	0.9715	-22.8303
OH8	0.9699	+22.1325	0.9716	+19.8843	0.9720	+16.4966
OH9	0.9700	-22.9236	0.9709	-23.4742	0.9703	-25.6399
OH10	0.9706	+22.7502	0.9720	+12.5709	0.9717	+11.8510
OH11	0.9706	-20.2697	0.9701	-22.7797	0.9681	-23.3322
OH12	0.9739	+6.1631	0.9742	+4.6690	0.9749	0.0000
OH13	0.9695	-11.1276	0.9675	-10.2882	0.9670	-7.8271
OH14	0.9720	+6.1931	0.9701	+13.1822	0.9697	+14.9828
OH15	0.9730	+21.3295	0.9715	-19.7010	0.9727	-17.2249
OH16	0.9736	+10.1903	0.9732	+13.8356	0.9734	+13.6439

[a] Bond labels and position of tetrahedral hydroxyl refer to Figure 4.5.

Table 4.9: O–H Bond Lengths of Hydroxyl Group Located in the Tetrahedral Layer and Relative Energies of Large Optimised Texas-type 1 Montmorillonite Models

location of hydroxyl group[a]	O–H/Å	Relative Energy/kJ mol^{-1}
(1)	0.9833	0.0
(2)	0.9813	12.5
(3)	0.9828	94.2

[a] Refer to Figure 4.5.

Table 4.9 lists the lengths of the hydroxyl groups in the tetrahedral layer of the large Texas-type 1 montmorillonite models. One can see that, when at position (1), the length of the hydroxyl group in the tetrahedral layer of the large Texas-type 1 montmorillonite model is 0.9833 Å, which is almost identical to 0.9834 Å, its value in the small model. More interesting are the total energies of the large models, also in Table 4.9, which indicate that it is preferable for the hydroxyl group in the tetrahedral layer to be close to the site of substitution in the octahedral layer

These findings suggest two important ideas: i) The overall charge density of a clay mineral layer has little effect on the length of structural hydroxyl groups and thus presumably on their Brønsted acidity—negative charge is localised around the sites of isomorphic substitution; ii) It is energetically most favourable for a proton to form a hydroxyl group with an oxygen atom in the tetrahedral layer, close to a site of isomorphic substitution. These observations go some way to justifying the use of the small clay mineral model systems.

4.4.4 Brønsted Acidity of Hydroxyl Groups Located in the Octahedral Layer

Hydroxyl groups in the octahedral layer lie behind the hexagonal ring-structure of the tetrahedral layer, which inhibits possible approach of the organic monomers. Figure 4.6 illustrates the increase in total energy as a methanal molecule moves through a hexagonal ring in the Texas-type 3 montmorillonite model, towards a hydroxyl group in the octahedral layer. The molecule was translated through the centre of the hexagonal ring with its carbonyl bond orientated perpendicular to the interlayer surface. The total energy was calculated with the methanal oxygen at various distances from the centre of the clay mineral layer. It was necessary to fix the methanal molecule and octahedral metal ions during optimisation. If these constraints were lifted the methanal molecule moved out of the hexagonal ring back into the interlayer nearer. The unit cell parameters were also kept fixed.

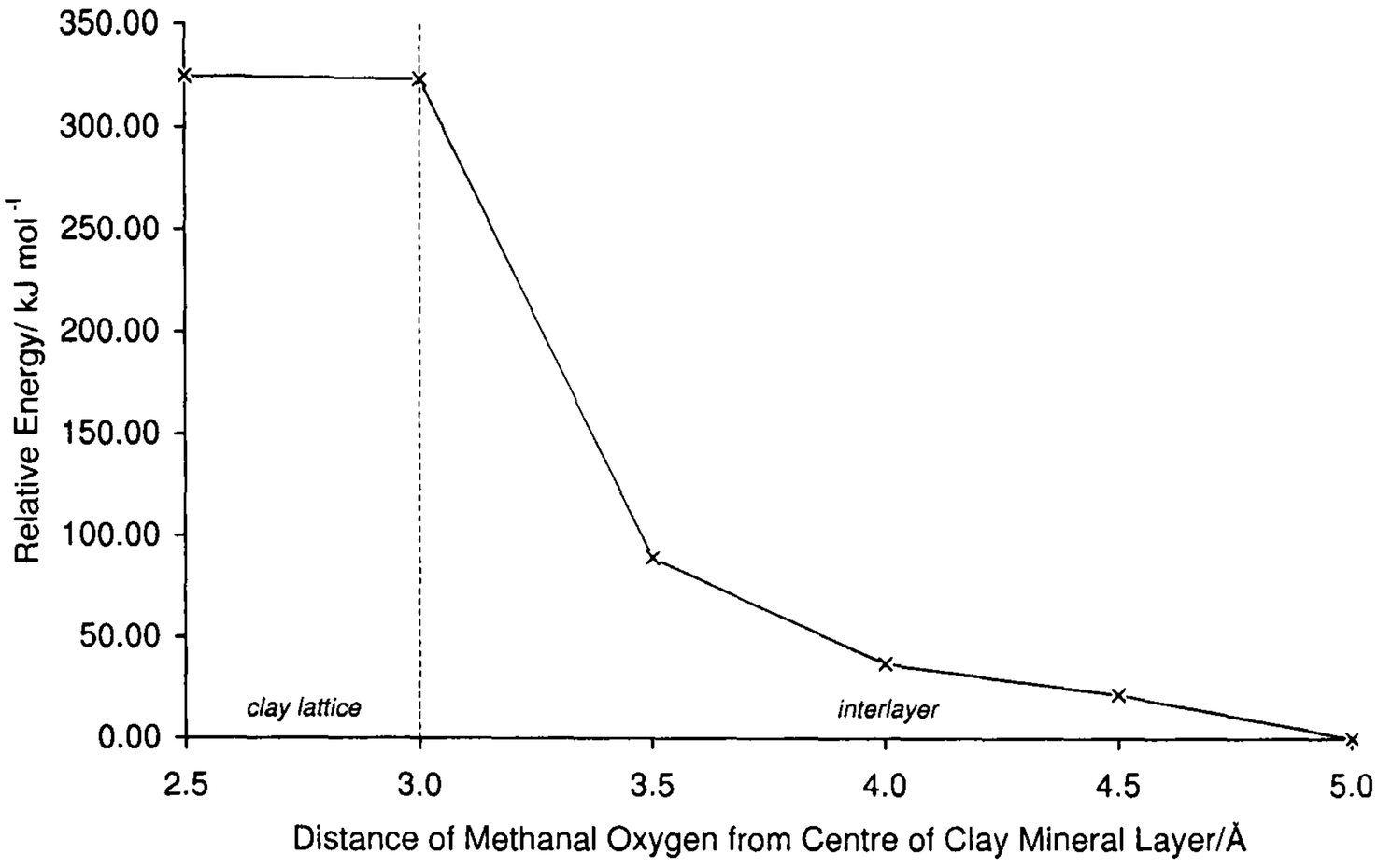

Figure 4.6: Increase in total energy as a methanal molecule moves through a silicate hexagonal ring in a Texas-type 3 montmorillonite model, towards a hydroxyl group in the octahedral layer.

It is concluded that the high energy barrier prohibits methanal molecules passing through a hexagonal ring and being protonated by a hydroxyl in the octahedral layer. It is possible that a water molecule, which is much smaller, could pass through a hexagonal ring, be protonated and then return to the interlayer as a Brønsted acid. This was not investigated.

4.4.5 Brønsted Acidity of Hydroxyl Groups Located in the Tetrahedral Layer

Hydroxyl groups in the tetrahedral layer are more accessible to the organic monomers than those in the octahedral layer. It can be seen from Table 4.5 that they are also, in general, marginally longer. In fact, protonation of methanal was not observed for any hydroxyl group in the tetrahedral layer of the montmorillonite models. In constrast, ethylenediamine was protonated in every case. This demonstrates again that protonation of a monomer by a clay mineral is mediated to some extent by the basicity of the molecule.

The weak Brønsted acidity of hydroxyl groups in the tetrahedral layer is in good agreement with observations reported by Trombetta *et al.*[126] The protonation of an ethylenediamine molecule would in fact inhibit its nucleophilic attack on methanal, which implies that the copolymerisation reaction is unlikely to be initiated by the hydroxyl groups in the tetrahedral layer.

For interest, protonation of methanal from the hydroxyl groups in the tetrahedral layer of the large Texas-type 1 montmorillonite models, described in Section 4.4.3, was also investigated. It was observed that protonation of methanal occurred when the hydroxyl group was located at site (3), shown in Figure 4.5, but not when it was at sites (1) or (2). In this position the positive proton counterion is located far from the negative site of isomorphic substitution and therefore is less tightly bound. It should be remembered however that, out of the three, this is also the energetically least favourable position for the hydroxyl group, reflected in the total energies listed in Table 4.9. The probable existence of such a labile proton is therefore very low. It is expected that most hydroxyl groups in the tetrahedral layer will be situated close to sites of isomorphic substitution, exhibiting low Brønsted acidity.

4.4.6 Brønsted Acidity of Hydroxyl Groups Located at the Lattice-Edge

It can be seen in Figure 4.4 that three types of hydroxyl group are identifiable at the clay mineral lattice-edge: i) those bonded to a silicon atom; ii) those bonded to an aluminium atom; and iii) those that compose water molecules co-ordinated to an aluminium atom. Protonation of methanal or ethylenediamine by such hydroxyl groups was not observed in either the pyrophyllite or Texas-type montmorillonite lattice-edge models. This implies that they are relatively less Brønsted acidic than hydroxyl groups in the tetrahedral layer.

The catalysis of the copolymerisation reaction of methanal and ethylenediamine is therefore also unlikely to be by Brønsted acid sites at the clay mineral lattice-edge.

4.4.7 Lewis Acidity at the Lattice-Edge

The catalysis of organic reactions by aluminium atoms exposed at the edges of clay mineral layers has been reported in the literature.[81,129] Two types of aluminium atom may be exposed in montmorillonite, those in the octahedral layer and those in the tetrahedral layer. Studies by Kubicki *et al.* identified the former as the active catalytic sites.[81] It was thought useful however to investigate the coordination of water, methanal and ethylenediamine to both.

In order to investigate the coordination of molecules to exposed aluminium atoms it was necessary to adjust the lattice-edge models. The atom labels for these are displayed in Figure 4.4. To model coordination to an exposed aluminium atom in the octahedral layer, water molecule H7–O14–H8 was removed. Molecules were then co-ordinated to aluminium atom Al4. To model coordination to an exposed aluminium atom in the tetrahedral layer, hydroxyl group O21–H10 was removed and silicon atom Si4 substituted by aluminium. Molecules were then co-ordinated to this aluminium atom. In this way models of water, methanal and ethylenediamine molecules co-ordinated to the specified Lewis acid sites were created and optimised.

This was done for both the Texas-type montmorillonite and pyrophyllite lattice-edge models. Pyrophyllite does not exhibit silicon-for-aluminium substitution in the tetrahedral layer. It was however still considered informative to investigate the coordination of molecules to an exposed aluminium atom in the tetrahedral layer of the pyrophyllite lattice-edge model, which could be thought representative of a montmorillonite with a very low degree of magnesium-for-aluminium substitution.

In addition, models with no molecule co-ordinated were optimised, to enable calculation of binding energies, from the following expression:

$$\Delta E = E_{clay+mol} - E_{clay} - E_{mol}, \tag{4.1}$$

where $E_{clay+mol}$ is the total energy of the clay mineral with a molecule co-ordinated. E_{clay} is the total energy of the clay mineral with no molecule co-ordinated and E_{mol} is the total energy of the molecule in a periodic box $(20\text{Å})^3$.

ΔE = -76.16 kJ mol^{-1}
ΔE = -79.81 kJ mol^{-1}

(a) Water.

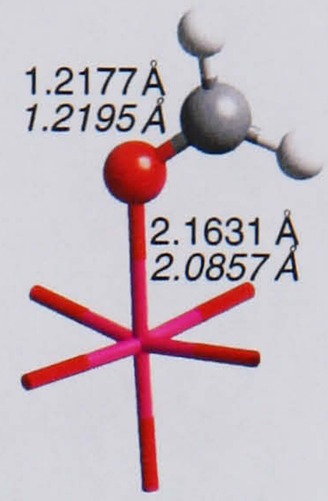

ΔE = -48.18 kJ mol^{-1}
ΔE = -52.89 kJ mol^{-1}

(b) Methanal.

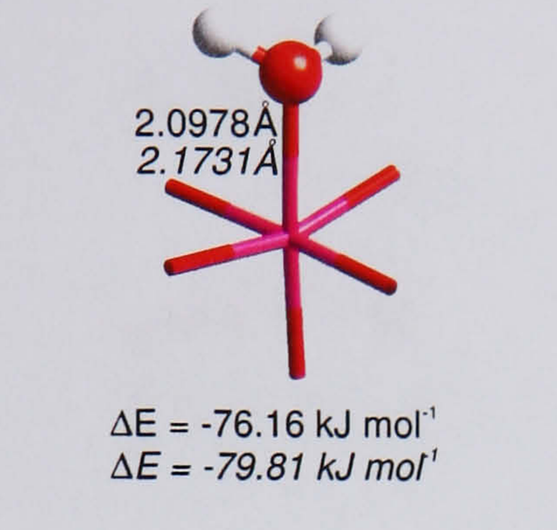

ΔE = -102.10 kJ mol^{-1}
ΔE = -103.33 kJ mol^{-1}

(c) Ethylenediamine.

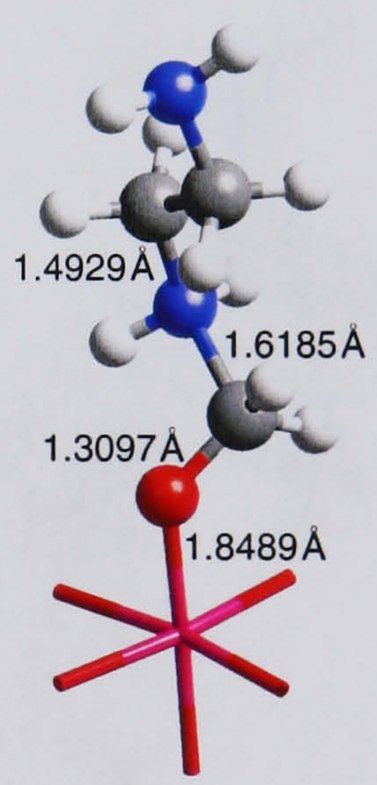

ΔE = -129.12 kJ mol^{-1}

(d) Hemiaminal.

Figure 4.7: Optimised geometries of species co-ordinated to an exposed aluminium atom in the octahedral layer of the Texas-type montmorillonite lattice-edge model. Note that the main clay mineral structure is not shown. The colour scheme here is white for hydrogen, grey for carbon, blue for nitrogen, red for oxygen and pink for aluminium. Bond lengths and adsorption energies for each model are presented, with analogous values for the pyrophyllite lattice-edge model also given in italics.

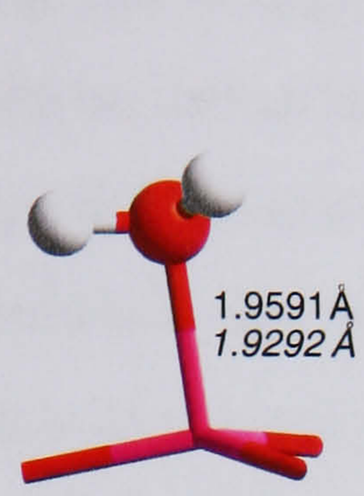

(a) Water.

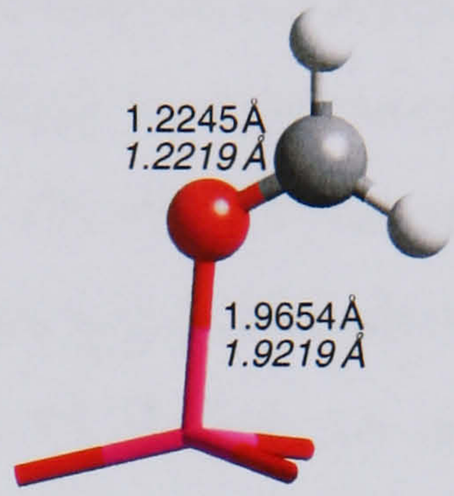

(b) Methanal.

(c) Ethylenediamine.

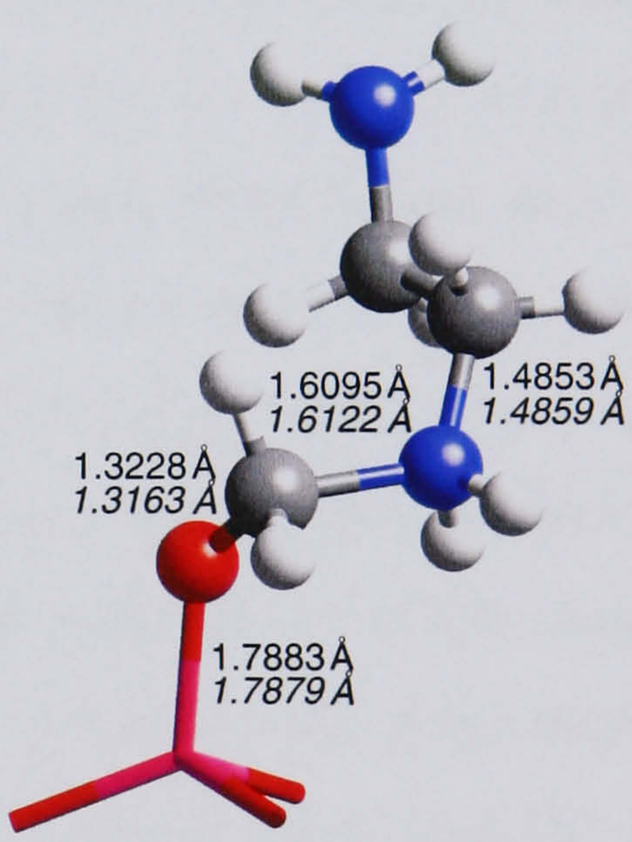

(d) Hemiaminal.

Figure 4.8: Optimised geometries of species co-ordinated to an exposed aluminium atom in the tetrahedral layer of the Texas-type montmorillonite lattice-edge model. Note that the main clay structure is not shown. The colour scheme here is white for hydrogen, grey for carbon, blue for nitrogen, red for oxygen and pink for aluminium. Bond lengths and adsorption energies for each model are presented, with analogous values for the pyrophyllite lattice-edge model also given in italics.

Prior to a discussion of the results it is helpful to remind ourselves of the nature of the clay mineral lattice-edge. In natural Wyoming montmorillonite about one in four hundred silicon atoms in the tetrahedral layer is substituted by aluminium. If we use the compositional data given in Section 4.2, simple calculations show that the ratio of aluminium atoms in octahedral sites to tetrahedral sites is about 150:1. Exposed aluminium atoms are therefore much more likely to be in the octahedral layer compared to the tetrahedral layer. In addition, the clay mineral lattice may be broken in an almost infinite number of different ways—the models represent only particular lattice-edges—though the same types of hydroxyl groups are expected to be present *i.e.*, Si–OH, Al–OH and Al–OH_2. The picture is thus quite complex.

In their experimental work Coveney *et al.* used dilute solutions of the monomers to synthesise nanocomposite materials.[116] Therefore the number of water molecules competing for the Lewis acid sites would be much greater than that of methanal and ethylenediamine. This could not be taken into account in the simulations due to the small size of the models, necessitated by the computational expense associated with first principles calculations. It is however an important consideration.

Figures 4.7 and 4.8 illustrate the optimised geometries of the monomers when co-ordinated to exposed aluminium atoms in the octahedral and tetrahedral layers of the Texas-type montmorillonite lattice-edge model. Note that the whole of the model is not shown. Selected bond lengths and calculated binding energies are also presented. Values for the analogous pyrophyllite models are given in italics.

It is apparent that, for each of the Lewis acid sites studied, calculated binding energies decrease from ethylenediamine, to water, to methanal. This implies that the fraction of methanal molecules co-ordinated to exposed aluminium atoms at the clay mineral lattice-edge will be relatively low, as compared to water or ethylenediamine. The coordination of methanal to the Lewis acid sites is however, believed to be the initial step in Lewis acid catalysed copolymerisation reactions, the second being the nucleophilic attack of ethylenediamine. This raises a concern over the actual driving force for the reaction, if indeed it does occur at the clay mineral edge.

The preferential binding of ethylenediamine to exposed aluminium atoms inhibits a Lewis acid catalysed copolymerisation reaction in two ways. In the first instance, sites occupied by ethylenediamine cannot be occupied by methanal. In addition, bound ethylenediamine is unable to react with any methanal that is co-ordinated to a Lewis acid site. It is thought, however, that at any point in time a fraction of methanal molecules will be co-ordinated to Lewis acid sites and a proportion of ethylenediamine molecules will be in solution so that copolymerisation will occur, driven by the favourable reaction of ethylenediamine with co-ordinated methanal.

The energy gained by the reaction of ethylenediamine with co-ordinated methanal is equal to the difference in the binding energies of the hemiaminal and methanal. This gives a value of about -150 kJ mol^{-1} for methanal co-ordinated to exposed aluminium atoms in the tetrahedral layer and -80 kJ mol^{-1} for that co-ordinated to exposed aluminium atoms in the octahedral layer. The exothermic reaction would therefore act as a driving force for copolymerisation. Note that ethylenediamine did not react with methanal co-ordinated to an exposed aluminium atom in the octahedral layer of pyrophyllite and thus no data exists for a hemiaminal structure.

Quite surprising is the relative difference in binding energies for the Texas-type montmorillonite and pyrophyllite lattice-edge models. For molecules co-ordinated to an exposed aluminium atom in the octahedral layer the values are very similar, but for those co-ordinated to an exposed aluminium atom in the tetrahedral layer an average difference of 37.43 kJ mol^{-1} is observed. These results imply that magnesium-for-aluminium substitution in the octahedral layer influences the Lewis acidity of exposed aluminium atoms in the tetrahedral layer to a much greater extent than those in the octahedral layer. This is manifest in the geometry of the optimised lattice-edge models with no molecules co-ordinated, shown in Figure 4.9. In both models the exposed aluminium atom makes a fourth bond with the oxygen atom of the nearest hydroxyl group, to try and obtain tetrahedral coordination. In the case of the pyrophyllite lattice-edge model the length of the bond between the aluminium atom and hydroxyl oxygen is 2.1263 Å, with the other three co-ordinating oxygen

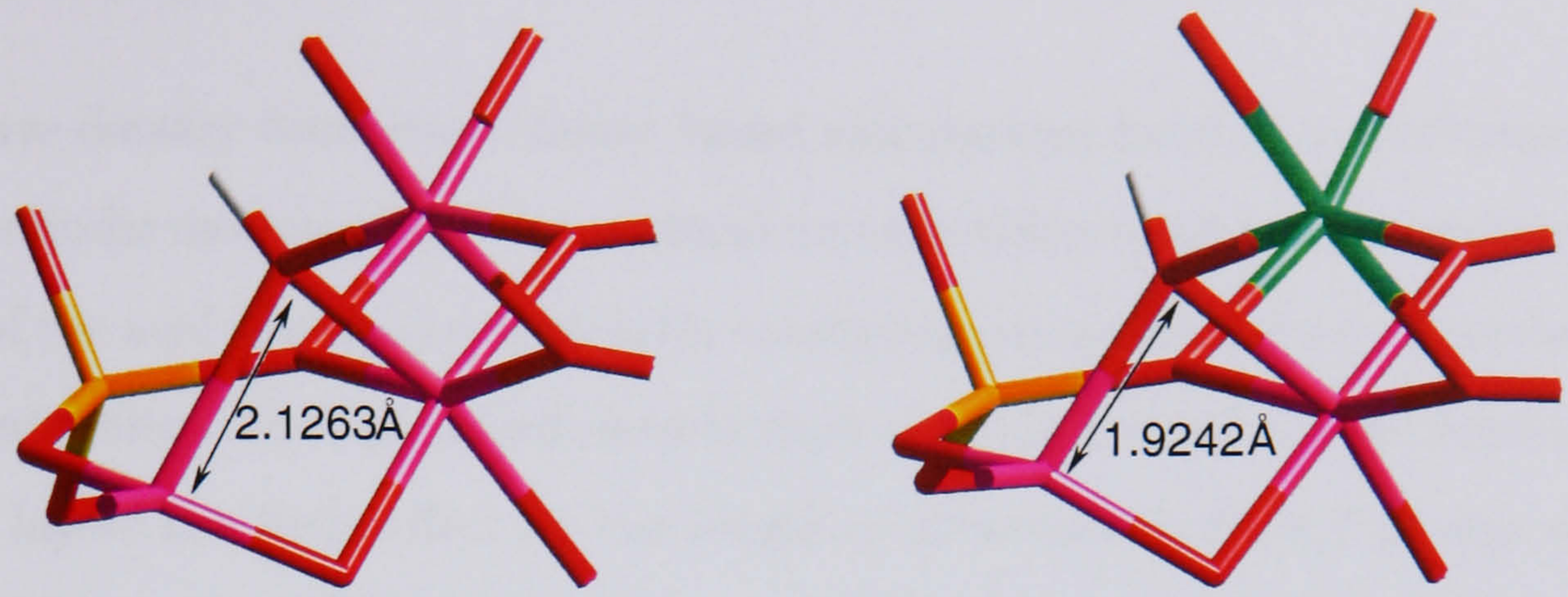

(a) Pyrophyllite. (b) Texas-type montmorillonite.

Figure 4.9: Fragments showing the local geometry of an exposed aluminium atom in the optimised pyrophyllite and Texas-type montmorillonite lattice-edge models. The colour scheme here is white for hydrogen, red for oxygen, green for magnesium and pink for aluminium.

atoms more or less lying together in a plane with the aluminium atom. In the Texas-type montmorillonite lattice-edge model however, the bond between the aluminium atom and hydroxyl oxygen is shorter at 1.9242 Å and the oxygen atoms co-ordinate in a more tetrahedral manner. Such large differences in structure are not observed between the lattice-edge models with exposed aluminium atoms in the octahedral layer.

In spite of the apparent catalytic behaviour shown by exposed aluminium atoms at the lattice-edge, many questions remain over the copolymerisation mechanism. For instance, the next step after formation of the hemiaminal must be the loss of a proton from the nitrogen atom. This could then act as a Brønsted acid and the reaction would then proceed via a mixture of both Brønsted and Lewis acid catalysis. Factors such as solvation have also not been addressed. Further work needs to be done to resolve such issues.

4.5 Conclusions

Planewave density functional theory based calculations have been performed to optimise periodic models of the clay mineral montmorillonite and to investigate the potential of the acid sites in the models for catalysing copolymerisation of methanal and ethylenediamine. The optimised models show that the overall charge density of clay mineral layers has little effect on the length of structural hydroxyl groups and thus presumably on their Brønsted acidity—negative charge is localised around the sites of isomorphic substitution. It is energetically most favourable for a proton to form a hydroxyl group, with an oxygen atom in the tetrahedral layer, close to sites of isomorphic substitution, where it is least Brønsted acidic. Protonation of methanal is not observed from water associated with sodium and calcium cations. hydroxyl groups in the octahedral or tetrahedral layers or at the clay mineral lattice-edge. This indicates that Brønsted acid catalysis is improbable. Catalysis has been shown to occur at the clay mineral lattice-edge where exposed aluminium atoms act as Lewis acid sites, although the full copolymerisation mechanism is still unclear.

Chapter 5

The Hofmann-Klemen Effect

Montmorillonite is a 2:1 layer type aluminosilicate belonging to the group of clay minerals known as smectites. It comprises an octahedral alumina layer fused between two tetrahedral silica layers. The partial substitution of octahedral aluminium by magnesium or iron and tetrahedral silicon by aluminium creates a negative structural charge that is balanced by metal cations adsorbed into the space between layers, known as the interlayer. Hydration of the cations means that it is normal for a certain amount of water to also be accommodated within the interlayer; as relative humidity rises the quantity of water adsorbed increases and the interlayer expands in order to accommodate the greater molecular volume between the layers.[140,141] This is known as clay swelling.

The swelling of clay minerals has been studied extensively by experiment[140,141] and simulation[135,142–149] and its dependence on interlayer cation species and degree and type of isomorphic substitution is now generally well understood. However, one related phenomenon that still attracts attention is the Hofmann-Klemen effect, which describes the observed reduction in expandable character and cation exchange capacity (CEC) of lithium saturated montmorillonite upon mild heating (200-300 °C).[150] It remains of interest since several important questions, reagarding the reaction mechanism, remain unanswered.

It is accepted that the observed changes in swelling properties and CEC are due to the lithium ions becoming fixated within the layer structure of the clay mineral—movement of the cations into the clay lattice decreases the number accessible for hydration and exchange, reducing the enthalpic driving force for the adsorption of water and subsequent swelling. However, some uncertainty still exists over the precise location of the lithium ions within the clay framework. It has been suggested that the cations migrate from the interlayer (Figure 5.1 site (a)) into the ditrigonal cavities of the tetrahedral layer (Figure 5.1 site (b)),[151–153] the vacant octahedral sites (Figure 5.1 site (c)),[154–156] or both of these.[88,157–161]

Tettenhorst was one of the first to argue that migration of cations occurs from the interlayer into the ditrigonal cavities of the tetrahedral layer without deeper penetration into unfilled octahedral sites, based on a lack of association of the metal cations with apical oxygens, inferred from infrared spectroscopy.[151] More recent evidence for the location of the cations exclusively in the ditrigonal cavities exists in the form of two complementary magic angle spinning nuclear magnetic resonance (MAS-NMR) studies. ^{27}Al MAS-NMR carried out by Alvero *et al.* showed distortion of the tetrahedra of oxygen atoms surrounding aluminium in the tetrahedral layer, attributed to lithium ions located in ditrigonal cavities.[152] This was supported by demonstration of the reversible migration of lithium ions in montmorillonite under high water vapour pressure, which implies that in a collapsed clay mineral the cations are situated close to the interlayer region where the water molecules can access them. ^{7}Li MAS-NMR performed by Theng *et al.* showed that the low symmetry chemical environment of lithium ions in heated montmorillonite is very different from those occupying octahedral sites in hectorite and lepidolite, indicating their location in distorted ditrigonal cavities.[153]

No authors claim lithium ions migrate exclusively to vacant octahedral sites, however some imply this by lack of any mention of cations being present in the ditrigonal cavities.[154–156] Evidence offered for the occupation of vacant octahedral sites has come almost entirely from infrared studies,[154–161] which compare the spectra

of untreated and thermally treated lithium montmorillonite, particularly those bands assigned to hydroxyl stretching and bending modes, found between 3300-3800 cm^{-1} and 650-1000 cm^{-1}, respectively. In addition, some investigations also examine Si-O vibrational modes, in the 400-1300 cm^{-1} region.[156,159–161]

One of the most important infrared studies is that by Calvet and Prost who reported the appearance of dichroic bands in the hydroxyl-stretching region of the infrared spectrum of lithium montmorillonite upon heat treatment.[157] These were attributed to hydroxyl groups orientated perpendicular to the *ab* plane, since they do not contribute to the absorption under normal incidence. Computations based on a point charge model presented in the same paper showed that in montmorillonite structural hydroxyl groups reorientate perpendicular to the *ab* plane upon filling of vacant octahedral sites. This led the authors to conclude that the appearance of dichroic bands was indicative of migration of lithium cations to the octahedral layer. Many subsequent studies have cited observation of similar bands as evidence for the migration of lithium ions to vacant octahedral sites.[154,156,159,161]

A possible explanation for discrepancies in the location of the lithium cations is provided by most recent investigations which indicate that the sites to which lithium ions migrate is dependent on the degree and type of substitution exhibited by the montmorillonite.[156,161] More specifically, migration to octahedral sites is most favourable when the degree of substitution in the octahedral layer is high and that in the tetrahedral layer is low, whereas when the degree of substitution in the octahedral layer is low and that in the tetrahedral layer is high migration is almost exclusively to ditrigonal cavities. The same studies also show that only a small percentage of lithium ions that migrate to the ditrigonal cavities are irreversibly trapped and so fixation is highest when migration is primarily to octahedral sites. Observations are therefore very sample dependent.

Further insight into the effect of isomorphic substitution on lithium migration is afforded by classical Monte Carlo and molecular dynamics studies of hydrated lithium montmorillonite.[145,147] These simulations show that the location of lithium

cations in the interlayer is greatly influenced by the isomorphic substitution present in the tetrahedral and octahedral sheets. Two types of lithium solvation complex are observed: (i) inner-sphere complexes strongly bound to isomorphic substitution sites in the tetrahedral sheet; (ii) outer-sphere complexes loosely associated with isomorphic substitutions sites in the octahedral sheet. Similar complexes have been reported for montmorillonite saturated with sodium,[144] potassium,[146] and cesium.[148] One could therefore postulate that the electrostatic interaction between lithium cations and tetrahedral aluminium is so great that it prevents further migration into vacant octahedral sites. Density functional studies of montmorillonite have also shown the tendency of cations to lie close to sites of tetrahedral substitution.[87,96]

In fact, it has proved useful to many authors to study the thermal treatment of montmorillonites saturated with other cations as part of their investigation of the Hofmann-Klemen effect.[155,157–160] Larger counterions (*e.g.* Rb^+, Cs^+, Cd^{2+}) are considered unable to enter fully into the ditrigonal cavities, while those of slightly smaller size (*e.g.* Na^+, Cu^{2+}) do so, but only small cations (*e.g.* Mg^{2+}, Li^+) are able to penetrate further in order to occupy vacant octahedral sites.

A concise summary of properties necessary for observation of the Hofmann-Klemen effect has been presented by Srasra *et al.*[154] who suggest the following: i) exchangeable cation with radius smaller than 0.7 Å; ii) vacancies in the octahedral sheet; and iii) at least a fraction of the lattice charge originating from substitution in the octahedral sheet.

In spite of the considerable literature on the migration of lithium cations from the interlayer into vacant octahedral sites, very few authors give any indication of how this may occur. Examination of the structure of montmorillonite shows that the steric hindrance imposed by hydroxyl groups inhibits migration of lithium cations from ditrigonal cavities into vacant octahedral sites, Figure 5.1. The only authors to comment on the matter are Ebina *et al.* who suggest that thermal treatment leads to the vigorous movement of the hydroxyl-hydrogens, which act as a "crossing gate" making lithium migration possible.[88]

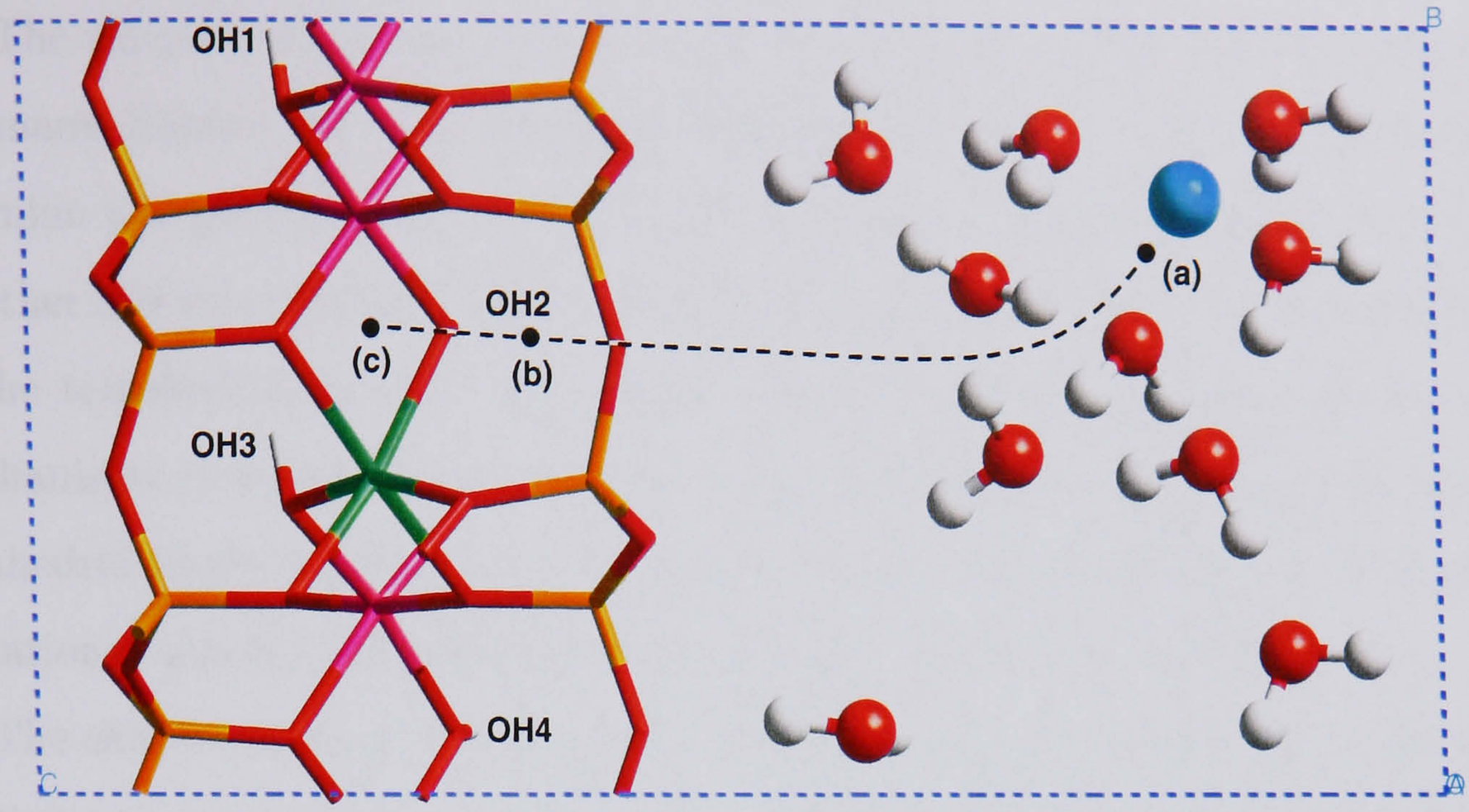

Figure 5.1: Lithium montmorillonite unit cell. Upon thermal treatment the lithium cations are thought to migrate from the interlayer (a) into the ditrigonal cavities of the tetrahedral layer (b), the vacant octahedral sites (c), or both of these. The colour scheme here is white for hydrogen, blue for lithium, red for oxygen, green for magnesium, pink for aluminium and yellow for silicon. Periodic boundaries are indicated by the blue dashed lines.

Two possible ways by which lithium cations may overcome the steric hindrance of the hydroxyl groups have been suggested (i) that lithium ions react with hydroxyl groups to release protons[152,162,163] and (ii) that dehydroxylation of montmorillonite facilitates migration of cations into vacant octahedral sites.[164] Dehydroxylation is normally considered to occur at much higher temperatures (> 500 °C).[131,132] Some authors imply however, that it may begin at temperatures as low as 200 °C.[165] It is interesting to note that Muller *et al.* report a shift from 3632 cm^{-1} to 3664 cm^{-1} for the main hydroxyl stretching band in the infrared spectrum of montmorillonite, as it transforms from *cis* to *trans*-vacant via dehydroxylation-rehydroxylation.[132] This is because it is similar to the shift from 3630 cm^{-1} to 3670 cm^{-1} reported and assigned by Calvet and Prost to an AlMgOH configuration changing to AlMgLiOH during heat treatment of lithium montmorillonite.[157]

The purpose of the present chapter is to provide theoretical insight into the Hofmann-Klemen effect by employing density functional theory based methods to examine the phenomenon at the quantum level. More specifically, we investigate whether it is more favourable for the lithium cation to reside in the ditrigonal cavities of the tetrahedral layer or the vacant octahedral sites. We also examine possible mechanisms of migration of lithium cations from the ditrigonal cavity to a vacant octahedral site by deprotonation or dehydroxylation of the clay mineral. In addition, vibrational spectra are calculated and compared with experimental data.

The chapter is organised as follows. In Section 5.1, we outline the model systems studied and the computational methods employed. This is followed by a discussion of the results of the simulations in Section 5.2, starting with the optimised models, moving on to the *ab initio* molecular dynamics and finishing with the predicted vibrational spectra. Finally, in Section 5.3 we draw some conclusions.

5.1 Simulation Details

In this section we describe the model systems and methods used to perform geometry optimisation, *ab initio* molecular dynamics and to calculate vibrational spectra. We also give some brief computational details concerning the calculations.

5.1.1 Model Systems

The unit cell of *cis*-vacant pyrophyllite described in the previous chapter was utilised. Pyrophyllite has very similar aluminosilicate layers to montmorillonite, but exhibits no isomorphic substitution in either the tetrahedral or octahedral layer.

From the *cis*-vacant pyrophyllite cell, a *cis*-vacant lithium montmorillonite model was developed, with a unit cell formula of $LiMgAl_3(OH)_4(Si_4O_{10})_2]$, corresponding to one isomorphic substitution of aluminium by magnesium in the octahedral layer balanced by a lithium cation. Two variations were fabricated, one with the cation located in a ditrigonal cavity of the tetrahedral layer and a second with it situated

in a previously vacant octahedral site. These represented a montmorillonite with a relatively high degree of isomorphic substitution in the octahedral layer. In the natural material approximately one in eight aluminium atoms in the octahedral layer and one in four hundred silicon atoms in the tetrahedral layer undergo substitution. However, to model such ratios exactly would have required a model so large as to make the simulations intractable. Calculations described in the previous chapter however indicate that the influence of sites of isomorphic substitution is localised rather than delocalised over the layers. This implies that although such small models do not represent the average composition of montmorillonite layers, they are a good approximation to the part of a layer around a site of isomorphic substitution.

To position the lithium cation in a ditrigonal cavity the unit cell c parameter was fixed at 12 Å and a short (0.1ps) molecular dynamics simulation was performed as outlined in Section 5.1.2. The cation, initially located at the centre of the cell, equidistant between the clay layer and its periodic image, moved directly into a ditrigonal cavity during dynamics. For the second model the lithium cation was placed in a vacant octahedral site by hand. Each model was assigned an initial interlayer spacing of 9.60 Å before optimisation, which corresponds to a unit cell c parameter of approximately 9.75 Å, determined from reported swelling data for lithium montmorillonite.[144]

In addition, partially deprotonated and dehydroxylated analogues were created. In the deprotonated models one hydroxyl-hydrogen was removed and placed in the interlayer, while in the dehydroxylated models one hydroxyl group and one hydroxyl-hydrogen *i.e.*, H_2O was deleted. In both cases species were removed from the hydroxyl group(s) in closest proximity to the cation.

For comparison purposes an additional model with the cation residing in the interlayer, hydrated by ten water molecules, was generated from the optimised model with the lithium cation in a ditrigonal cavity. The model was given a d-spacing of 17.00 Å, which corresponds to a unit cell c parameter of approximately 17.26Å. again based on previously reported swelling data for lithium montmorillonite.[144]

5.1.2 Simulation Methods

Geometry optimisation and molecular dynamics simulations were performed with the density functional theory based CASTEP code,[137] which utilises periodic boundary conditions, a planewave basis set and **k**-point sampling. Ultrasoft pseudopotentials were employed.[42] The energy cut-off for the planewave expansion was 340 eV and just one special **k**-point was allowed in the Brillouin zone, situated at (0.25,0.00,0.00). For all simulations the gradient corrected PW91 exchange-correlation functional was used,[61,62] just as in the calculation described in the previous chapter.

Geometry optimisation simulations were performed with all atomic positions and cell parameters allowed to vary. In order to allow calculation of differences in total energy between cells of different volume at a relatively low energy cut-off a finite basis set correction was applied.[138] This corrects total energies for errors due to the use of a finite **k**-point set in a finite cut-off energy calculation.

Molecular dynamics simulations were performed within the canonical (N,V,T) ensemble using a timestep of 1.0 fs. For the model systems, with the lithium cation located in a ditrigonal cavity or octahedral site, a total of 3.0 ps was obtained at temperatures of 300 K and 573 K, while for the hydrated model just 2.5 ps was recorded at a temperature of 300 K.

5.1.3 Calculation of Power Spectra

Vibrational power spectra were calculated for all systems from the temporal Fourier transform of the velocity autocorrelation function (VACF) determined from the molecular dynamics simulations at 300 K. In each case the first 0.5 ps was allowed as equilibration time and the VACFs calculated over the remaining time. The VACFs were calculated up to the maximum value, with the time origins at every time step, but truncated at 0.4 ps prior to Fourier transformation, giving a resolution of 41.67 cm^{-1} (or $\pm$1.2 THz).

5.1.4 Computational Details

The computational cost of *ab initio* molecular dynamics necessitates the use of parallel machines. The majority of calculations were run on a Silicon Graphics Onyx2 mounted with sixteen 400MHz MIPS R12000 processors and 8GB RAM. Some were also performed on an 816-processor CRAY T3E-1200E. The CASTEP code scales well up to 16 processors for our systems.

5.2 Results and Discussion

In this section we discuss the results of our simulations. It begins with details of the optimised periodic lithium montmorillonite structures. This is followed by an account of observations made from the *ab initio* molecular dynamics simulations. Finally we analyse the calculated power spectra.

5.2.1 Optimised Structures

Figures 5.2(a) and 5.2(b) illustrate the optimised montmorillonite models with the lithium cation located in a ditrigonal cavity of the tetrahedral layer and an octahedral site, respectively. These will subsequently be referred to as the Li-tetra and Li-octa models, respectively.

Deprotonation and dehydroxylation were not observed during the optimisation of the models. This is unsurprising since these were 0K calculations, where thermal energy is not considered. The unit cell parameters of the optimised models are listed in Table 5.1. Those reported from crystallographic data for montmorillonite are also listed for comparison;[130] although no information was available on the exact nature of the sample, it is presumed to be a natural, dehydrated clay. The calculated unit cell parameters show little deviation from those reported from experiment. The only interesting result is the larger a and b parameters exhibited by the Li-octa model, required to accommodate the lithium cation in the octahedral layer.

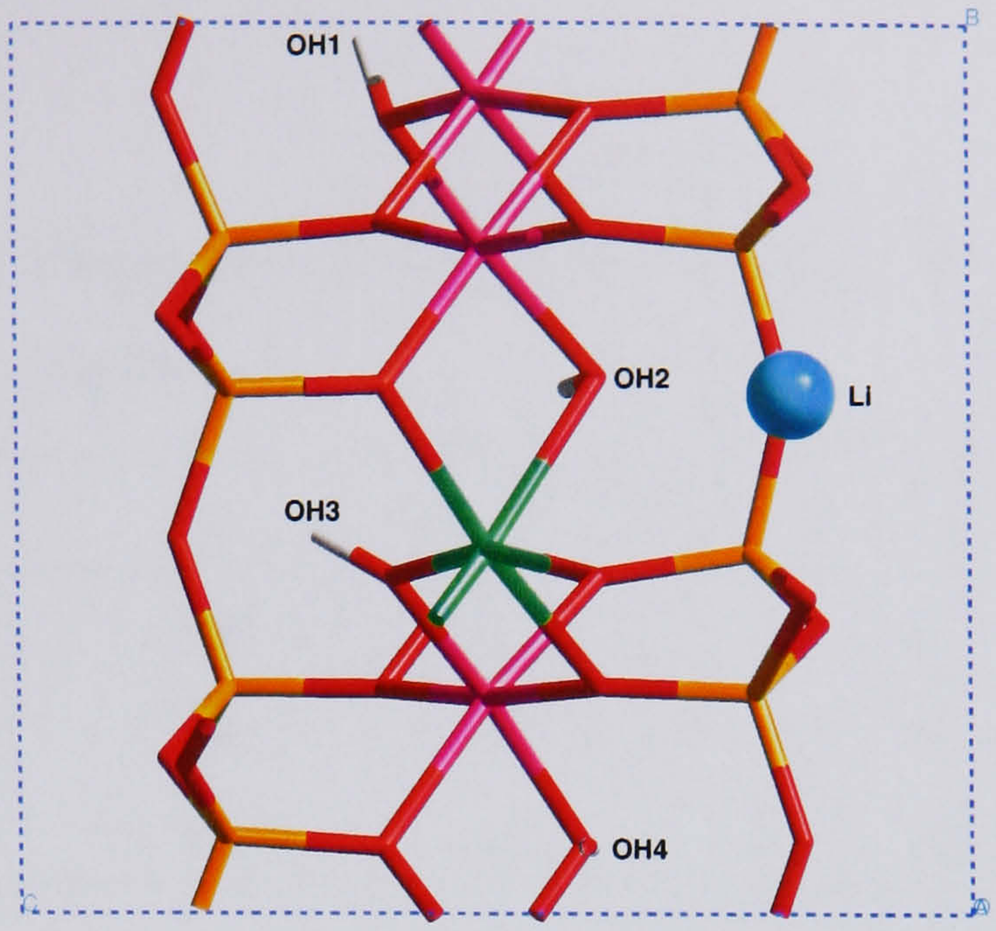

(a) Optimised lithium montmorillonite unit cell with cation situated in a ditrigonal cavity of the tetrahedral layer.

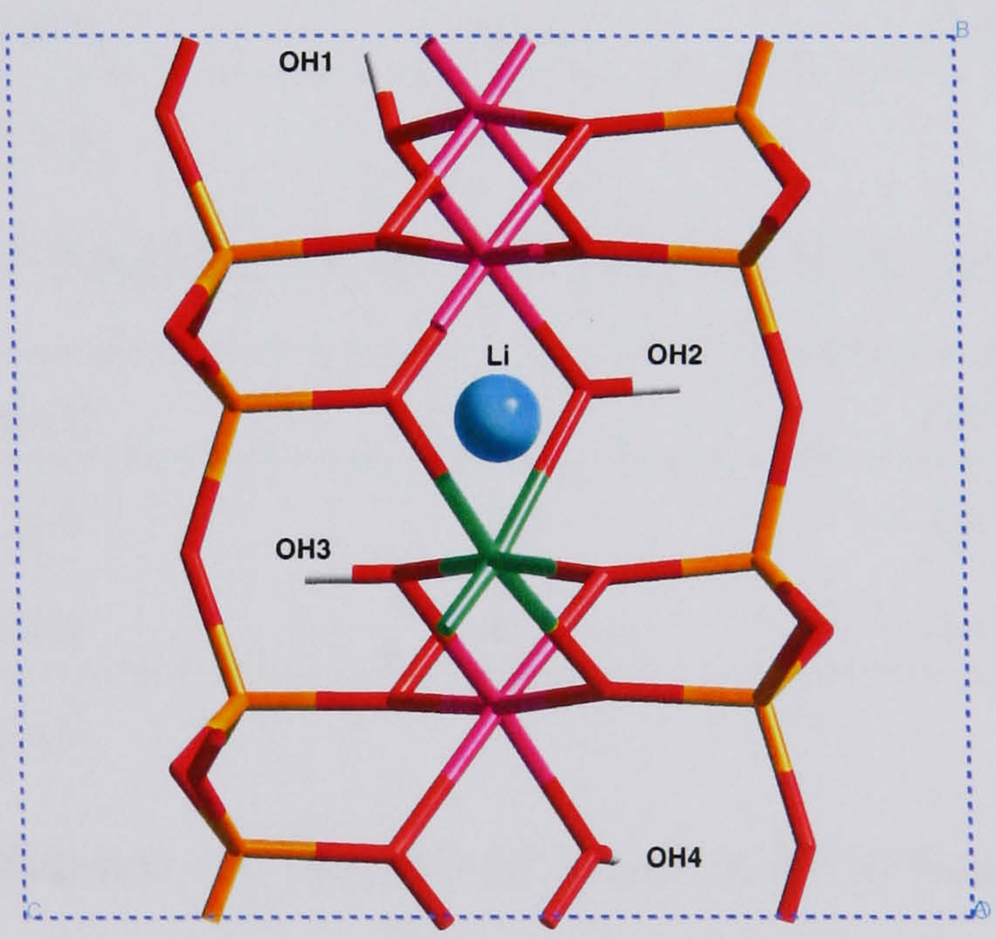

(b) Optimised lithium montmorillonite unit cell with cation situated in an octahedral site.

Figure 5.2: Optimised lithium montmorillonite models. The colour scheme here is white for hydrogen, blue for lithium, red for oxygen, green for magnesium, pink for aluminium and yellow for silicon. Periodic boundaries are indicated by the blue dashed lines.

Table 5.1: Unit Cell Parameters of Optimised Lithium Montmorillonite Models: Lengths are in Å and Angles in °

model	a	b	c	α	β	γ
experiment[130]	5.18	8.96	9.97	90.0	99.9	90.0
Li-tetra	5.19	9.00	9.77	89.0	97.3	90.3
Li-octa	5.21	9.02	9.77	88.6	97.5	90.0

Table 5.2: O–H Bond Lengths of Optimised Lithium Montmorillonite Models[a]/Å

model	OH(1)	OH(2)	OH(3)	OH(4)
Li-tetra	0.973	0.981	0.966	0.974
Li-octa	0.974	0.972	0.971	0.974

[a] Bond labels refer to Figure 5.2.

Table 5.3: *ab*–O–H Angles of Optimised Lithium Montmorillonite Models[a]/°

model	OH(1)	OH(2)	OH(3)	OH(4)
Li-tetra	-15.9	-18.0	-51.9	+3.5
Li-octa	-12.0	+82.7	-89.5	+11.5

[a] Bond labels refer to Figure 5.2.

Table 5.4: Li–O Distances of Optimised Lithium Montmorillonite Models[a]/Å

model	Li–O1	Li–O2	Li–O3	Li–O4	Li–O5	Li–O6	Li–O7
Li-tetra	2.538	2.307	2.724	2.654	2.795	2.298	1.976
Li-octa	2.198	2.167	2.383	2.070	2.042	2.128	-

[a] Bond labels refer to Figures 5.3 and 5.4.

The total energy of the optimised Li-octa model was 87.9 kJ mol^{-1} lower than that of the Li-tetra model, which indicates that it is energetically more favourable for the lithium cation to reside in an octahedral site than within a ditrigonal cavity of the tetrahedral layer. This is probably due to the closer proximity of the lithium cation to the negative charge site when in the octahedral layer, increasing favourable coulombic interactions. The lithium-magnesium distances are 3.545 Å and 2.973 Å for the optimised Li-tetra and Li-octa models, respectively. Ebina *et al.* performed density functional based calculations on cluster models of lithium montmorillonite and reported analogous lithium-magnesium distances of 3.535 Å and 2.610 Å.[88] The reason for the comparatively shorter lithium-magnesium distance calculated by these authors, in the case where the lithium cation is located in an octahedral site, is probably due to their employment of a local geometry optimisation method. The idea that increased proximity of lithium cations to isomorphic substitutions in the octahedral layer increases stability corroborates experimental observations that fixation in octahedral sites is greatest when the degree of substitution in the octahedral layer is high.[156,161]

The bond lengths of the hydroxyls present in our optimised models are listed in Table 5.2. The hydroxyl bond lengths are all very similar to one other. The longest hydroxyl bond is that whose oxygen is co-ordinated to a lithium ion located in a ditrigonal cavity *i.e.* OH2 of the Li-tetra model.

The angle that each hydroxyl group present in the optimised models makes with the *ab* plane is listed in Table 5.3. The Li-octa model exhibits two hydroxyls making an angle of approximately 90 ° to the *ab* plane and two lying parallel to the plane. Such large angles are not observed for the Li-tetra model. These results confirm the simple calculations of Calvet and Prost who, as we discussed earlier, reported that the filling of vacant octahedral sites in montmorillonite results in stability only if neighbouring structural hydroxyl groups reorientate perpendicular to the *ab* plane—the dichroic nature of hydroxyl stretching bands observed in the infrared spectrum of heat-treated lithium montmorillonite being a corollary of this.[157]

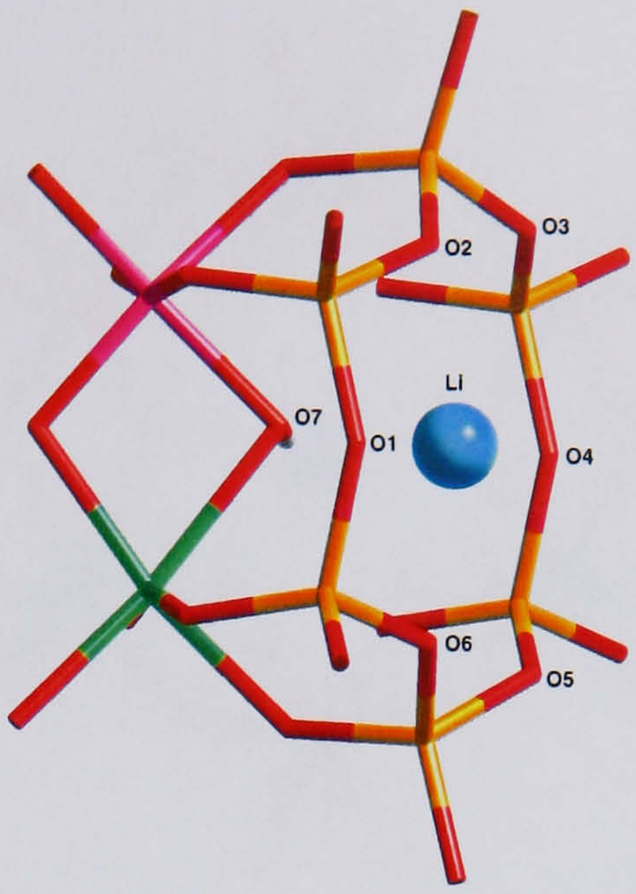

Figure 5.3: Fragment showing the coordination of a lithium cation by oxygen when it is situated in a ditrigonal cavity of the tetrahedral layer. The colour scheme here is white for hydrogen, blue for lithium, red for oxygen, green for magnesium, pink for aluminium and yellow for silicon.

Figures 5.3 and 5.4 show the coordination of lithium by oxygen in the Li-tetra and Li-octa models, respectively. Associated Li–O distances are given in Table 5.4. In the Li-tetra model the lithium cation is essentially three-co-ordinate, bonding to O2 and O6 of the hexagonal ring and O7, the hydroxyl oxygen at the bottom of the ditrigonal cavity. In the case of the Li-octa model coordination is, as expected, octahedral type. The average Li–O bond length is 2.165 Å. This compares quite well with 2.130 Å, the average Li–O bond length for a $[Li(H_2O)_6]^+$ cluster, calculated using second-order Møller-Plesset perturbation theory and a 6-31+G(d) basis set.[166] In both instances the shortest Li–O bonds are those made between the lithium cation and hydroxyl oxygen atom.

These results all indicate that migration of lithium ions into vacant octahedral sites does indeed occur, albeit without providing a pathway. The total energy of the optimised deprotonated Li-octa model was 80.1 kJ mol^{-1} lower than that of the Li-tetra model. In addition, the total energy of the optimised dehydroxylated Li-octa model being 32.8 kJ mol^{-1} lower than that of the Li-tetra model.

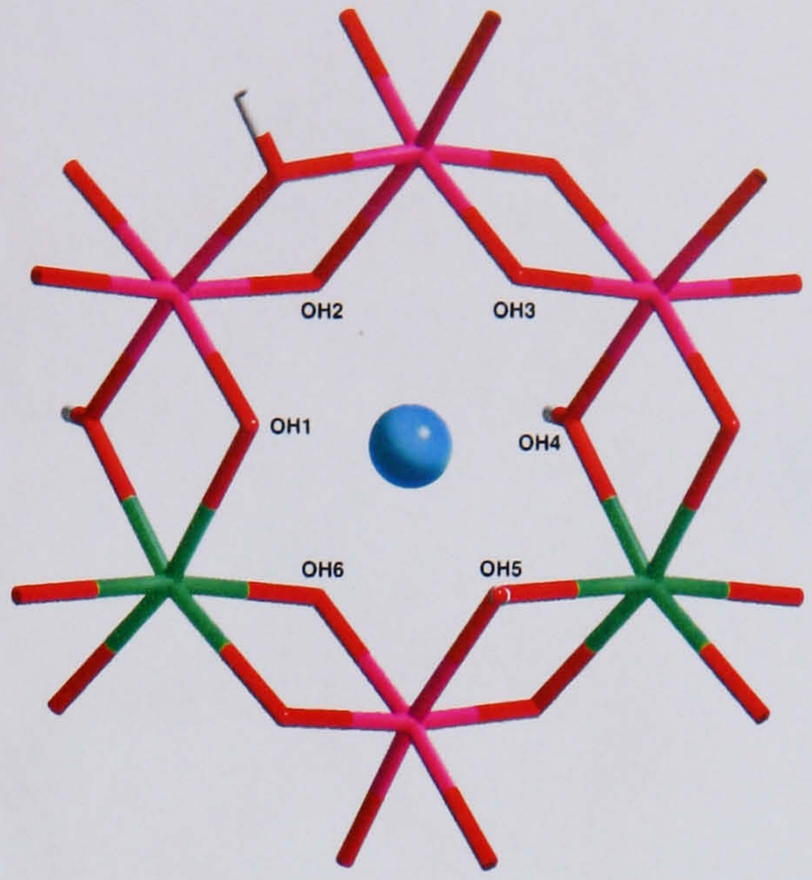

Figure 5.4: Fragment showing the coordination of a lithium cation by oxygen when it is situated in an octahedral site. The colour scheme here is white for hydrogen, blue for lithium, red for oxygen, green for magnesium, pink for aluminium and yellow for silicon.

The geometry of the optimised deprotonated models for the most part resembled their parent structures shown in Figure 5.2, simply with a proton removed. The most notable change occurred in the deprotonated Li-tetra model, where a decrease was observed in the lithium-oxygen distance, for that oxygen from which the proton had been removed. The deprotonated Li-tetra model exhibited a value of 1.786 Å, compared to a figure of 1.976 Å for the parent model. The lithium ion associated very strongly with the residual oxygen.

Muller *et al.* suggest that upon dehydroxylation, *cis* and *trans*-vacant montmorillonite form the same *trans*-vacant layer structure where the residual oxygen atoms locate themselves within the plane of the octahedral aluminium ions, which provide homogenous local charge compensation.[132] The formation of the *trans*-vacant dehydroxylated structure from *cis*-vacant montmorillonite is purported to occur in two stages: initially dehydroxylation occurs and the residual oxygen atoms move within the octahedral plane, after which the octahedral aluminium cations migrate to form a *trans*-vacant state, which brings about the stabilisation of the arrangement.

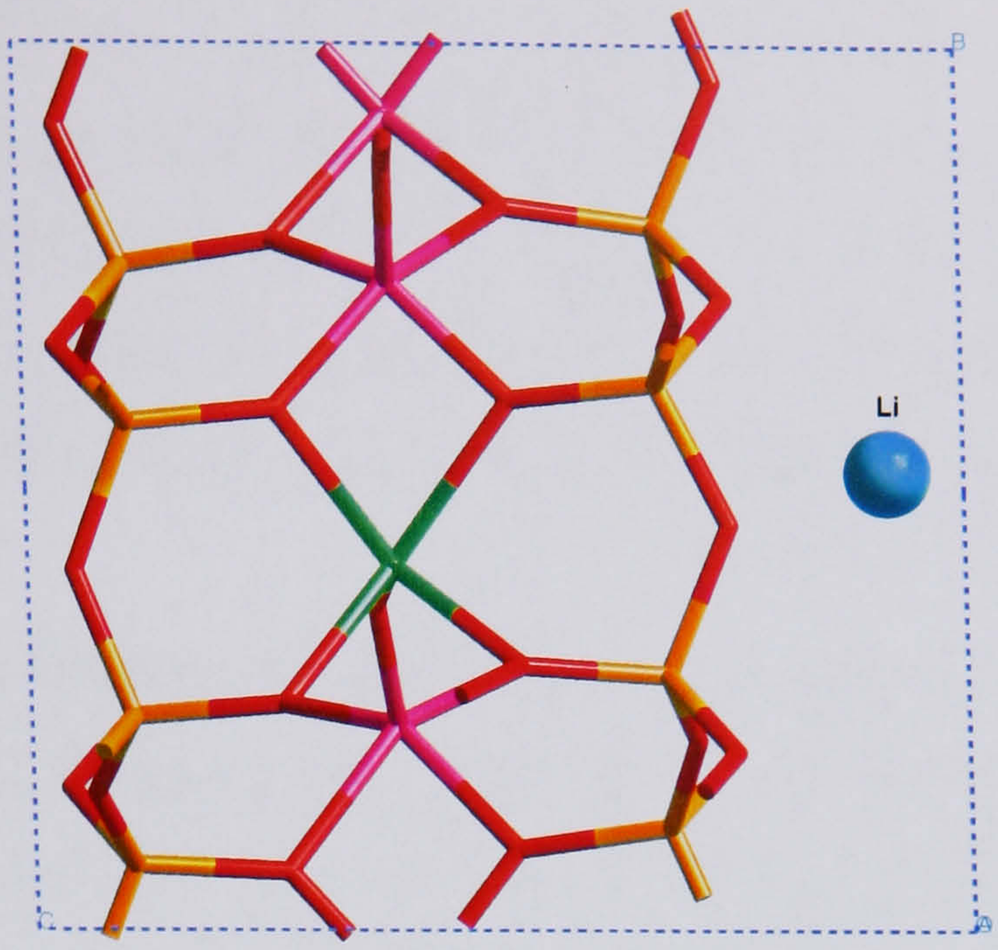

Figure 5.5: *Trans*-vacant dehydroxylated structure formed upon optimisation of the fully dehydroxylated lithium montmorillonite model. During rearrangement the cation moves from the ditrigonal cavity of the tetrahedral layer to the interlayer. The colour scheme here is white for hydrogen, blue for lithium, red for oxygen, green for magnesium, pink for aluminium and yellow for silicon. Periodic boundaries are indicated by the blue dashed lines.

In the optimised dehydroxylated Li-tetra model, the lithium cation associated with the residual oxygen, which showed no movement into the octahedral layer. Similarly no movement of the residual oxygen into the octahedral plane was observed for the Li-octa model. However, further investigation showed that when the Li-tetra model was fully dehydroxylated before energy-minimisation, it did indeed rearrange to form a *trans*-vacant dehydroxylated structure, shown in Figure 5.5. Movement of the residual oxygen atoms into the plane of the octahedral aluminium ions occurs concurrently with and is dependent on the migration of the octahedral ions.

It is interesting to note that the movement of the residual oxygen atoms within the plane of the octahedral ions yields a much less sterically hindered pathway for lithium to migrate to vacant sites in the octahedral layer. However, no migration was observed during optimisation of the dehydroxylated models. In fact, the opposite

was observed. The lithium cation moved out of the ditrigonal cavity and out into the interlayer. This is probably because the negative charge of the residual oxygen is shielded between the octahedral ions so that the driving force for the lithium cation to enter the ditrigonal cavity is removed. These observations indicate that dehydroxylation inhibits rather than aids the migration of lithium cations into the octahedral layer.

Though lithium migration was not observed during the geometry optimisation of the Li-tetra model, we again note that this is a 0K calculation, where thermal energy is not considered. In order to be able to take into account the thermal energy available when the lithium montmorillonite is heated to 300 °C, molecular dynamics were performed, as described in the following sub-section.

5.2.2 Molecular Dynamics

Molecular dynamics simulations were performed for the Li-tetra and Li-octa models. These showed the systems to be stable towards deprotonation and dehydroxylation at 300 K and 573 K, at least on the achieved timescales. Migration of the lithium cation into a vacant octahedral site was not observed for the Li-tetra model at either temperature—perhaps due to the very short simulation time. The constraint that cell parameters must remain fixed during the molecular dynamics may also have restricted the movement of atoms. Indeed, geometry optimisation calculations, discussed in Section 5.2.1, showed that the unit cell a and b parameters increase in order to accommodate a lithium cation in the octahedral layer.

Figure 5.1 shows a snapshot from the molecular dynamics simulation of the hydrated lithium montmorillonite model at 300 K. The Li–O radial distribution function for the interlayer water is shown in Figure 5.6 and is good agreement with that calculated by Chang *et al.* from classical molecular dynamics investigations.[145] both exhibiting a main peak at 2.00 Å. The lithium counterion was observed to be mainly hydrated by four water molecules. with short intervals when this reduced

to three. This is in good accord with classical simulations of Sposito *et al.*[147] The lithium cation did not, however, venture into a ditrigonal cavity at any point during the simulation or even approach close, probably due to its hydration sphere.

The most useful observations emanating from these simulations concerned the orientation of the hydroxyl groups in the Li-octa model. In Section 5.2.1, it was described how geometry optimisation calculations showed that migration of the lithium cation into an octahedral site causes orientation of neighbouring hydroxyl groups approximately 90 ° to the *ab* plane. The molecular dynamics simulations showed that even at finite temperature the same hydroxyl groups fluctuated little from this angle.

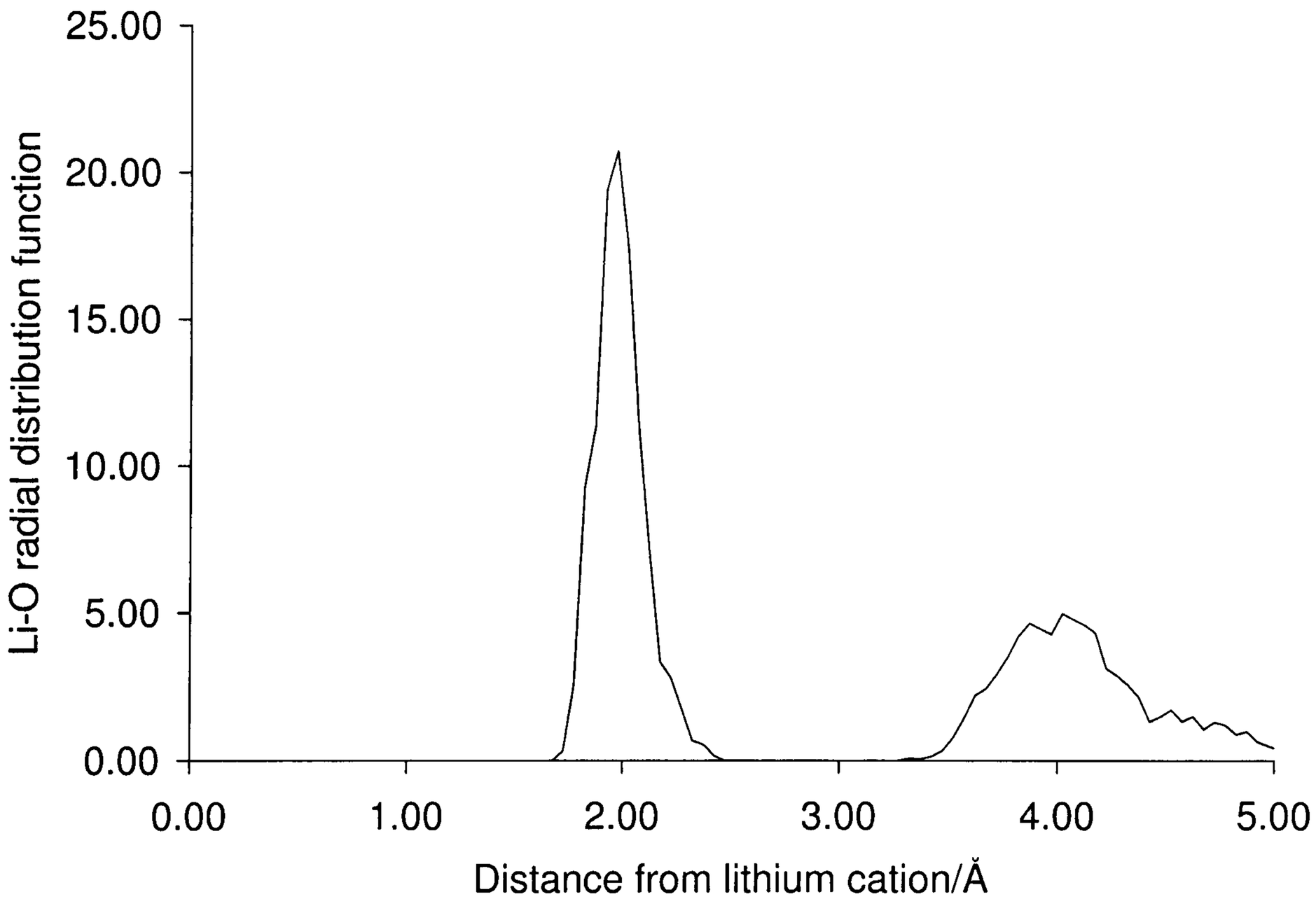

Figure 5.6: Li–O radial distribution function for the interlayer water of the hydrated lithium montmorillonite model, evaluated over the final 2ps of molecular dynamics at 300K.

5.2.3 Power Spectra

When employing *ab initio* techniques to calculate vibrational spectra it has been usual to employ a second derivative based method and study cluster models.[78,92] The problem with cluster models is that they are unable to take into account the existence of hydrogen bonding between hydroxyl-hydrogens and apical oxygen atoms of the tetrahedral sheet, which causes calculated hydroxyl stretching frequencies to be lower than expected.[78] More recent investigations have therefore taken a different route and calculated power spectra from the Fourier transformation of the velocity autocorrelation function (VACF) obtained from the trajectories of relatively short (1ps) molecular dynamics simulations of a periodic model.[94,100,101] This technique is discussed in detail by Kleinhesselink and Wolfsberg who recommend the use of long trajectories coupled with truncation of the VACF prior to its Fourier transform, in such a way that the tail of the VACF is disregarded.[103]

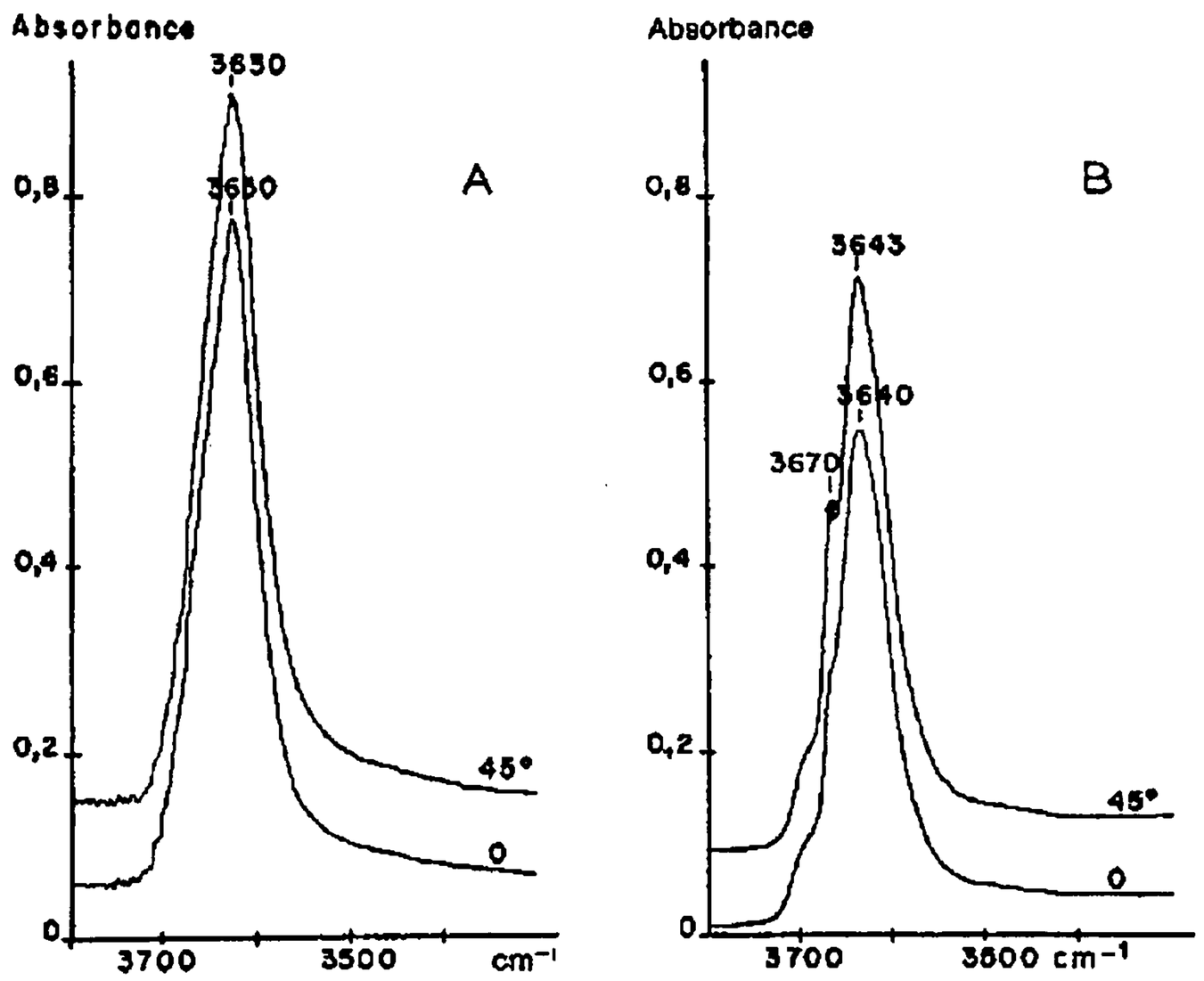

Figure 5.7: Experimental stretching vibrations of structural hydroxyl groups of lithium montmorillonite; (A) unheated; (B) heated at 220 °C for 24 h. Dichroic properties are observed by tilting the film in the incident beam from 0 to 45 °. Reproduced from Calvet and Prost[157] with permission.

Truncation is employed to smooth the power spectra by excluding statistical noise in the tail of the VACF. It has been shown to have little effect on the position of band maxima in power spectra, though it has a noticeable affect on band-width.[103] In our work the calculated VACFs were truncated at 0.4ps before Fourier transformation—this was the approximate value at which all the VACFs decayed to a minimum level. If truncation was omitted the spectra showed bands with multiplet type structure.

More preferable to truncation would have been ensemble-averaging by computing multiple trajectories. This however, was impossible because of the computational expense involved. Experimentation with simulation times showed that if a VACF was calculated using just 1 ps of a trajectory (ignoring the first 0.5 ps) and then using 2 ps, differences of up to 30 cm^{-1} were observed in band maxima. This indicated the necessity of long trajectories for quantitatively reliable results. Of course, this was inhibited by computational cost.

Before analysing the calculated spectra it is useful to review the changes in the experimental infrared spectrum of lithium montmorillonite upon thermal treatment. Figure 5.7 shows the experimental infrared spectra recorded by Calvet and Prost.[157] Prior to thermal treatment the O–H stretching region of the infrared spectrum exhibits just a single, non-dichroic band at 3630 cm^{-1}, but after heating several new bands are observed: a dichroic band at 3670 cm^{-1} assigned to an AlMgLiOH configuration; a second dichroic band at slightly lower frequency attributed to an AlAlLiOH arrangement; and a shoulder at 3700 cm^{-1} due to MgMgLiOH. (Here the three metal ions indicate the trioctahedral arrangement to which a hydroxyl group is bonded.) Similar observations have been reported by other authors.[154,156,159,161] We also note that in montmorillonites which exhibit an unusually high degree of substitution in the tetrahedral layer there is no observed change.[161]

The power spectrum calculated for the hydrated model is shown in Figure 5.8(a). It shows a group of O–H stretching bands centred around 3880 cm^{-1}. Hydroxyls OH2 and OH3 still show some multiplet structure, an artefact of the short trajectory. One would not expect the calculated spectrum to exhibit an identical profile to

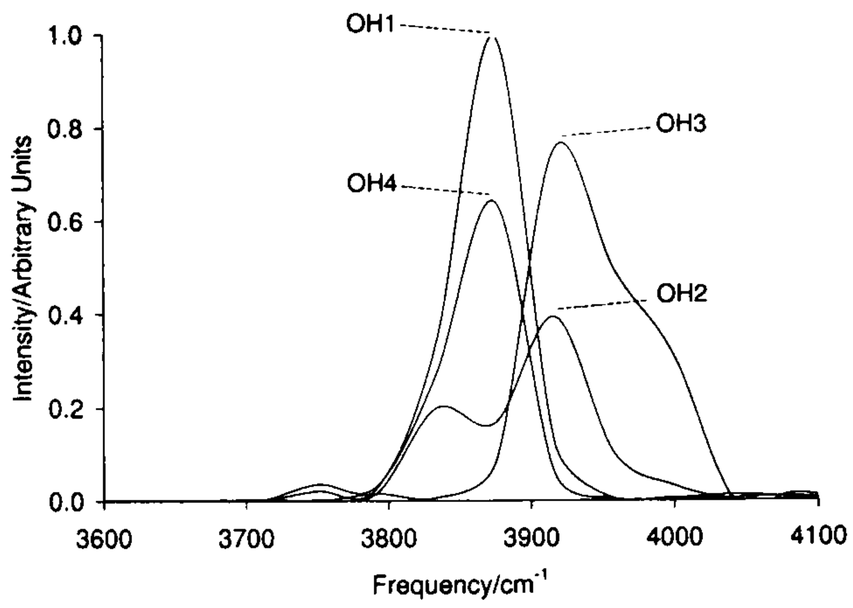

(a) Lithium montmorillonite with cation hydrated in the interlayer. Hydroxyl labels refer to Figure 5.1

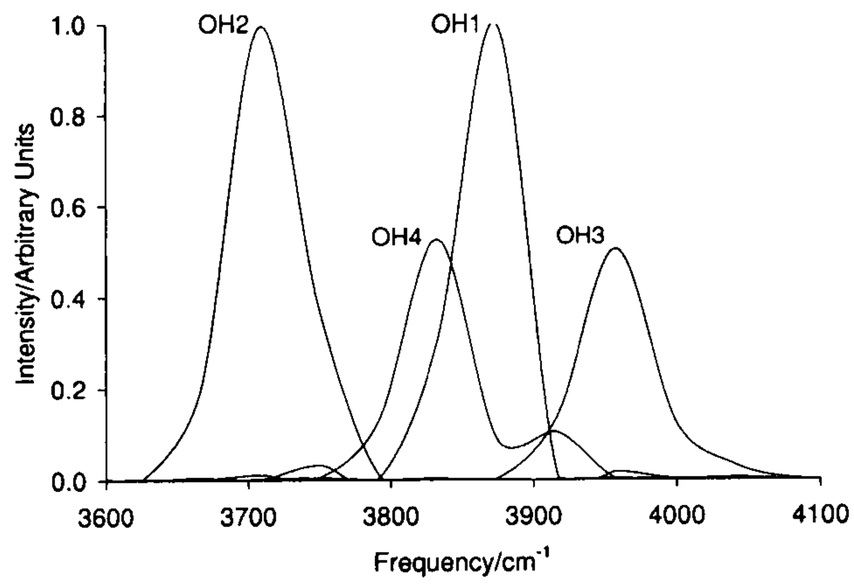

(b) Lithium montmorillonite with cation located in a ditrigonal cavity of the tetrahedral layer. Hydroxyl labels refer to Figure 5.2(a).

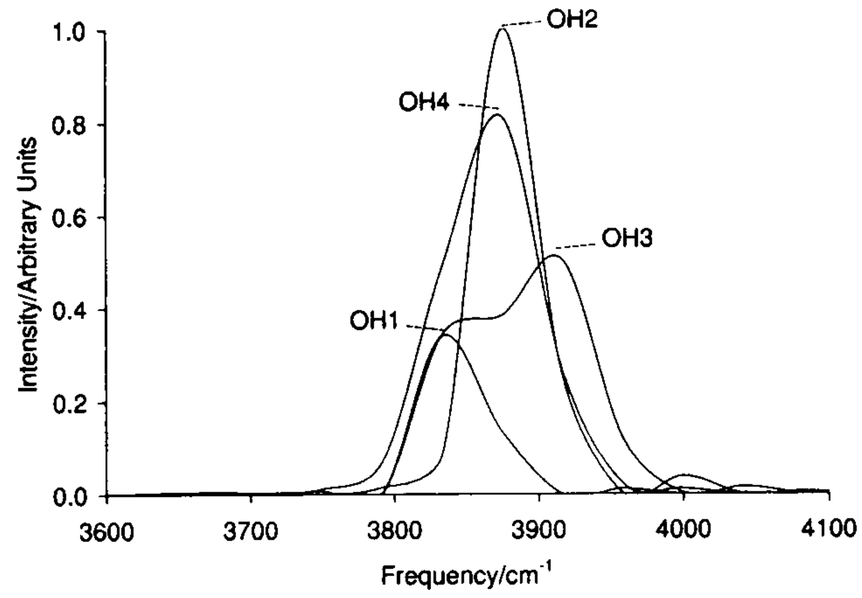

(c) Lithium montmorillonite with cation located in an octahedral site. Hydroxyl labels refer to Figure 5.2(b).

Figure 5.8: Calculated power spectra for the lithium montmorillonite models.

that produced by experiment. Experimental vibrational spectra show the sum of the vibrational frequencies of a vast number of hydroxyl groups, in a large number of different local environments, whereas the calculated power spectrum displays the individual frequencies of four such groups, in a few selected coordination states. Even when experimental vibrational frequencies may be assigned explicitly, calculated frequencies are not normally expected to be in good quantitative agreement. For *ab initio* second derivatives methods it is customary to multiply frequencies by a scaling factor, in order to improve agreement with experimental results.[167-170] However, no similar scaling factor exists for frequencies calculated from the Fourier transformation of autocorrelation functions. The advantage of calculated spectra is that one is able to observe the vibrational frequency of an individual hydroxyl group and investigate the effect of varying its local environment. As such, this spectrum will be used as a reference to calculate relative shifts due to the migration of the lithium cation into the tetrahedral and octahedral layer.

The power spectrum calculated for the Li-tetra model is shown in Figure 5.8(b). Calculated stretching frequencies for OH1, OH2, OH3 and OH4 are approximately 3875 cm^{-1}, 3710 cm^{-1}, 3960 cm^{-1} and 3830 cm^{-1}, respectively. These correlate well with the corresponding hydroxyl bond lengths listed in Table 5.2. In fact, previous theoretical investigations of clay minerals have shown an approximate linear relationship between calculated stretching frequency and bond length, for structural hydroxyl groups.[94,100,101] The frequencies of OH1 and OH4 lie in the same range as the hydroxyl stretching band observed for the hydrated model, while that of OH2, which interacts directly with the lithium cation is much lower and that of OH3, much higher. Though the band due to OH3 could possibly be assigned to the shoulder at higher frequencies, that associated with OH2 at lower frequencies is not observed experimentally for any type of montmorillonite. The disagreement with spectra for montmorillonites where tetrahedral charge is low is unsurprising since we expect the cations to be in octahedral sites. It is more interesting that the spectrum is also in disagreement with those reported for montmorillonites with a

high degree of substitution in the tetrahedral layer, where the lithium cations are thought to be present in the ditrigonal cavities.[161] A possible explanation is that in these types of clay the lithium cations associate so strongly with the tetrahedral aluminium that they are unable to penetrate deep enough into the ditrigonal cavities to interfere with structural hydroxyl groups. Hence there is little change observed in the infrared spectrum upon heating.

The power spectrum calculated for the Li-octa model is shown in Figure 5.8(c). Calculated stretching frequencies for OH1, OH2, OH3 and OH4 are approximately 3840 cm^{-1}, 3870 cm^{-1}, 3875 cm^{-1} and (3850 cm^{-1} and 3910 cm^{-1}). These correlate well with the corresponding hydroxyl bond lengths listed in Table 5.2. as above. Together they form a band centred around 3880 cm^{-1}, the same position as that observed for the hydrated model. There is no indication of a new band/shoulder at higher frequency. In fact, compared with the spectrum of the hydrated model the bands associated with OH2 and OH3 occur at lower frequencies. However, overall the calculated spectrum for the Li-octa model is in much better agreement with that observed experimentally for thermally treated lithium montmorillonite than that of the Li-tetra model. This implies that lithium cations normally migrate to vacant octahedral sites in clay minerals with a low degree of substitution in the tetrahedral layer.

It is impossible to conclusively confirm experimental assignments. The short length of the dynamics trajectories limits the accuracy of the calculated spectra to such an extent that it is impossible to resolve the smaller band shifts reported from experiment.

5.3 Conclusions

In montmorillonite, the migration of lithium cations into vacant octahedral sites causes structural hydroxyl groups to reorientate perpendicular to the *ab*-plane. It is energetically preferable for lithium cations to reside in octahedral sites rather than

ditrigonal cavities, due to the closer proximity of the lithium cations to negative charge sites in the octahedral layer, increasing favourable coulombic interactions. Dehydroxylation inhibits migration of lithium cations to vacant octahedral sites. Comparison of calculated power spectra with those from experiment indicates that lithium cations migrate to octahedral sites when no isomorphic substitution is present in the tetrahedral layer.

Chapter 6

Montmorillonite Dehydroxylation

The effect of thermal treatment on 2:1, dioctahedral clay minerals has been studied much by experimental methods.[171–173] These investigations have shown that three distinct behavioural phases are observed as the temperature is increased: (i) between 20-500 °C dehydration occurs—with increasing temperature water on the external surface, interlayer water hydrogen-bonded to the clay mineral layers and interlayer water associated with metal counterions is lost; (ii) between 500-800°C dehydroxylation occurs—structural hydroxyl groups react together and are lost as water; and (iii) between 800-1500 °C amorphisation occurs—the dehydroxylated clay mineral structure decomposes into an amorphous phase. Temperature ranges vary with type of clay mineral.

Of the three phases, dehydroxylation is both the most interesting and least well understood. Though some authors have studied the dehydroxylation behaviour of a number of clay minerals,[131,132] the majority have focused on pyrophyllite[173–176] and montmorillonite.[163,171,172,177–185] In general, differential thermal analysis (DTA) or thermogravimetric analysis (TGA) has been used to monitor water loss during dehydroxylation and infrared spectroscopy (IR) and X-ray diffraction (XRD) to follow structural changes in the clay minerals. In addition, some investigations have employed magic-angle-spinning nuclear magnetic resonance (MAS-NMR)[174–177] spectroscopic techniques to observe changes in ^{27}Al and ^{29}Si environments.

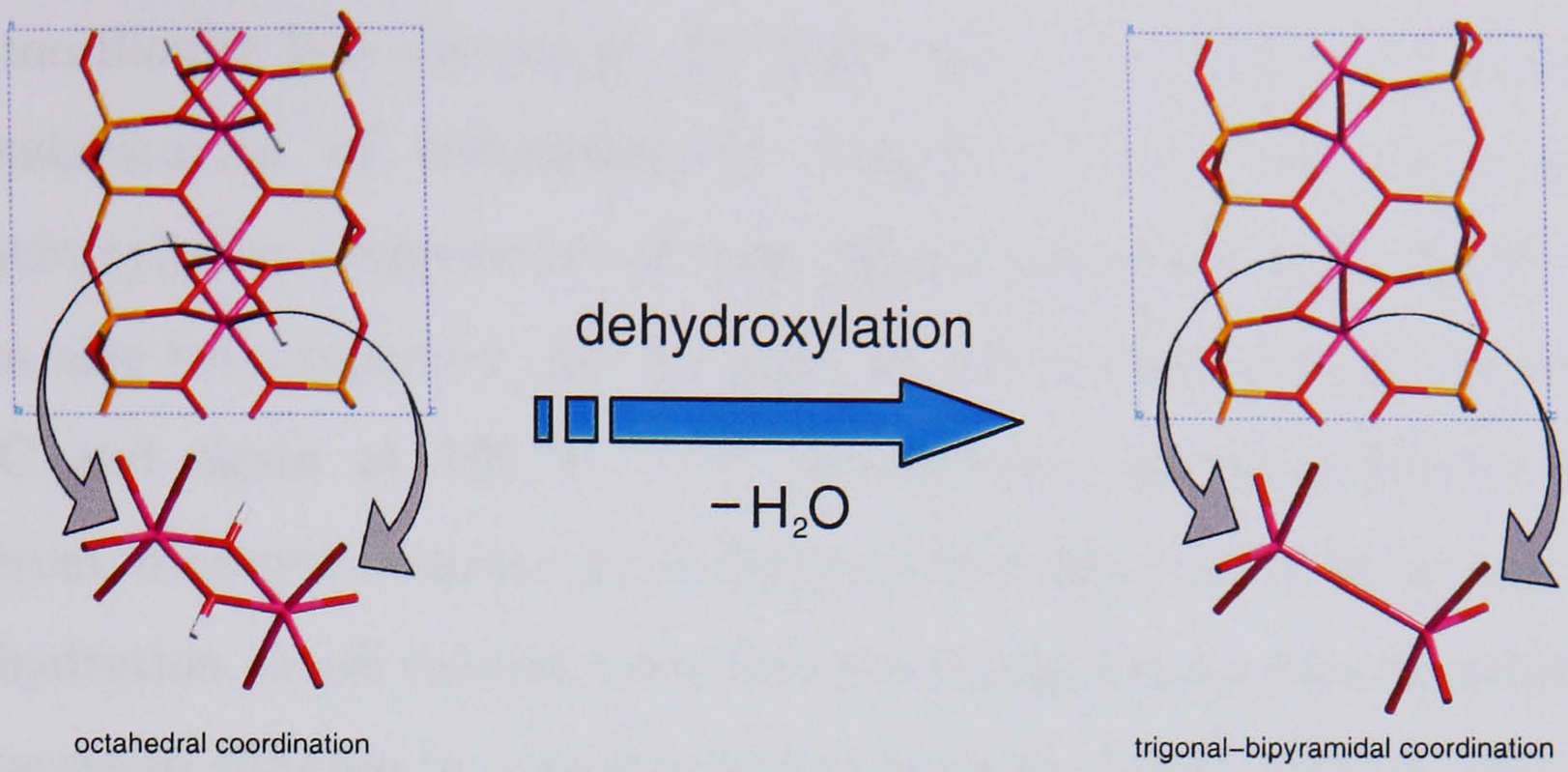

Figure 6.1: The dehydroxylation of pyrophyllite—adjacent hydroxyl groups react to form water and a residual oxygen atom, which locates itself in the plane of the aluminium atoms, where it experiences homogeneous charge compensation. The colour scheme here is white for hydrogen, red for oxygen, pink for aluminium and yellow for silicon. Periodic boundaries are indicated by the blue dashed lines.

Pyrophyllite is a *trans*-vacant, 2:1 layer type, clay mineral, characterised by no isomorphic substitution in either the octahedral or tetrahedral layer. It exhibits a dehydroxylation temperature of approximately 550 °C.[176] Prior to thermal treatment, ^{27}Al MAS-NMR analysis shows a single sharp resonance due to aluminium in octahedral coordination, which disappears upon dehydroxylation as a more complex pattern assigned to aluminium in distorted trigonal-bipyramidal coordination emerges.[175,176] ^{29}Si MAS-NMR analysis indicates that the silicate sheet layer structure is maintained upon dehydroxylation.[174,176] These observations have led to the postulation of a simple dehydroxylation mechanism for pyrophyllite—adjacent hydroxyl groups react to form water and a residual oxygen atom located in the plane of the aluminium atoms, where it experiences homogeneous charge compensation, Figure 6.1. This mechanism has recently been questioned by an infrared study, which reports evidence for a more complex two-stage process.[173] The authors conjectured that the process of pyrophyllite dehydroxylation is in fact a combination of dehydroxylation and rehydroxylation.

Montmorillonite is a *cis*-vacant, 2:1 layer type, clay mineral characterised by partial substitution of aluminium by magnesium in the octahedral layer. The dehydroxylation temperature of most montmorillonites is about 700 °C,[131,132] but it has also been reported that for some dehydroxylation occurs in two stages, at 550 °C and again at 700 °C.[171,172] In addition, montmorillonites saturated with different interlayer cations exhibit different dehydroxylation behaviour.[180,182,185] Upon dehydration, small cations move into the ditrigonal cavities allowing the clay mineral layers to collapse to a greater extent than for larger cations, which remain in the interlayer holding them apart. Therefore with small cations, movement of water during dehydroxylation is diffusion controlled, whereas with larger cations first-order behaviour is observed.[180] The type of interlayer cation is reported to have only a small effect on activation energy of dehydroxylation,[180] with a value of about 250 kJ mol^{-1} calculated for Na^+, K^+ and Ca^{2+} saturated montmorillonites.

The mechanism for the dehydroxylation of montmorillonite is thought to be much more complex than that of pyrophyllite. Prior to thermal treatment ^{27}Al MAS-NMR analysis shows a strong resonance due to aluminium in octahedral coordination and also a second much weaker resonance due to aluminium in tetrahedral coordination; upon dehydroxylation, the former disappears completely, while the latter remains largely unaffected.[177] Though no resonance assignable to five-coordinate aluminium has been observed for dehydroxylated montmorillonite, this is assumed to be due to use of a relatively weak magnetic field,[177] as compared to those employed to analyse dehydroxylation of pyrophyllite,[175,176] rather than its inexistence.

Further insight into the dehydroxylation of montmorillonite has come from study of the rehydroxylated material. It has been shown that it is possible to rehydroxylate montmorillonite subsequent to dehydroxylation.[182–185] Investigations into the effect of thermal treatment on rehydroxylated montmorillonite have demonstrated that it exhibits a dehydroxylation temperature of approximately 550 °C,[132] which is 150 °C lower than that of the original clay mineral, more similar to that of pyrophyllite and other aluminous *trans*-vacant clay minerals.

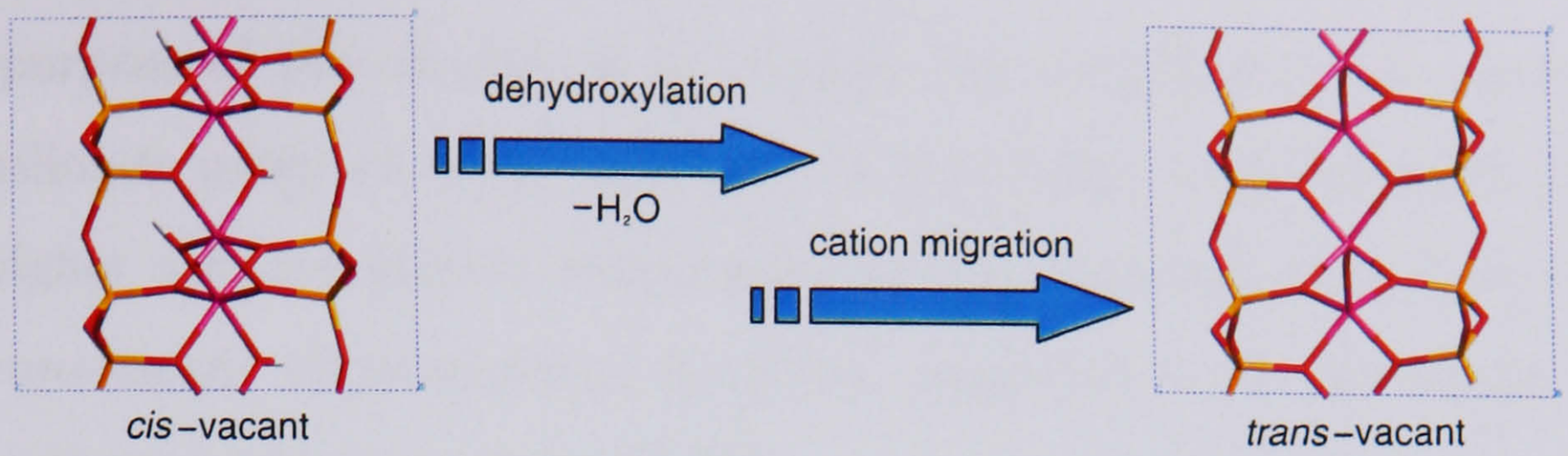

Figure 6.2: The dehydroxylation of montmorillonite is thought to proceed in two separate stages: (i) adjacent hydroxyl groups react to form water and a residual oxygen atom; (ii) aluminium cations in *trans* sites migrate to vacant *cis* sites. In this way the *cis*-vacant clay mineral forms a *trans*-vacant dehydroxylated structure. The colour scheme here is white for hydrogen, red for oxygen, pink for aluminium and yellow for silicon. Periodic boundaries are indicated by the blue dashed lines. Note that no magnesium-for-aluminium substitution is shown here.

In view of this, it has been postulated that upon dehydroxylation *cis*-vacant montmorillonite forms a *trans*-vacant dehydroxylated structure,[131,132] which upon rehydroxylation forms a *trans*-vacant clay mineral, resembling pyrophyllite. This is corroborated by observations from X-ray diffraction studies of the dehydroxylation of other aluminous *cis*-vacant clay minerals,[131,132] which show similar behaviour. The transformation not only explains the lower dehydroxylation temperature of rehydroxylated montmorillonite, but also provides a rational for the fact that some montmorillonites exhibit two different dehydroxylation temperatures—thought to comprise both *cis* and *trans*-vacant layers.

The mechanism of dehydroxylation of montmorillonite is therefore suggested to proceed in two stages.[131,132] In the first stage adjacent hydroxyl groups react to form water and a residual oxygen atom. The initial dehydroxylated structure is, however, calculated to be unstable, due to unrealistically long aluminium-oxygen bonds.[131,132] Stabilisation is brought about by the migration of aluminium cations in *trans* sites to vacant *cis* sites. In this way the *cis*-vacant clay mineral forms a *trans*-vacant dehydroxylated structure, Figure 6.2.

The purpose of this chapter is to examine the dehydroxylation mechanism of montmorillonite using *ab initio* methods. In particular, to understand the reason for the higher dehydroxylation temperature of the *cis*-vacant isomer, as compared to the *trans*-vacant rehydroxylated structure; suggested to be the longer distance between adjacent hydroxyl groups.[131,132]

This chapter is organised as follows. In Section 6.1 we describe the model systems and optimisation methods used. This is followed by a presentation and discussion of the results of the calculations later in Section 6.2, starting with the optimised pyrophyllite structures and moving on to the reaction energy profiles. In Section 6.3 we draw some conclusions.

6.1 Simulation Details

In this section we describe the model systems, methods used to perform the geometry optimisation calculations and geometric constraints applied.

6.1.1 Model Systems

The dehydroxylation-rehydroxylation behaviour of all studied, aluminous, *cis*-vacant clay minerals has been shown to be similar, regardless of the type of isomorphic substitution that they exhibit.[131,132] In addition, it is reported that the activation energy for the dehydroxylation of montmorillonite is predominantly dependent on the type of vacant sites in the octahedral layers and only to a small extent on type of interlayer cations.[180] In view of this, it was decided to study a charge neutral montmorillonite structure without interlayer cations or isomorphic substitution; in effect, a *cis*-vacant pyrophyllite.

The periodic models of *cis* and *trans*-vacant pyrophyllite described in Chapter 4, each with unit cell formula $[Al_2(OH)_2Si_4O_{10}]_2$, were used as the initial models for the optimisation calculations. The small size of the models was again necessitated by the large computational cost associated with *ab initio* calculations.

6.1.2 Geometry Optimisation

Geometry optimisation calculations were carried out using the density functional theory based CPMD code,[186] which utilises periodic boundary conditions and a planewave basis set. The CPMD code is very similar to the CASTEP code used in previous chapters, but allows much more complex geometric constraints to be applied during simulations. The exchange-correlation functional used adhered to the BLYP generalised gradient approximation,[60,65] ionic cores were described by Troullier-Martins norm-conserving pseudopotentials[187] and the energy cut-off for the planewave expansion of the wavefunction was 120 Rydberg. Optimisation of the wavefunction was achieved using the method of direct inversion in the iterative subspace (DIIS),[188] while ionic positions were optimised using the Broyden-Fletcher-Goldfarb-Shanno (BFGS) algorithm[189] and cell parameters by steepest descents.[37]

In the planewave density functional method the number of planewaves required to represent a specified energy cut-off varies proportionally with the volume of the cell. In the CPMD prescription the necessary number of planewaves is calculated prior to optimisation, based on the initial volume of the cell and kept constant throughout. This dictates that any variation in the volume of the cell during optimisation causes the effective energy cut-off to deviate from the desired value; an increase in volume causes it to decrease, leading to a corresponding decrease in precision and vice versa. In order to imitate constant cut-off geometry optimisation, an iterative scheme was adopted in which each cell was repeatedly reoptimised until the change in the volume of the cell upon optimisation was less than 1 $Bohr^3$.

This scheme necessitated the use of a very high energy cut-off, in order to reduce, to an acceptable level, unphysical discontinuities in the total energies of the model systems, associated with the change in the number of planewaves required to expand the wavefunction, at different cell volumes. Preliminary calculations showed that for an energy cut-off of 120 Rydberg, these discontinuities were reduced to approximately 0.25 kJ mol^{-1}, which was considered an acceptable limit.

6.1.3 Geometric Constraints

The *cis* and *trans*-vacant pyrophyllite models were initially optimised with no atom or cell constraints applied. To simulate the process of dehydroxylation they were then reoptimised with a series of different geometric constraints applied.

Two types of dehydroxylation were investigated: (i) *partial dehydroxylation*, in which just one pair of adjacent hydroxyl groups was constrained to react and form a water molecule; (ii) *total dehydroxylation*, in which both pairs of adjacent hydroxyl groups were constrained to react and form water molecules. The periodic nature of the models meant that the former corresponded to the simultaneous reaction of alternate pairs of adjacent hydroxyl groups and the latter to the simultaneous reaction of all pairs of adjacent hydroxyl groups. Though neither is an exact representation of the dehydroxylation process, they were considered the most useful, tractable calculations.

In each case the dehydroxylation process was simulated in two separate stages: (i) *protonation*—protonation of hydroxyl group(s) by adjacent hydroxyl group(s). This was achieved by successive reoptimisation of each model with the distance between the oxygen atom of one hydroxyl group and the proton of the adjacent hydroxyl group constrained at a progressively shorter distance. (ii) *water migration*—migration of water molecule(s) formed by protonation into the interlayer. This was achieved by successive reoptimisation of each model with the distance between the oxygen atom of the water molecule and a dummy atom near the centre of the closest hexagonal ring constrained at a progressively shorter distance. More specific details are listed in Table 6.1. Note that the final model from the protonation stage was used as the initial model for the water migration stage.

In addition, completely dehydroxylated structures were created by removing the water molecules from the *cis* and *trans*-vacant pyrophyllite models that had undergone the process of total dehydroxylation. These were optimised with no atom or cell constraints applied.

Table 6.1: Geometric Constraints Applied to Pyrophyllite Models to Promote their Dehydroxylation

dehydroxylation process	constraint(s) applied[a,b,c]	
partial dehydroxylation of *cis*-vacant pyrophyllite	protonation[d]	water migration
	O9—H2 = 2.700 Å→0.991 Å	D(O20, O21, O22)—O9 = 2.400 Å→0.000 Å; O9—H2 < 1.000 Å
partial dehydroxylation of *trans*-vacant pyrophyllite	protonation[e]	water migration
	O8—H1 = 2.900 Å→1.310 Å	D(O19, O20, O21)—O8 = 1.200 Å→0.000 Å
total dehydroxylation of *cis*-vacant pyrophyllite	protonation[d]	water migration
	O9—H2 = 2.700 Å→0.991 Å	D(O20, O22)—O9 = 2.600 Å→1.000 Å; O9—H2 < 1.000 Å
	O12—H1 = 2.700 Å→0.991 Å	D(O19, O23)—O12 = 2.600 Å→1.000 Å; O12—H1 < 1.000 Å
total dehydroxylation of *trans*-vacant pyrophyllite	protonation[e]	water migration
	O8—H1 = 2.900 Å→1.260 Å	D(O19, O21)—O8 = 1.700 Å→1.000 Å
	O11—H3 = 2.900 Å→1.260 Å	D(O22, O24)—O11 = 1.700 Å→1.000 Å

[a] atom labels refer to Figures 6.3 and 6.4.

[b] X1—X2 = N1→N2 indicates the distance between atoms X1 and X2 was constrained at N1 and progressively lower values until a value of N2 was reached.

[c] D(X1, X2 ...) indicates a dummy atom located at the arithmetic mean of the co-ordinates of atoms X1, X2 ... .

[d] 0.991 Å is the calculated average O—H bond length for liquid water, using a similar density functional method to that used in this work.[190]

[e] in the case of the *trans*-vacant pyrophyllite models protonation was spontaneous once the proton was brought within a certain distance of the oxygen atom.

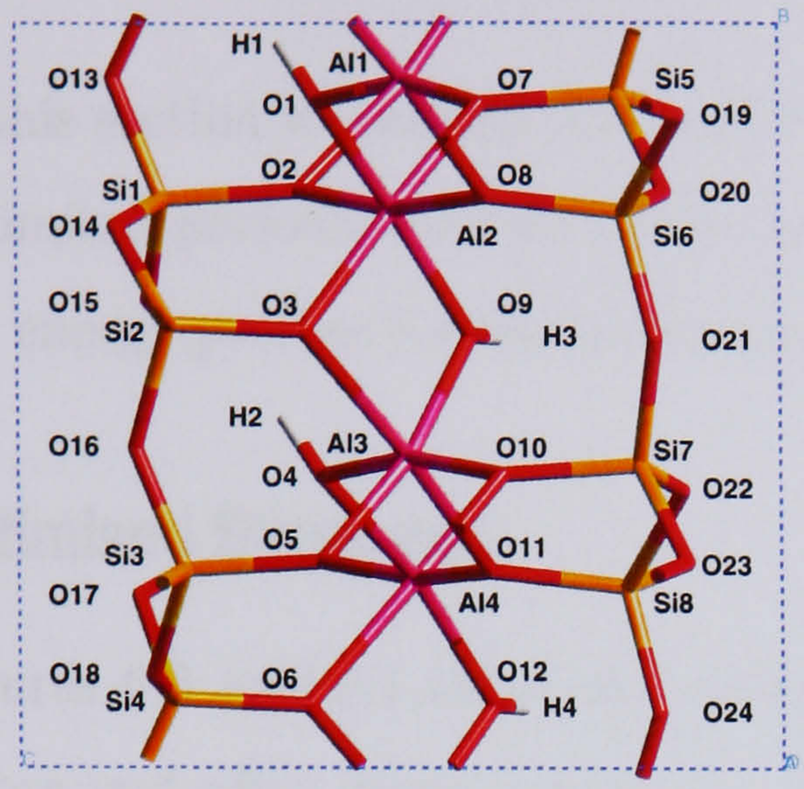

(a) before dehydroxylation

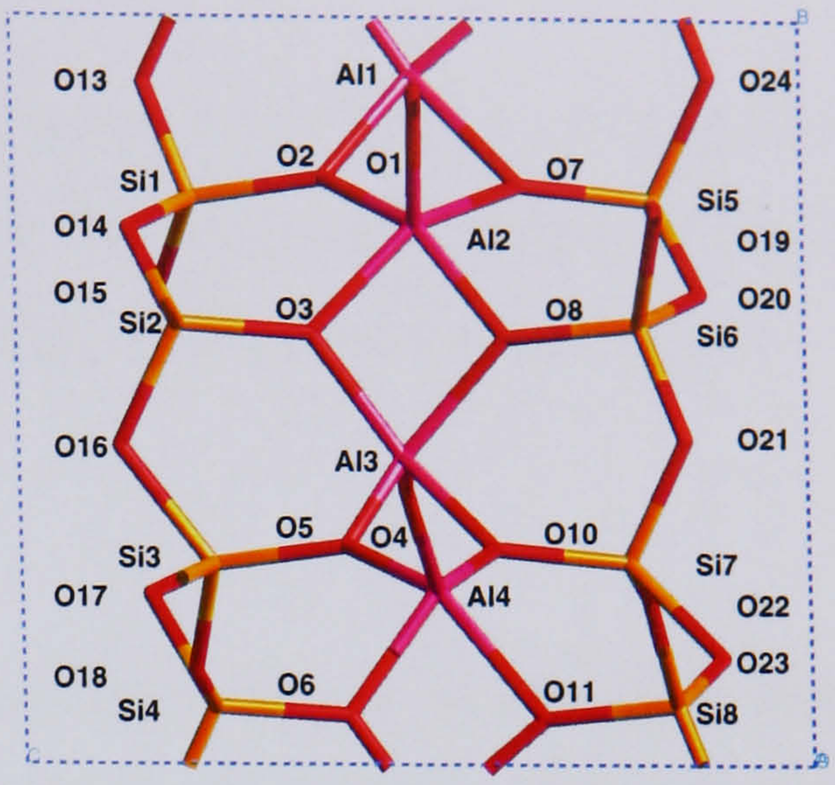

(b) after dehydroxylation

Figure 6.3: Optimised *cis*-vacant pyrophyllite model. The colour scheme here is white for hydrogen, red for oxygen, pink for aluminium and yellow for silicon. Periodic boundaries are indicated by the blue dashed lines.

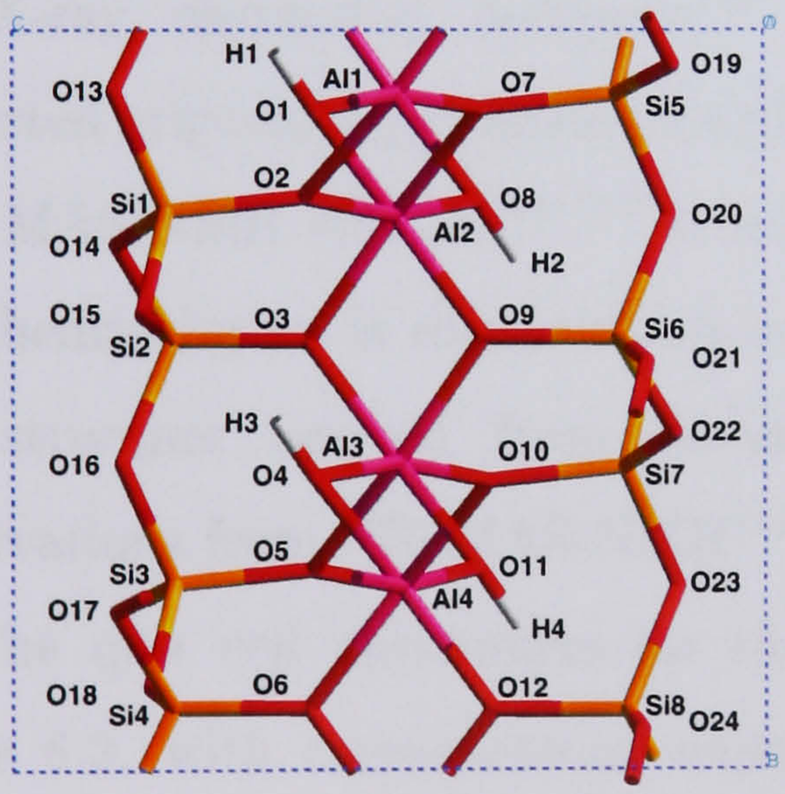

(a) before dehydroxylation

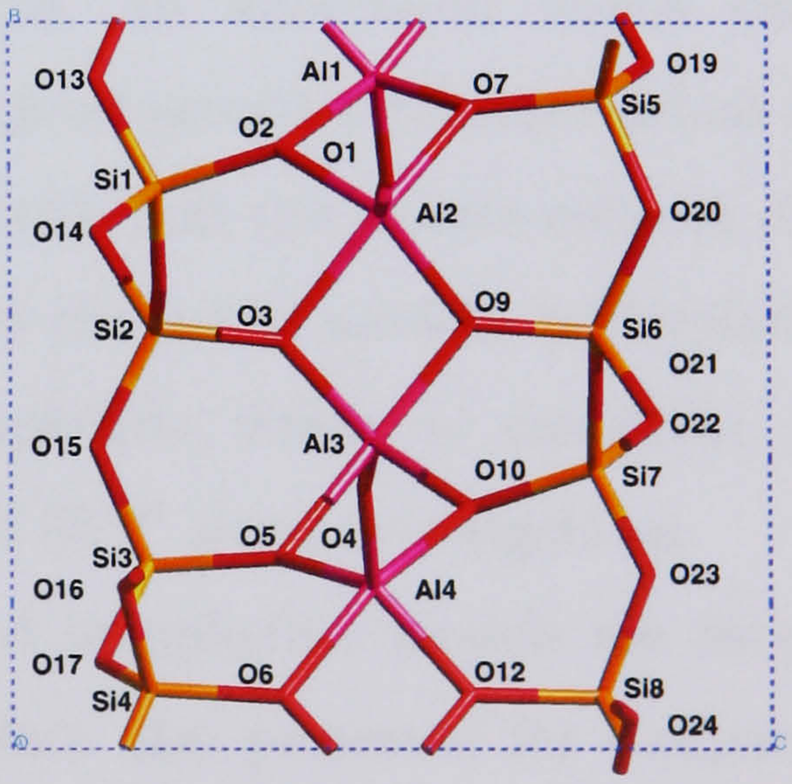

(b) after dehydroxylation

Figure 6.4: Optimised *trans*-vacant pyrophyllite model. The colour scheme here is white for hydrogen, red for oxygen, pink for aluminium and yellow for silicon. Periodic boundaries are indicated by the blue dashed lines..

6.2 Results and Discussion

In this section we discuss the results of our simulations. It begins with details of the optimised periodic *cis* and *trans*-vacant pyrophyllite structures. This is followed by the energy profiles for the partial and total dehydroxylation of both models.

6.2.1 Optimised Structures

Figures 6.3 and 6.4 show the optimised *cis* and *trans*-vacant pyrophyllite models, before and after dehydroxylation. The atom labels are consistent for each isomer, going from before to after dehydroxylation, so that movement of atoms can be traced.

One can see that the *cis* and *trans*-vacant pyrophyllite models both form a similar *trans*-vacant structure upon dehydroxylation, as postulated by Drits *et al.*[131,132] In both dehydroxylated structures the residual oxygen atoms reside within the plane of the aluminium atoms, as proposed by Drits *et al.*[131,132] and in agreement with the crystal structure of dehydroxylated *trans*-vacant pyrophyllite determined by X-ray diffraction methods.[191] In addition, all aluminium atoms exhibit distorted trigonal-bipyramidal coordination in good accord with observations from ^{27}Al MAS-NMR studies.[175–177] It is also noticeable that the silicate network of the tetrahedral layers is distorted, as compared to the initial models, particularly in the structure derived from *cis*-vacant pyrophyllite, which is consistent with observations from ^{29}Si MAS-NMR[173,174,176] and IR[180] based investigations.

The unit cell parameters for the optimised pyrophyllite models are listed in Table 6.2, with corresponding experimental data also presented for comparison. In general, calculated unit cell lengths are slightly longer than experimental values, while angles are in reasonable agreement. The most noticeable change in the calculated unit cell parameters, upon dehydroxylation, is the large increase in b, which is observed experimentally, but to a much lesser extent. The small increase in a observed experimentally is not seen in the calculated values. Such differences are probably due to the small size of the models.

Table 6.2: Unit Cell Parameters of Optimised Pyrophyllite Models; Lengths are in Å and Angles in °

clay structure	a	b	c	α	β	γ
cis-vacant pyrophyllite	5.288	9.232	9.662	89.29	98.65	90.07
cis-vacant montmorillonite (exp.)[132]	5.193	8.994	-	-	-	-
dehydroxylated *cis*-vacant pyrophyllite	5.214	9.427	10.256	87.57	103.51	92.16
dehydroxylated *cis*-vacant montmorillonite (exp.)[132]	5.241	9.078	-	-	-	-
trans-vacant pyrophyllite	5.305	9.261	9.561	90.51	100.37	89.69
trans-vacant pyrophyllite (exp.)[131]	5.161	8.957	9.351	-	100.37	-
dehydroxylated *trans*-vacant pyrophyllite	5.248	9.430	9.972	91.02	101.02	87.73
dehydroxylated *trans*-vacant pyrophyllite (exp.)[131]	5.192	9.122	9.499	-	100.21	-

It has been postulated that the higher dehydroxylation temperature of *cis*-vacant, aluminous, dioctahedral, 2:1 layer-type clay minerals, as compared to similar *trans*-vacant clay minerals, is predominantly due to the longer distance between adjacent hydroxyl groups in the former.[131] This is based on the assumption that the thermal energy required for the proton of one hydroxyl group to transfer to the oxygen atom of an adjacent hydroxyl group is primarily dependent on the distance between the two. It is likely however, that this conclusion was reached on the basis of hydroxyl oxygen atom positions only.

In the optimised *cis*-vacant pyrophyllite model, the average distance between the oxygen atoms of adjacent hydroxyl groups is 2.822 Å, while in the optimised *trans*-vacant pyrophyllite model it is 2.420 Å. This is in agreement with experiment. Note however, that the average distance between the proton of a hydroxyl group and the oxygen atom of an adjacent hydroxyl group is only 2.953 Å in the *cis*-vacant pyrophyllite model, but significantly larger at 3.311 Å, in the *trans*-vacant model. This implies that some factor other than proximity of adjacent hydroxyl groups is responsible for the difference in dehydroxylation temperatures.

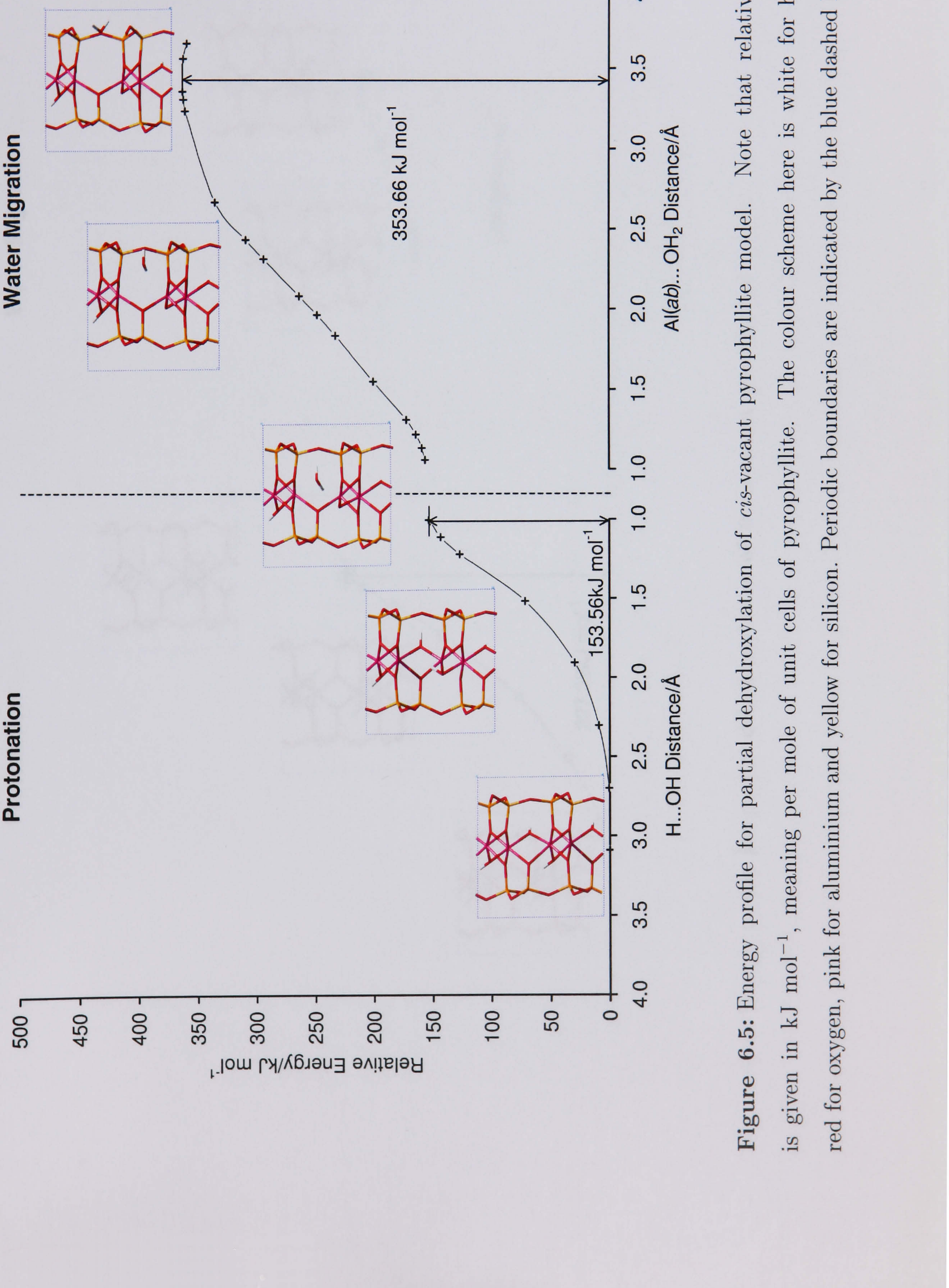

Figure 6.5: Energy profile for partial dehydroxylation of *cis*-vacant pyrophyllite model. Note that relative energy is given in kJ mol^{-1}, meaning per mole of unit cells of pyrophyllite. The colour scheme here is white for hydrogen, red for oxygen, pink for aluminium and yellow for silicon. Periodic boundaries are indicated by the blue dashed lines.

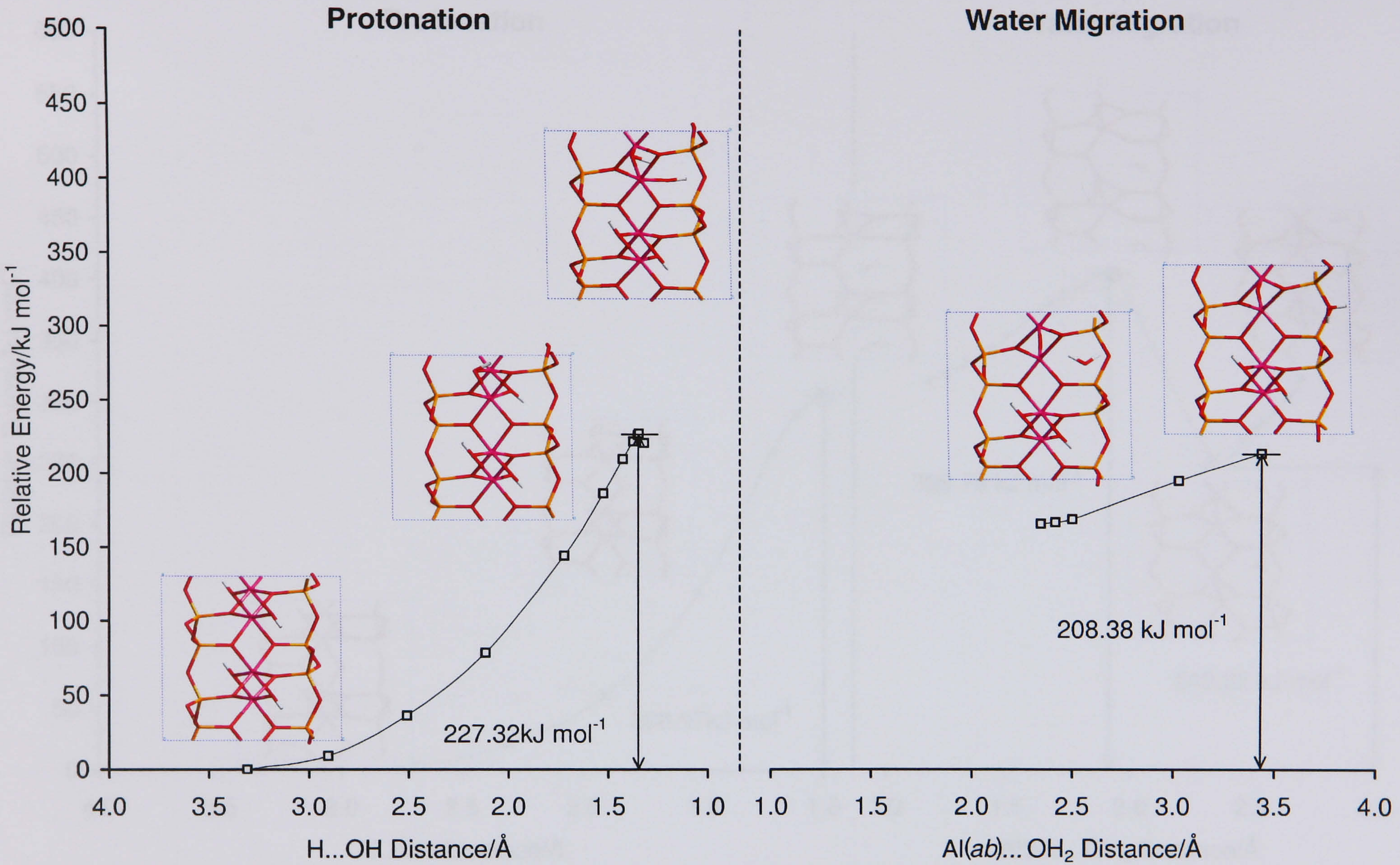

Figure 6.6: Energy profile for partial dehydroxylation of *trans*-vacant pyrophyllite model. Note that relative energy is given in kJ mol^{-1}, meaning per mole of unit cells of pyrophyllite. The colour scheme here is white for hydrogen, red for oxygen, pink for aluminium and yellow for silicon. Periodic boundaries are indicated by the blue dashed lines.

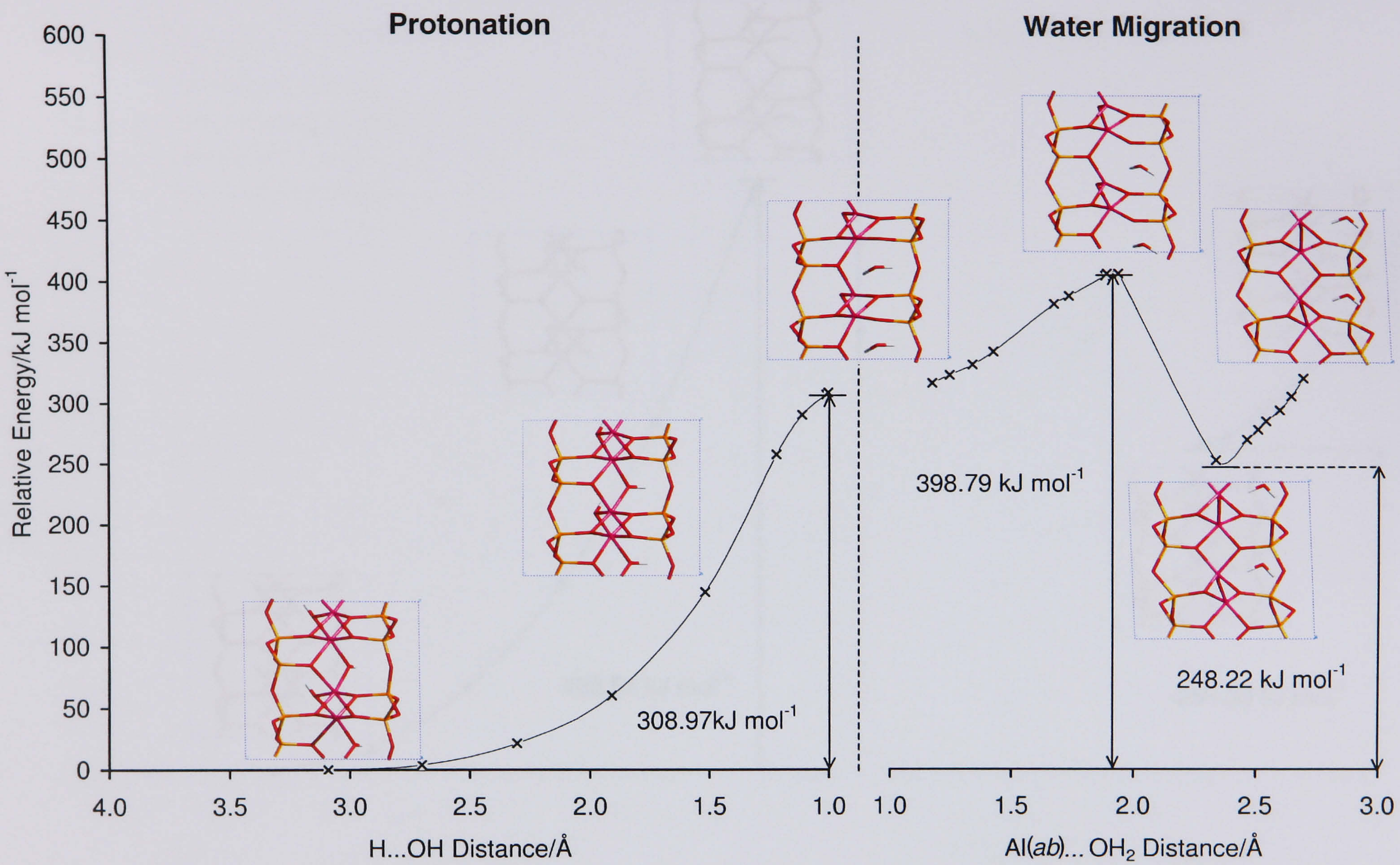

Figure 6.7: Energy profile for total dehydroxylation of *cis*-vacant pyrophyllite model. Note that relative energy is given in kJ mol^{-1}, meaning per mole of unit cells of pyrophyllite. The colour scheme here is white for hydrogen, red for oxygen, pink for aluminium and yellow for silicon. Periodic boundaries are indicated by the blue dashed lines.

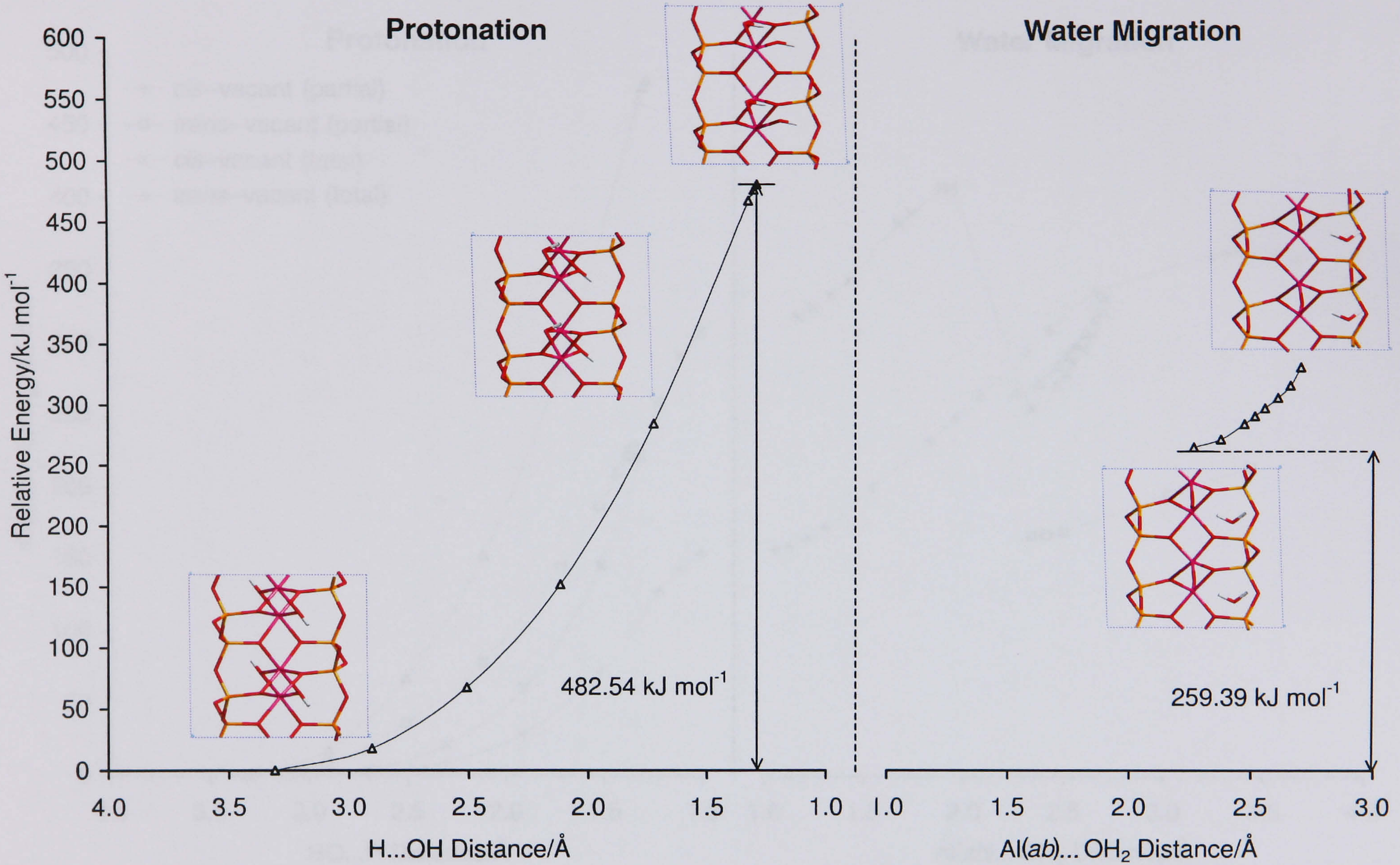

Figure 6.8: Energy profile for total dehydroxylation of *trans*-vacant pyrophyllite model. Note that relative energy is given in kJ mol^{-1}, meaning per mole of unit cells of pyrophyllite. The colour scheme here is white for hydrogen, red for oxygen, pink for aluminium and yellow for silicon. Periodic boundaries are indicated by the blue dashed lines.

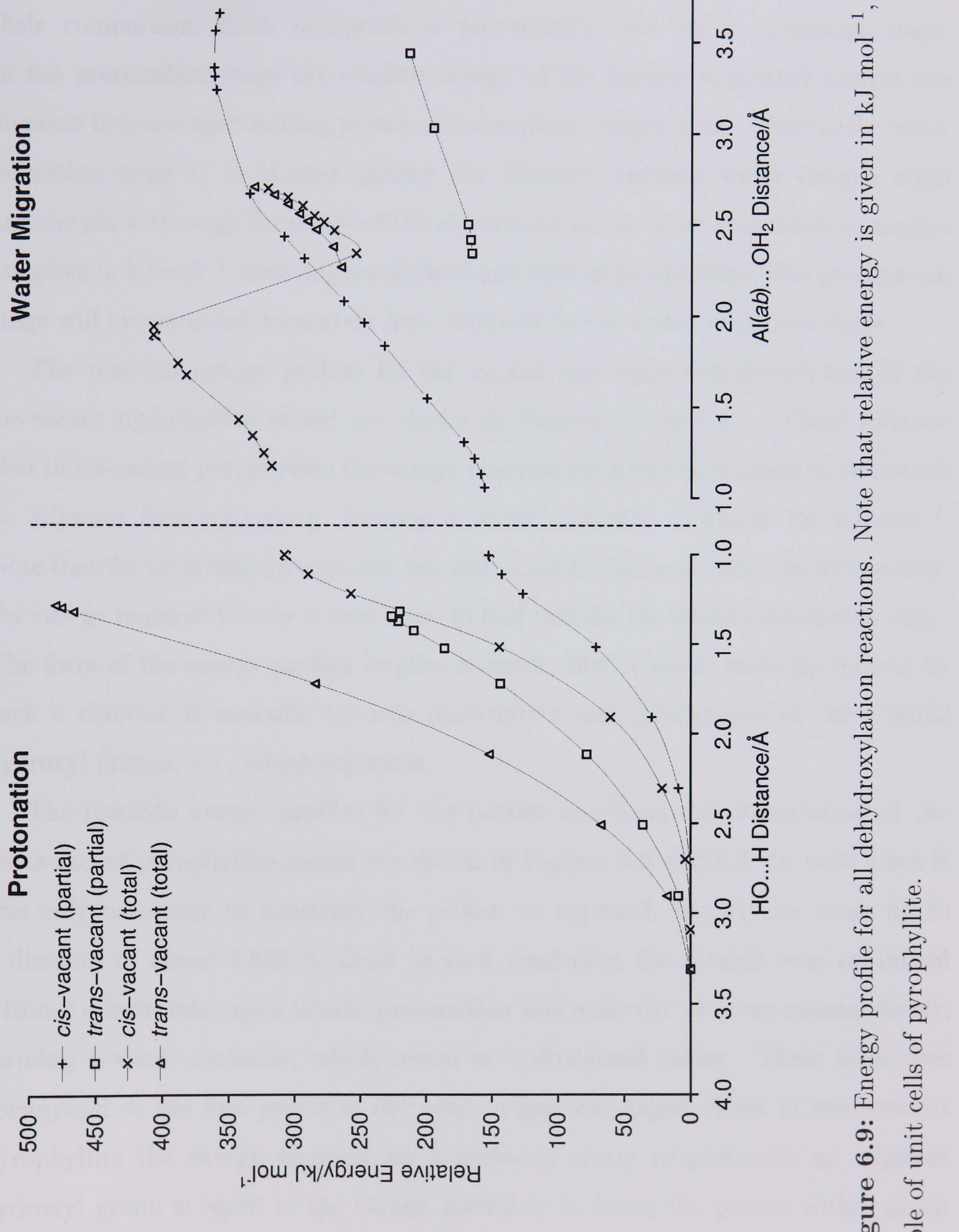

Figure 6.9: Energy profile for all dehydroxylation reactions. Note that relative energy is given in kJ mole^{-1}, meaning per mole of unit cells of pyrophyllite.

6.2.2 Dehydroxylation Reaction Energy Profiles

Figures 6.5, 6.6, 6.7 and 6.8 show the energy profiles for the four dehydroxylation reactions investigated. These are also plotted together in Figure 6.9 in order to aid their comparison. Each comprises a protonation and water migration stage. In the protonation stage the relative energy of the system is plotted against the distance between approaching proton and accepting oxygen atom, while in the water migration stage it is plotted against the distance between water oxygen atom and the plane through the centre of the aluminium atoms. Note that relative energies are given in kJ mol^{-1}, meaning per mole of unit cells of pyrophyllite. The protonation stage will be discussed separately first, followed by the water migration stage.

The reaction energy profiles for the partial and total dehydroxylation of the *cis*-vacant pyrophyllite model are shown in Figures 6.5 and 6.7. These indicate that in *cis*-vacant pyrophyllite the energy required for a hydroxyl group to protonate an adjacent hydroxyl group, forming a water molecule, is about 155 kJ mol^{-1}. Note that for total dehydroxylation two protonation reactions occur simultaneously; the energy required for one is thus equal to half that for the whole protonation stage. The form of the energy profiles implies however, that a water molecule formed by such a reaction is unstable towards dissociation and reformation of the original hydroxyl groups, *i.e.*, rehydroxylation.

The reaction energy profiles for the partial and total dehydroxylation of the *trans*-vacant pyrophyllite model are shown in Figures 6.6 and 6.8. In both cases it was only necessary to constrain the proton to approach the oxygen atom up to a distance of about 1.300 Å. Once in such proximity, the models were optimised without constraints, upon which, protonation was observed to occur spontaneously, forming a water molecule, which rested in a ditrigonal cavity. These structures correspond to the first points in the water migration stages. Thus in *trans*-vacant pyrophyllite the energy required for a hydroxyl group to protonate an adjacent hydroxyl group is equal to the energy necessary to bring the proton within about 1.300 Å of the oxygen atom, shown to be approximately 235 kJ mol^{-1}.

These results indicate that the energy required to enable a hydroxyl group to protonate an adjacent hydroxyl group is much less in *cis*-vacant pyrophyllite, as compared to *trans*-vacant. But also that a water molecule formed by such a reaction in *cis*-vacant pyrophyllite is unstable towards rehydroxylation, while in *trans*-vacant, once formed, a water molecule is relatively stable.

In order to understand these results one must consider the subtle differences in the structures of the isomers. In particular, the fact that in *cis*-vacant pyrophyllite adjacent hydroxyl groups bridge different pairs of aluminium atoms, whereas in *trans*-vacant pyrophyllite they are both bonded to the same pair.

It was noted in the previous section that although the distance between adjacent hydroxyl oxygen atoms is greater in *cis*-vacant pyrophyllite, as compared to *trans*-vacant, the distance between the proton of a hydroxyl group and the oxygen atom of an adjacent hydroxyl group is shorter. It could therefore be postulated that the lesser energy required to bring about protonation in *cis*-vacant pyrophyllite, as compared to *trans*-vacant, is due to the shorter distance the proton must travel. In fact, in both isomers the distance between the proton of a hydroxyl group and the oxygen atom of an adjacent hydroxyl group is too large for the proton to jump across. For protonation to occur, it is necessary for the hydroxyl oxygen atoms to rearrange and the hydroxyl bonds to reorientate, in order to bring them into closer proximity.

In *cis*-vacant pyrophyllite the distance between adjacent hydroxyl oxygen atoms is approximately 2.800 Å, while that between the proton of a hydroxyl group and the oxygen atom of an adjacent hydroxyl group is approximately 2.900 Å. The simulations show that during protonation, adjacent hydroxyl oxygen atoms move to within approximately 2.300 Å. In addition, the hydroxyl bonds reorientate. Consequently at the instant proton transfer begins the distance between the proton and adjacent oxygen atom is approximately 1.200 Å. The important point to note is that the rearrangement of the hydroxyl oxygen atoms and reorientation of the hydroxyl bonds is relatively sterically unhindered, because the hydroxyl groups bridge different pairs of aluminium atoms.

In *trans*-vacant pyrophyllite the distance between adjacent hydroxyl oxygen atoms is approximately 2.400 Å, while that between the proton of a hydroxyl group and the oxygen atom of an adjacent hydroxyl group is approximately 3.300 Å. The simulations show that during protonation, adjacent hydroxyl oxygen atoms move to within approximately 2.200 Å. In addition, the hydroxyl bonds reorientate, with one rotating up to 180°. Consequently at the instant proton transfer begins the distance between the proton and adjacent oxygen atom is approximately 1.300 Å. These rearrangements are however, highly sterically hindered, due to the fact that adjacent hydroxyl groups bridge the same pair of aluminium atoms. This not only constrains the relative movement of the hydroxyl oxygen atoms, but also prescribes that hydroxyl bonds orientate in opposing directions.

In view of this, it is concluded that the lesser energy required to induce protonation in *cis*-vacant pyrophyllite, as compared to *trans*-vacant, is due to the lesser energy necessary for the rearrangement of the hydroxyl oxygen atoms and reorientation of hydroxyl bonds. This being related to the fact that in *cis*-vacant pyrophyllite adjacent hydroxyl groups bridge different pairs of aluminium atoms, whereas in *trans*-vacant pyrophyllite they are both bonded to the same pair.

The same structural difference is also responsible for the different stabilities of water molecules, formed by hydroxyl protonation, in the two isomers. When one hydroxyl group protonates another, a water molecule and residual oxygen atom are formed. It can be seen in the dehydroxylation energy profiles of both isomers, that as protonation proceeds, the residual oxygen atoms move towards the plane of the aluminium atoms, in an attempt to obtain uniform charge compensation.

It is apparent from Figures 6.5 and 6.7 that in *cis*-vacant pyrophyllite residual oxygen atoms are unable to move fully into the plane of the aluminium atoms (unless cation migration occurs.) This is because of an opposing oxygen atom, which bridges the same pair of aluminium atoms, illustrated in Figure 6.10(a). The opposing oxygen atom, as part of the tetrahedral layer, is fixed in position and inhibits movement of the residual oxygen atom between the aluminium atoms.

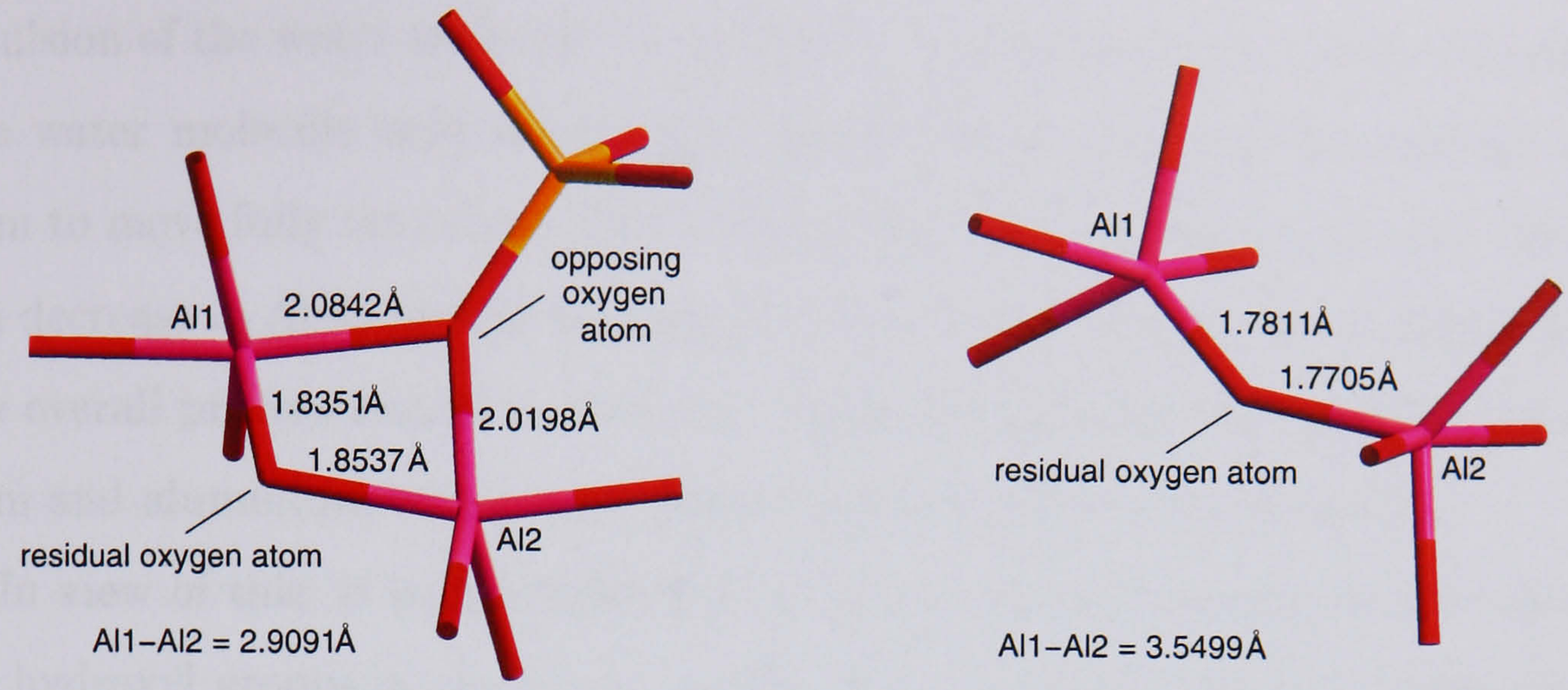

(a) *cis*-vacant pyrophyllite

(b) *trans*-vacant pyrophyllite

Figure 6.10: Fragments from optimised *cis* and *trans*-vacant pyrophyllite models showing the location of residual oxygen atoms immediately after protonation. The colour scheme here is red for oxygen, pink for aluminium and yellow for silicon. Periodic boundaries are indicated by the blue dashed lines.

It is seen in Figures 6.5 and 6.7 that this causes the residual oxygen atom to be insufficiently charge compensated by the aluminium atoms, which makes it extremely susceptible to reprotonation by the associated water molecule. The water molecule is inhibited from moving away, into a ditrigonal cavity, since it must balance the asymmetric charge distribution around the aluminium atoms, generated by the ill-positioned residual oxygen atom. The combination of these factors renders the water molecule unstable towards rehydroxylation.

In contrast, Figures 6.6 and 6.8 show that in *trans*-vacant pyrophyllite residual oxygen atoms are able to move into the centre of the plane of the aluminium atoms. This is due to adjacent hydroxyl groups bridging the same pair of aluminium atoms, which means that the oxygen atom opposing the residual oxygen atom is that of the protonated hydroxyl group, *i.e.*, water molecule, and is relatively free to move. It is seen in Figures 6.6 and 6.8 that in *trans*-vacant pyrophyllite protonation, movement of the residual oxygen atom into the plane of the aluminium atoms and

expulsion of the water molecule formed into a ditrigonal cavity, occurs concurrently. The water molecule moves into a ditrigonal cavity, allowing the residual oxygen atom to move fully into the centre of the plane of the aluminium atoms. This leads to a decrease in Al–O and an increase in Al–Al bond lengths, seen in Figure 6.10(b). The overall process results in uniform charge compensation for the residual oxygen atom and aluminium atoms and consequently a stable water molecule.

In view of this, it is concluded that a water molecule formed by the reaction of two hydroxyl groups in *cis*-vacant pyrophyllite is unstable towards rehydroxylation, because the residual oxygen atom is unable to move fully into the centre of the plane of the aluminium atoms, which results in an unfavourable separation of charge. In *trans*-vacant pyrophyllite however, the residual oxygen atom is able to move into the centre of the plane of the aluminium atoms, leading to homogenous charge compensation and a stable water molecule. These differences originate from the fact that in *cis*-vacant pyrophyllite adjacent hydroxyl groups bridge different pairs of aluminium atoms, whereas in *trans*-vacant pyrophyllite they bridge the same pair.

If we now turn our attention to the water migration stage of the dehydroxylation energy profiles. These show the energetics of the systems as water molecules migrate across the ditrigonal cavity towards the interlayer. It will be seen that this is very different for each of the isomers.

The energy profile for the partial dehydroxylation of *cis*-vacant pyrophyllite is shown in Figure 6.5. It can be seen that it is extremely unfavourable for the water molecule to move across the ditrigonal cavity towards the interlayer. This is due to the fact that as the water molecule migrates it is less able to compensate the asymmetric charge distribution caused by the residual oxygen atom. If one considers the whole profile, it is clear that the water molecule is unstable towards rehydroxylation up until it exits the ditrigonal cavity. The energy barrier to this is in the region of 200 kJ mol^{-1}. If added to the activation energy for protonation, it gives a total activation energy for dehydroxylation of approximately 350 kJ mol^{-1}. Note however, that cation migration does not occur.

The energy profile for the partial dehydroxylation of *trans*-vacant pyrophyllite is shown in Figure 6.6. It can be seen that although it is unfavourable for the water molecule to move across the ditrigonal cavity towards the interlayer, it is to a much lesser extent than that observed in the partial dehydroxylation of the *cis*-vacant isomer. This is because the residual oxygen atom and aluminium atoms are homogeneously charge compensated and it is therefore predominantly steric, as oppose to coulombic, interactions that hinder migration of the water molecule. In contrast to the *cis*-vacant case, the energy profile shows that the water molecule is always stable towards rehydroxylation during migration to the interlayer. The energy barrier to complete expulsion is approximately 50 kJ mol^{-1}, which is four times smaller than that calculated in the partial dehydroxylation of the *cis*-vacant isomer. The activation energy for dehydroxylation is simply equal to that for protonation, calculated to be approximately 230 kJ mol^{-1}.

The energy profile for the total dehydroxylation of *cis*-vacant pyrophyllite is shown in Figure 6.5. It can be seen that it is initially extremely unfavourable for the two water molecules to move across the ditrigonal cavity towards the interlayer. The energy barrier is similar to that observed in the partial dehydroxylation of the same isomer. Things change dramatically however, as the water molecules migrate further and are less able to compensate the asymmetric charge distribution around the aluminium atoms. Once the water molecules are a certain distance from the plane of the aluminium atoms the coulombic interactions between the residual oxygen atoms and aluminium atoms become so acutely unfavourable that cation migration occurs. This results in a *trans*-vacant structure, where the residual oxygen atoms and aluminium atoms are uniformly charge compensated and incurs a gain in energy of about 150 kJ mol^{-1}. Thereafter the water molecules experience an energy barrier to migration similar to that observed in the total and partial dehydroxylation of the *trans*-vacant isomer, seen in Figure 6.9. The total activation energy for dehydroxylation is approximately 200 kJ mol^{-1}, which is that required to bring about protonation and induce cation migration.

The energy profile for the total dehydroxylation of *trans*-vacant pyrophyllite is shown in Figure 6.8. It can be seen that again it is unfavourable for the water molecules to move across the ditrigonal cavity towards the interlayer. The energy barrier is similar to that observed in the partial dehydroxylation of the same isomer. The activation energy for dehydroxylation is likewise equal to that for protonation, calculated to be approximately 240 kJ mol^{-1}.

If we compare the activation energies for the dehydroxylation of *cis*-vacant pyrophyllite calculated from the partial and total dehydroxylation reactions we find that they are very different. The value calculated from partial dehydroxylation is approximately 350 kJ mol^{-1}, which is significantly larger than the 200 kJ mol^{-1} deduced from total dehydroxylation. This is because of the occurrence of cation migration in the total dehydroxylation case, which as discussed above, reduces the energy barrier towards the water molecules migrating to the interlayer.

It is postulated that for cation migration to occur in *cis*-vacant pyrophyllite a large number of neighbouring pairs of adjacent hydroxyl groups must react, to introduce sufficient flexibility into the layer structure. This is why it was not observed in the partial dehydroxylation case, but was seen for total dehydroxylation. Based on this assumption, dehydroxylation may proceed in two ways. In the first scenario, pairs of adjacent hydroxyl groups react in a sequential manner, with an associated activation energy similar to that calculated from the partial dehydroxylation case. But as this continues, more flexibility is introduced into the layer structure, cation migration becomes more prevalent and the activation energy for dehydroxylation of further pairs of adjacent hydroxyl groups decreases. In the second scenario, large numbers of neighbouring pairs of adjacent hydroxyl groups react together simultaneously, with an associated activation energy similar to that calculated for the total dehydroxylation case. In fact, a combination of both dehydroxylation mechanisms is thought most likely. This would lead to an activation energy for dehydroxylation between the two calculated values, much closer to the 250 kJ mol^{-1} calculated for montmorillonite from experimental data.[180]

Evidence for this kind of dehydroxylation behaviour in *cis*-vacant pyrophyllite has been observed in experimental studies. It has been reported that using a slower heating rate during thermal treatment reduces the dehydroxylation temperature of montmorillonite samples.[183] It could be conjectured that using a slower heating rate causes larger numbers of pairs of adjacent hydroxyl to simultaneously possess the energy to react together. Dehydroxylation would therefore proceed via the second mechanism, with the lower associated activation energy.

In contrast, the activation energies for dehydroxylation of *trans*-vacant pyrophyllite calculated from the partial and total dehydroxylation reactions are almost exactly the same at approximately 235 kJ mol^{-1}. This implies that in *trans*-vacant pyrophyllite the activation energy for dehydroxylation of each pair of adjacent hydroxyl groups is the same and independent of the dehydroxylation state of neighbouring pairs.

Though the calculations have only been concerned with pyrophyllite it is expected that the conclusions are applicable to all other aluminous, 2:1 layer type, *cis* and *trans*-vacant clay minerals.

6.3 Conclusions

The structure of montmorillonite is analogous to that of *cis*-vacant pyrophyllite. Density functional calculations have been performed to investigate the mechanism of dehydroxylation in both *cis* and *trans*-vacant pyrophyllite. In agreement with predictions from experiment, calculations show that both form a *trans*-vacant dehydroxylated structure, with aluminium in trigonal-bipyramidal coordination and a highly distorted tetrahedral layer. Differences in the dehydroxylation behaviour of *cis* and *trans*-vacant pyrophyllite are due to the fact that in the former adjacent hydroxyl groups bridge different pairs of aluminium atoms, while in the latter they bridge the same pair. These conclusions are thought to be valid for all aluminous, 2:1 layer type, dioctahedral clay minerals

Chapter 7

Conclusions

The reactivity of the clay mineral montmorillonite has been explored by density functional theory based calculations. Three particular aspects have been considered: catalytic properties, cation migration and dehydroxylation.

The catalytic properties of montmorillonite are quite complex. Several different Brønsted and Lewis acid sites exist. The Brønsted acidity of water in the hydration sphere of interlayer cations is very dependent on the type of cation, with small, highly charged cations being better able to polarise water molecules and bring about dissociation. Structural hydroxyl groups bonded to metal cation in the octahedral layer are inaccessible to even very small organics molecules because of the hexagonal silicate framework of the tetrahedral layer. Though much more accessible, hydroxyl groups bonded to basal oyxgen atoms in the tetrahedral layer are only weakly acidic. The acidity of such hydroxyl groups increases with distance from sites of isomorphic substitution in the octahedral layer, however, it is energetically most favourable for them to reside close to such sites. Those hydroxyl groups that terminate broken bonds at the clay mineral lattice-edge are also only weakly acidic. In constrast, exposed aluminium atoms at the clay mineral lattice-edge, in particular, those that are part of the tetrahedral layer, show strong Lewis acidity. These are able to activate methanal to induce nucleophilic attack from ethylenediamine. Protonation of methanal is not possible from any of the above Brønsted acid sources.

In montmorillonite, the migration of lithium cations into vacant octahedral sites causes structural hydroxyl groups to reorientate perpendicular to the *ab*-plane. This implies that the partial dichroic nature of hydroxyl stretching bands observed experimentally for heat treated lithium montmorillonite, is indicative of lithium cations being present in octahedral sites. In addition, it is energetically preferable for lithium cations to reside in octahedral sites, as oppose to the ditrigonal cavities. This is due to the closer proximity of the cations to negative charge sites in the octahedral layer, increasing favourable coulombic interactions. Dehydroxylation of the layers inhibits migration of lithium cations to octahedral sites, since it eliminates the negative hydroxyl oxygen atoms, which attracts them into ditrgonal cavities. Comparison of calculated power spectra with those from experiment indicates that lithium cations migrate to octahedral sites when no isomorphic substitution is present in the tetrahedral layer.

The structure of *cis*-vacant pyrophyllite is analogous to that of montmorillonite. Upon dehydroxylation, *cis* and *trans*-vacant pyrophyllite form a similar *trans*-vacant structure, with aluminium in trigonal bipyramidal coordination and a highly distorted tetrahedral layer. The energy required to enable a hydroxyl group to protonate an adjacent hydroxyl group is much less in *cis*-vacant pyrophyllite, as compared to *trans*-vacant, but a water molecule formed by such a reaction in the former is unstable towards rehydroxylation, while in the latter, once formed, a water molecule is relatively stable. In order for water molecules to be stable towards rehydroxylation in *cis*-vacant pyrophyllite cation migration must occur. The energy required for this is the reason for the higher dehydroxylation temperature of *cis*-vacant pyrophyllite, as compared to *trans*-vacant. The different dehydroxylation behaviour of the two isomers originates from the fact that in *cis*-vacant pyrophyllite adjacent hydroxyl groups bridge different pairs of aluminium atoms, while in *trans*-vacant pyrophyllite they bridge the same pair. These conclusions are thought to be valid for all aluminous, 2:1 layer type, dioctahedral clay minerals, independent of isomorphic substitution.

Overall it has been shown that density functional theory based calculations are an extremely powerful tool for the study of clay minerals, allowing one to correlate structural features with reactivity. The outlook appears good for its application to other clay mineral systems.

Bibliography

[1] N. N. Greenwood, A. Earnshaw, *Chemistry of the Elements*, Pergamon Press, Oxford, 1984, p 410.

[2] R. E. Grim, *Applied Clay Mineralogy*, McGraw-Hill Book Company, New York, 1953.

[3] R. E. Grim, *Clay Mineralogy*, McGraw-Hill Book Company, New York, 1962.

[4] G. W. Brindley, G. Brown (eds.), *Crystal Structures of Clay Minerals and their X-Ray Identification*, Mineralogical Society, London, 1980.

[5] D. W. Bruce, D. O'Hare (eds.), *Inorganic Materials*, Wiley, New York, 1992, pp 295-351.

[6] S. Cheng, *Catal. Today*, 1999, **49**, 303.

[7] A. Vaccari, *Appl. Clay Sci.*, 1999, **14**, 161.

[8] T.-Q. Li, M. Häggkvist, L. Ödberg, *Colloid. Surface. A*, 1999, **159**, 57.

[9] A. Allen, *Eng. Geol.*, 2001, **60**, 3.

[10] U. Kalbe, W. W. Müller, W. Berger, J. Eckardt, *Appl. Clay Sci.*, 2002. **21**, 67.

[11] H. Kugler, F. Ottner, H. Froeschl, R. Adamcova, B. Schwaighofer, *Appl. Clay Sci.*, 2002, **21**, 45.

[12] Almacenamiento Geológico Profundo de Residuos Radiactivos de alta Actividad (AGP): Conceptos Preliminares de Referencia., Technical Report 07/94, Empresa Nacional de Residuos Radiactivos, S.A., 1994.

[13] Environmental Impact Statement on the Concept for Disposal of Canada's Nuclear Fuel Waste., Technical Report AECL-10711,COG-93-1, Atomic Energy of Canda Limited, 1994.

[14] L. O. Ericsson, *Eng. Geol.*, 1999, **52**, 305.

[15] A. Meunier, B. Velde, L. Griffault, *Clay Miner.*, 1998, **33**, 187.

[16] T. Hueckel, R. Pellegrini, *Eng. Geol.*, 2002, **64**, 195.

[17] N. Sultan, P. Delage, Y. J. Cui, *Eng. Geol.*, 2002, **64**, 135.

[18] F. T. Madsen, *Clay Miner.*, 1998, **33**, 109.

[19] J. Choi, C.-H. Kang, J. Whang, *J. Environ. Sci. Heal. A*, 2001, **36**, 689.

[20] M. Martín, J. Cuevas, S. Leguey, *Appl. Clay Sci.*, 2000, **17**, 55.

[21] J. Bors, S. Dultz, B. Riebe, *Appl. Clay Sci.*, 2000, **16**, 1.

[22] S. Dultz, J. Bors, *Appl. Clay Sci.*, 2000, **16**, 15.

[23] Y. Kojima, A. Usuki, M. Kawasumi, A. Okada, T. Kurauchi, O. Kamigaito, *J. Polym. Sci. Pol. Chem.*, 1993, **31**, 983.

[24] L. Liu, Z. Qi, X. Zhu, *J. Appl. Polym. Sci.*, 1999, **71**, 1133.

[25] Flammability of Polymer Clay Nanocomposites Consortium: Year One Annual Report., Technical Report NISTIR 6531, National Institute of Standards and Technology, 2000.

[26] J. W. Gilman, *Appl. Clay Sci.*, 1999, **15**, 31.

[27] P. B. Messersmith, E. P. Giannelis, *J. Polym. Sci. Pol. Chem.*, 1995, **33**, 1047.

[28] M. Born, J. R. Openheimer, *Ann. Physik*, 1927, **84**, 457.

[29] D. Hartree, *Proc. Cambridge Phil. Soc.*, 1928, **24**, 426.

[30] W. Pauli, *Z. Physik*, 1925, **31**, 765.

[31] J. C. Slater, *Phys. Rev.*, 1930, **35**, 509.

[32] G. G. Hall, *Proc. Roy. Soc. Lond. A*, 1951, **205**, 541.

[33] C. C. J. Roothan, *Rev. Mod. Phys.*, 1951, **23**, 69.

[34] R. P. Feynman, *Phys. Rev.*, 1939, **56**, 340.

[35] P. Pulay, *Mol. Phys.*, 1969, **17**, 197.

[36] S. F. Boys, F. Bernardi, *Mol. Phys.*, 1970, **19**, 553.

[37] G. H. Grant, W. G. Richards, *Computational Chemistry.*, Oxford University Press, Oxford, 1985, pp 32-61.

[38] N. W. Ashcroft, N. D. Mermin, *Solid State Physics*, Harcourt College Publishers, Orlando, 1976, p 133.

[39] H. J. Monkhorst, J. D. Pack, *Phys. Rev. B*, 1976, **13**, 5188.

[40] A. H. MacDonald, *Phys. Rev. B*, 1978, **18**, 5897.

[41] J. C. Phillips, *Phys. Rev.*, 1958, **112**, 685.

[42] D. Vanderbilt, *Phys. Rev. B*, 1990, **41**, 7892.

[43] N. Troullier, J. L. Martins, *Phys. Rev. B*, 1991, **43**, 1993.

[44] L. Kleinman, D. M. Bylander, *Phys. Rev. Lett.*, 1982, **48**, 1425.

[45] A. Szabo, N. S. Ostlund, *Modern Quantum Chemistry*, Dover, Mineola, 1996, p 116.

[46] C. Møller, M. S. Plesset, *Phys. Rev.*, 1934, **46**, 618.

[47] R. Car, M. Parrinello, *Phys. Rev. Lett.*, 1985, **55**, 2471.

[48] P. Hohenberg, W. Kohn, *Phys. Rev. B*, 1964, **136**, 864.

[49] W. Kohn, L. J. Sham, *Phys. Rev. A*, 1965, **140**, 1133.

[50] E. J. Baerends, O. V. Gritsenko, *J. Phys. Chem. A*, 1997, **101**, 5383.

[51] K. Burke, J. P. Perdew, *Int. J. Quantum Chem.*, 1995, **56**, 199.

[52] N. Argaman, G. Makov, *Am. J. Phys.*, 2000, **68**, 69.

[53] J. Harris, *Phys. Rev. A*, 1984, **29**, 1648.

[54] J. C. Slater, *Phys. Rev.*, 1951, **81**, 385.

[55] S. H. Vosko, L. Wilk, M. Nusair, *Can. J. Phys.*, 1980, **58**, 1200.

[56] J. P. Perdew, Y. Wang, *Phys. Rev. B*, 1992, **45**, 13244.

[57] D. M. Ceperley, B. J. Alder, *Phys. Rev. Lett.*, 1980, **45**, 566.

[58] W. Koch, M. C. Holthausen, *A Chemist's Guide to Density Functional Theory*, Wiley VCH, Weinheim, 2002, p 74.

[59] F. Sim, A. St-Amant, I. Papai, D. R. Salahub, *J. Am .Chem. Soc.*, 1992, **114**, 4391.

[60] A. D. Becke, *Phys. Rev. A*, 1988, **38**, 3098.

[61] J. P. Perdew, J. A. Chevary, S. H. Vosko, K. A. Jackson, M. R. Perderson, D. J. Singh, C. Fiolhais, *Phys. Rev. B*, 1992, **46**, 6671.

[62] J. P. Perdew, J. A. Chevary, S. H. Vosko, K. A. Jackson, M. R. Perderson. D. J. Singh, C. Fiolhais, *Phys. Rev. B*, 1993, **48**, 4978.

[63] J. P. Perdew, K. Burke, M. Ernzerhof, *Phys. Rev. Lett.*, 1996, **77**. 3865.

[64] J. P. Perdew, K. Burke, M. Ernzerhof, *Phys. Rev. Lett.*, 1997, **78**, 1396.

[65] C. T. Lee, W. T. Yang, P. G. Parr, *Phys. Rev. B.*, 1988, **37**, 785.

[66] A. D. Becke, *J. Chem. Phys.*, 1993, **98**, 5648.

[67] J. A. Pople, D. P. Santry, G. A. Segal, *J. Chem. Phys.*, 1965, **43**, 129.

[68] J. A. Pople, G. A. Segal, *J. Chem. Phys.*, 1965, **43**, 136.

[69] R. C. Bingham, M. J. S. Dewar, D. Lo, *J. Am. Chem. Soc.*, 1975, **97**, 1285.

[70] M. J. S. Dewar, E. G. Zoebisch, E. F. Healy, J. J. P. Stewart, *J. Am. Chem. Soc.*, 1985, **107**, 3902.

[71] J. J. P. Stewart, *J. Comput. Chem.*, 1989, **10**, 209.

[72] J. J. P. Stewart, *J. Comput. Chem.*, 1989, **10**, 221.

[73] B. T. Luke, A. G. Gupta, G. H. Loew, J. G. Lawless, D. H. White, *Int. J. Quantum Chem.*, 1984, **11**, 117.

[74] J. D. Kubicki, G. A. Blake, S. E. Apitz, *Geochim. Cosmochim. Acta.*, 1997, **61**, 1031.

[75] H. Strandh, L. G. M. Pettersson, L. Sjöberg, U. Wahlgren, *Geochim. Cosmochim. Acta.*, 1997, **61**, 2577.

[76] B. J. Teppen, C.-H. Yu, S. Q. Newton, D. M. Miller, L. Schäfer, *J. Mol. Struct.*, 1998, **445**. 65.

[77] D. Bougeard, K. S. Smirnov, E. Geidel, *J. Phys. Chem. B*, 2000, **104**, 9210.

[78] C. I. Sainz-Diaz, V. Timon, V. Botella, A. Hernandez-Laguna, *Am. Mineral.*. 2000, **85**, 1038.

[79] A. Chatterjee, T. Iwasaki, H. Hayashi, T. Ebina, K. Torii, *J. Mol. Catal. A-Chem.*, 1998, **136**, 195.

[80] J. D. Kubicki, L. M. Schroeter, M. J. Itoh, B. N. Nguyen, S. E. Apitz, *Geochim. Cosmochim. Acta.*, 1999, **63**, 2709.

[81] J. D. Kubicki, M. J. Itoh, L. M. Schroeter, S. E. Apitz, *Environ. Sci. Technol.*, 1997, **31**, 1151.

[82] T. Ebina, T. Iwasaki, A. Chatterjee, M. Katagiri, G. D. Stucky, *J. Phys. Chem. B*, 1997, **101**, 1125.

[83] A. Chatterjee, T. Iwasaki, T. Ebina, H. Hayashi, *Appl. Surf. Sci.*, 1997, **121**, 167.

[84] L. G. Gorb, E. V. Aksenenko, J. W. Adams, S. L. Larson, C. A. Weiss, D. Leszczynska, J. Leszczynski, *J. Mol. Struc.-Theochem.*, 1998, **425**, 129.

[85] L. G. Gorb, J. D. Gu, D. Leszczynska, J. Leszczynski, *Phys. Chem. Chem. Phys.*, 2000, **2**, 5007.

[86] Y. I. Tarasevich, E. V. Aksenenko, *Colloid. Surface. A*, 2001, **180**, 33.

[87] A. Chatterjee, T. Iwasaki, T. Ebina, A. Miyamoto, *Comp. Mater. Sci.*, 1999, **14**, 119.

[88] T. Ebina, T. Iwasaki, A. Chatterjee, *Clay Sci.*, 1999, **10**, 569.

[89] A. Pelmenschikov, J. Leszczynski, *J. Phys. Chem.*, 1999, **103**, 6886.

[90] D. Tunega, G. Haberhauer, M. H. Gerzabek, H. Lischka, *Langmuir*, 2002, **18**, 139.

[91] A. Michalková, D. Tunega, L. T. Nagy, *J. Mol. Struc.-Theochem.*, 2002, **581**, 37.

[92] A. Chatterjee, T. Iwasaki, T. Ebina, H. Hayashi, *J. Mol. Graphic. Model.*, 1996, **14**, 302.

[93] B. J. Teppen, C.-H. Yu, S. Q. Newton, D. M. Miller, L. Schäfer, *J. Phys. Chem. A*, 2002, **106**, 5498.

[94] L. Benco, D. Tunega, J. Hafner, H. Lischka, *Am. Mineral.*, 2001, **86**, 1057.

[95] C. H. Bridgeman, A. D. Buckingham, N. T. Skipper, M. C. Payne, *Mol. Phys.*, 1996, **89**, 879.

[96] A. Chatterjee, T. Iwasaki, T. Ebina, *J. Phys. Chem. A*, 2000, **104**, 8216.

[97] A. C. Hess, V. R. Saunders, *J. Phys. Chem.*, 1992, **96**, 4367.

[98] C.-H. Yu, S. Q. Newton, D. M. Miller, B. J. Teppen, L. Schäfer, *Struct. Chem.*, 2001, **12**, 393.

[99] D. Tunega, L. Benco, G. Haberhauer, M. H. Gerzabek, H. Lischka, *J. Phys. Chem. B*, 2002, **106**, 11515.

[100] L. Benco, D. Tunega, J. Hafner, H. Lischka, *Chem. Phys. Lett.*, 2001, **333**, 479.

[101] L. Benco, D. Tunega, J. Hafner, H. Lischka, *J. Phys. Chem. B*. 2001, **105**, 10812.

[102] A. G. Cairns-Smith, *Genetic Takeover and the Mineral Origins of Life*, Cambridge University Press, London, 1982.

[103] D. Kleinhesselink, M. Wolfsberg, *Surf. Sci.*, 1992, **262**, 189.

[104] J.-R. Hill, J. Sauer, *J. Phys Chem.*. 1994. **98**, 1238.

[105] J.-R. Hill, J. Sauer, *J. Phys Chem.*, 1995, **99**, 9536.

[106] B. J. Teppen, K. Rasmussen, P. M. Bertsch, D. M. Miller, L. Schäfer, *J. Phys. Chem. B*, 1997, **101**, 1579.

[107] C.-H. Yu, M. A. Norman, S. Q. Newton, D. M. Miller, B. J. Teppen, L. Schäfer. *J. Mol. Struct.*, 2000, **556**, 95.

[108] V. A. Ermoshin, K. S. Smirnov, D. Bougeard, *Chem. Phys.*, 1996, **202**, 53.

[109] V. A. Ermoshin, K. S. Smirnov, D. Bougeard, *Chem. Phys.*, 1996, **209**, 41.

[110] J. P. Lemmon, J. Wu, C. Oriakhi, M. M. Lerner, *Electrochim. Acta.*, 1995, **40**, 2245.

[111] M. Wang, T. J. Pinnavaia, *Chem. Mater.*, 1994, **6**, 468.

[112] M. Okamoto, S. Morita, H. Taguchi, Y. H. Kim, T. Kotaka, H. Tateyama, *Polymer*, 2000, **10**, 3887.

[113] R. A. Vaia, H. Ishii, E. P. Giannelis, *Chem. Mater.*, 1993, **5**, 1694.

[114] R. A. Vaia, K. D. Jandt, E. J. Kramer, E. P. Giannelis, *Chem. Mater.*, 1996, **8**, 2628.

[115] M. Alexandre, P. Dubois, *Mat. Sci. Eng. R*, 2000, **28**, 1.

[116] P. V. Coveney, J. L. W. Griffin, M. Watkinson, A. Whiting, E. S. Boek, *Mol. Sim.*, 2002, **28**, 295.

[117] J. McMurry, *Organic Chemistry*, Brooks/Cole Publishing, Pacific Grove. CA. 1999, p 1271.

[118] H. van Olphen, J. J. Fripiat (eds.), *Data Handbook for Clay Materials and other Non-Metallic Minerals.*, Pergamon Press. New York. 1979. p 346.

[119] S. Moreno, R. S. Kou, G. Poncelet. *J. Catal.*, 1996. **162**, 198.

[120] J. Bujdák, B. M. Rode, *J. Mol. Catal. A-Chem.*, 1999, **144**, 129.

[121] D. H. White, R. M. Kennedy, J. Macklin, *Origins Life Evol. B.*, 1984, **14**, 273.

[122] R. Gregory, D. J. H. Smith, D. J. Westlake, *Clay Miner.*, 1983, **18**, 431.

[123] C. L. Marshall, J. B. Nicholas, H. Brand, K. A. Carrado, R. E. Winans, *J. Phys. Chem.*, 1996, **100**, 15748.

[124] S. Nishihama, H. Yamada, H. Nakazawa, *Clay Miner.*, 1997, **32**, 645.

[125] D. T. B. Tennakoon, R. Schlögl, T. Rayment, J. Klinowski, W. Jones, J. M. Thomas, *Clay Miner.*, 1983, **18**, 357.

[126] M. Trombetta, G. Busca, M. Lenarda, L. Storaro, R. Ganzerla, L. Piovesan, A. J. Lopez, M. Alcantara-Rodrìguez, E. Rodríguez-Castellón, *Appl. Catal. A-Gen.*, 2000, **193**, 55.

[127] J. M. Adams, T. V. Clapp, D. E. Clement, *Clay Miner.*, 1983, **18**, 411.

[128] P. V. Brady, R. T. Cygan, K. L. Nagy, *J. Colloid Interf. Sci.*, 1996, **183**, 356.

[129] A. Negrón-Mendoza, S. Ramos-Bernal, G. Albarrán, J. Reyes-Gasga, *Nanostruct. Mater.*, 1997, **9**, 209.

[130] R. W. G. Wyckoff, *Crystal Structure Volume 4*, John Wiley and Sons, Chichester, 1968, p 372.

[131] V. A. Drits, G. Besson, F. Muller, *Clays Clay Miner.*, 1995, **43**, 718.

[132] F. Muller, V. Drits, A. Plançon, J.-L. Robert, *Clays Clay Miner.*, 2000, **48**, 572.

[133] C. I. Sainz-Diaz, A. Hernández-Laguna, M. T. Dove, *Phys. Chem. Miner.*, 2001, **28**, 322.

[134] Accelrys, 9685 Scranton Road, San Diego, CA 92121-3752, U.S.A.

[135] A. S. Bains, E. S. Boek, P. V. Coveney, S. J. Williams. M. V. Akbar. *Mol. Sim.*, 2001, **26**, 101.

[136] K. B. Lipkowitz, D. B. Boyd (eds.), *Reviews in Computational Chemistry*, VCH Publishers, New York, 1990, ch 2.

[137] M. C. Payne, M. P. Teter, D. C. Allan, T. A. Arias, J. D. Joannopoulos, *Rev. Mod. Phys.*, 1992, **64**, 1045.

[138] G. P. Francis, M. C. Payne, *J. Phys.-Condens. Matter*, 1990, **2**, 4395.

[139] E. S. Boek, M. Sprik, *J. Phys. Chem. B*, 2003, **107**, 3251.

[140] R. Calvet, *Ann. Agron.*, 1973, **24**, 77.

[141] M. H. Fu, Z. Z. Zhang, P. F. Low, *Clays Clay Miner.*, 1990, **38**, 485.

[142] A. Delville, P. Laszlo, *Langmuir*, 1990, **6**, 1289.

[143] A. Delville, *Langmuir*, 1991, **7**, 547.

[144] E. S. Boek, P. V. Coveney, N. T. Skipper, *J. Am. Chem. Soc.*, 1995, **117**, 12608.

[145] F.-R. C. Chang, N. T. Skipper, G. Sposito, *Langmuir*, 1997, **13**, 2074.

[146] F.-R. C. Chang, N. T. Skipper, G. Sposito, *Langmuir*, 1998, **14**, 1201.

[147] J. Greathouse, G. Sposito, *J. Phys. Chem. B*, 1998, **102**, 2406.

[148] D. E. Smith, *Langmuir*, 1998, **14**, 5959.

[149] S.-H. Park, G. Sposito, *J. Phys. Chem. B*, 2000, **104**, 4642.

[150] U. Hofmann, R. Klemen, *Z. Anorg. Allg. Chem.*, 1950, **262**, 95.

[151] R. Tettenhorst, *Am. Mineral.*, 1962, **47**, 769.

[152] R. Alvero, M. D. Alba, M. A. Castro, J. M. Trillo, *J. Phys. Chem.*, 1994, **98**. 7848.

[153] B. K. G. Theng, S. Hayashi, M. Soma, H. Seyama, *Clays Clay Miner.*, 1997, **45**, 718.

[154] E. Srasra, F. Bergaya, J. J. Fripiat, *Clays Clay Miner.*, 1994, **42**, 237.

[155] M. A. Karakassides, D. Gournis, D. Petridis, *Clay Miner.*, 1999, **34**, 429.

[156] J. Hrobáriková, J. Madejová, P. Komadel, *J. Mater. Chem.*, 2001, **11**, 1452.

[157] R. Calvet, R. Prost, *Clays Clay Miner.*, 1971, **19**, 175.

[158] G. Sposito, R. Prost, J.-P. Gaultier, *Clays Clay Miner.*, 1983, **31**, 9.

[159] J. Madejová, B. Arvaiová, P. Komadel, *Spectrochim. Acta A*, 1999, **55**, 2467.

[160] M. A. Karakassides, J. Madejová, B. Arvaiová, A. Bourlinos, D. Petridis, P. Komadel, *J. Mater. Chem.*, 1999, **9**, 1553.

[161] J. Madejová, J. Bujdák, S. Petit, P. Komadel, *Clay Miner.*, 2000, **35**, 739.

[162] L. Heller-Kallai, *Appl. Clay Sci.*, 2001, **20**, 27.

[163] J. Bujdák, H. Slosiariková, *J. Therm. Anal.*, 1994, **41**, 825.

[164] H. P. He, J. G. Guo, X. D. Xie, J. L. Peng, *Environ. Int.*, 2001, **26**, 347.

[165] P. Bala, K. Samantaray, S. K. Srivastava, *Bull. Mater. Sci.*, 2000, **23**, 61.

[166] K. Yamaji, Y. Makita, H. Watanabe, A. Sonoda, H. Kanoh, T. Hirotsu, K. Ooi, *J. Phys. Chem. A*, 2001, **105**, 602.

[167] G. Rauhut, P. Pulay, *J. Phys. Chem.*, 1995, **99**, 3093.

[168] A. A. El-Azhary, H. U. Suter, *J. Phys. Chem.*, 1996, **100**, 15056.

[169] A. P. Scott, L. Radom, *J. Phys. Chem.*, 1996, **100**, 16502.

[170] M. D. Halls, J. Velkovski, H. B. Schlegel, *Theor. Chem. Acc.*, 2001, **105**. 413.

[171] V. Š. Fajnor, L. Kuchta, *J. Therm. Anal.*, 1995, **45**, 481.

[172] V. Š. Fajnor, K. Jesenák, *J. Therm. Anal.*, 1996, **46**, 489.

[173] L. Wang, M. Zhang, S. A. T. Redfern, Z. Zhang, *Clays Clay Miner.*. 2002, **50**, 272.

[174] R. L. Frost, P. F. Barron, *J. Phys. Chem.*, 1984, **88**, 6206.

[175] J. J. Fitzgerald, S. F. Dec, A. I. Hamza, *Am. Mineral.*, 1989, **74**, 1405.

[176] J. J. Fitzgerald, A. I. Hamza, S. F. Dec, C. E. Bronnimann, *J. Phys. Chem.*, 1996, **100**, 17351.

[177] D. T. B. Tennakoon, J. M. Thomas, W. Jones, T. A. Carpenter, S. Ramdas, *J. Chem. Soc., Farad. T. 1*, 1986, **82**, 545.

[178] S. Guggenheim, A. F. K. van Groos, *J. Therm. Anal.*, 1992, **38**, 2529.

[179] H. J. Bray, S. A. T. Redfern, *Mineral. Mag.*, 1998, **62**, 647.

[180] H. J. Bray, S. A. T. Redfern, *Mineral. Mag.*, 2000, **64**, 337.

[181] Y. Sarikaya, M. Önal, B. Baran, T. Alemdaroğlu, *Clays Clay Miner.*, 2000. **48**, 557.

[182] K. Emmerich, F. T. Madsen, G. Kahr, *Clays Clay Miner.*, 1999. **47**. 591.

[183] K. Emmerich, *Clays Clay Miner.*, 2000, **48**, 405.

[184] K. Emmerich, G. Kahr, *Appl. Clay Sci.*. 2001. **20**, 119.

[185] K. Emmerich, M. Plötze, G. Kahr. *Appl. Clay Sci.*. 2001. **19**, 143.

[186] CPMD, Copyright IBM Corp. 1990-2001. Copyright MPI für Festkörperforschung, Stuttgart, 1997-2001.

[187] M. E. Tuckerman, G. J. Martyna, *J. Phys. Chem. B*, 2000, **104**. 159.

[188] J. Hutter, H. P. Lüthi, M. Parrinello, *Comp. Mater. Sci.*, 1994, **2**, 244.

[189] R. Fletcher, *Practical Methods of Optimization.*, Wiley, New York, 1980.

[190] P. L. Silvestrelli, M. Parrinello, *J. Chem. Phys.*, 1999, **111**, 3572.

[191] R. Wardle, G. W. Brindley, *Am. Mineral.*, 1972, **57**, 732.